

Developing Efficient Cu₂ZnSnS₄ (CZTS) Thin Film Solar Cells by Heterojunction Engineering

Author:

Sun, Heng

Publication Date:

2021

DOI:

<https://doi.org/10.26190/unsworks/2015>

License:

<https://creativecommons.org/licenses/by/4.0/>

Link to license to see what you are allowed to do with this resource.

Downloaded from <http://hdl.handle.net/1959.4/100105> in <https://unsworks.unsw.edu.au> on 2024-04-27

Developing Efficient $\text{Cu}_2\text{ZnSnS}_4$ (CZTS) Thin Film Solar Cells by Heterojunction Engineering

Heng Sun

A THESIS IN FULFILMENT OF THE REQUIREMENTS FOR THE
DEGREE OF DOCTOR OF PHILOSOPHY



UNSW
SYDNEY

School of Photovoltaic and Renewable Energy Engineering

Faculty of Engineering

September 2021

THESIS/DISSERTATION SHEET

Surname/Family Name	:	Sun
Given Name/s	:	Heng
Abbreviation for degree as give in the University calendar	:	PhD
Faculty	:	Faculty of Engineering
School	:	School of Photovoltaic and Renewable Energy Engineering
Thesis Title	:	Developing Efficient Cu₂ZnSnS₄ (CZTS) Thin Film Solar Cells by Heterojunction Engineering

Abstract

Kesterite Cu₂ZnSnS₄ (CZTS), having the Earth-abundant and environment-benign constituents, and stable structure, is regarded as a promising thin-film photovoltaic material. However, the current power conversion efficiency (PCE) of CZTS solar cells is far below the commercialization-viable level. One of the main issues restricting the efficiency is the severe Shockley-Read-Hall (SRH) recombination at the highly defective CdS-buffer/CZTS-absorber heterointerface and within the CZTS absorber layer, giving rise to a large open circuit voltage (V_{OC}) deficit. This thesis aims to mitigate the SRH recombination within the CdS/CZTS heterojunction by novel post-deposition treatment technologies to facilitate the passivation of the local defects.

Firstly, the ultrathin intermediate stannic oxide (SnO₂) layer was introduced at the CZTS/CdS heterointerface via a solution method. The employment of this layer enabled the effective passivation of the heterointerface, resulting in higher V_{OC}, fill factor (FF) and thus PCE. Secondly, we applied our in-house developed moisture-assisted post-deposition annealing (MAPDA) treatment to modify the heterojunction by manipulating the trace element distributions. This technology enabled Na and K depletion in the CZTS film, which, in turn, facilitated the spontaneous Cd diffusion during the chemical bath deposition process for CdS buffer layer, driving a significant improvement in device performance. The heterojunction modification is attributed to the remarkable mitigation of local deep-level defect and the creation of the preferable shallow acceptor copper vacancies. Peak efficiency at 9.40 % was obtained using the combined MAPDA and heterojunction air annealing (HJA) treatments, which further optimized the elemental distributions within the heterojunction region. Finally, the nanoscale optoelectronic characterization techniques, including Kelvin probe force microscopy (KPFM) and conductive-atomic force microscopy (C-AFM) were applied to investigate the impact of excess Na and K at the CZTS surface. The significant enhancement of quasi-Fermi level splitting and effective alleviation of SRH recombination through the combined MAPDA and HJA treatments were also revealed by surface photovoltage (SPV) analysis through KPFM.

These technologies with first-hand novelty explore new defect passivation routes in kesterite solar cells, which can also be widely applied to other thin-film solar cells.

Declaration relating to disposition of project thesis/dissertation

I hereby grant to the University of New South Wales or its agents a non-exclusive licence to archive and to make available (including to members of the public) my thesis or dissertation in whole or in part in the University libraries in all forms of media, now or here after known. I acknowledge that I retain all intellectual property rights which subsist in my thesis or dissertation, such as copyright and patent rights, subject to applicable law. I also retain the right to use all or part of my thesis or dissertation in future works (such as articles or books).

.....
Signature

.....
Date

The University recognises that there may be exceptional circumstances requiring restrictions on copying or conditions on use. Requests for restriction for a period of up to 2 years can be made when submitting the final copies of your thesis to the UNSW Library. Requests for a longer period of restriction may be considered in exceptional circumstances and require the approval of the Dean of Graduate Research.

INCLUSION OF PUBLICATIONS STATEMENT

UNSW is supportive of candidates publishing their research results during their candidature as detailed in the UNSW Thesis Examination Procedure.

Publications can be used in their thesis in lieu of a Chapter if:

- The candidate contributed greater than 50% of the content in the publication and is the “primary author”, ie. the candidate was responsible primarily for the planning, execution and preparation of the work for publication
- The candidate has approval to include the publication in their thesis in lieu of a Chapter from their supervisor and Postgraduate Coordinator.
- The publication is not subject to any obligations or contractual agreements with a third party that would constrain its inclusion in the thesis

Please indicate whether this thesis contains published material or not:

☐

This thesis contains no publications, either published or submitted for publication

☒

Some of the work described in this thesis has been published and it has been documented in the relevant Chapters with acknowledgement

☐

This thesis has publications (either published or submitted for publication) incorporated into it in lieu of a chapter and the details are presented below

CANDIDATE'S DECLARATION

I declare that:

- I have complied with the UNSW Thesis Examination Procedure
- where I have used a publication in lieu of a Chapter, the listed publication(s) below meet(s) the requirements to be included in the thesis.

Candidate's Name

Signature

Date (dd/mm/yy)

ORIGINALITY STATEMENT

I hereby declare that this submission is my own work and to the best of my knowledge it contains no materials previously published or written by another person, or substantial proportions of material which have been accepted for the award of any other degree or diploma at UNSW or any other educational institution, except where due acknowledgement is made in the thesis. Any contribution made to the research by others, with whom I have worked at UNSW or elsewhere, is explicitly acknowledged in the thesis. I also declare that the intellectual content of this thesis is the product of my own work, except to the extent that assistance from others in the project's design and conception or in style, presentation and linguistic expression is acknowledged.

Signed:

Date:

COPYRIGHT STATEMENT

I hereby grant the University of New South Wales or its agents a non-exclusive licence to archive and to make available (including to members of the public) my thesis or dissertation in whole or part in the University libraries in all forms of media, now or here after known. I acknowledge that I retain all intellectual property rights which subsist in my thesis or dissertation, such as copyright and patent rights, subject to applicable law. I also retain the right to use all or part of my thesis or dissertation in future works (such as articles or books).

For any substantial portions of copyright material used in this thesis, written permission for use has been obtained, or the copyright material is removed from the final public version of the thesis.

Signed:

Date:

AUTHENTICITY STATEMENT

I certify that the Library deposit digital copy is a direct equivalent of the final officially approved version of my thesis.

Signed:

Date:

Abstract

Kesterite $\text{Cu}_2\text{ZnSnS}_4$ (CZTS), having the Earth-abundant and environment-benign constituents, and stable structure, is regarded as a promising thin-film photovoltaic material. However, the current power conversion efficiency (PCE) of CZTS solar cells is far below the commercialization-viable level. One of the main issues restricting the efficiency is the severe Shockley-Read-Hall (SRH) recombination at the highly defective CdS-buffer/CZTS-absorber heterointerface and within the CZTS absorber layer, giving rise to a large open circuit voltage (V_{OC}) deficit. This thesis aims to mitigate the SRH recombination within the CdS/CZTS heterojunction by novel post-deposition treatment technologies to facilitate the passivation of the local defects.

Firstly, the ultrathin intermediate stannic oxide (SnO_2) layer was introduced at the CZTS/CdS heterointerface via a solution method. The employment of this layer enabled the effective passivation of the heterointerface, resulting in higher V_{OC} , fill factor (FF) and thus PCE. Secondly, we applied our in-house developed moisture-assisted post-deposition annealing (MAPDA) treatment to modify the heterojunction by manipulating the trace element distributions. This technology enabled Na and K depletion in the CZTS film, which, in turn, facilitated the spontaneous Cd diffusion during the chemical bath deposition process for CdS buffer layer, driving a significant improvement in device performance. The heterojunction modification is attributed to the remarkable mitigation of local deep-level defect and the creation of the preferable shallow acceptor copper vacancies. Peak efficiency at 9.40 % was obtained using the combined MAPDA and heterojunction air annealing (HJA) treatments, which further optimized the elemental distributions within the heterojunction region. Finally, the nanoscale optoelectronic characterization techniques, including Kelvin probe force

microscopy (KPFM) and conductive-atomic force microscopy (C-AFM) were applied to investigate the impact of excess Na and K at the CZTS surface. The significant enhancement of quasi-Fermi level splitting and effective alleviation of SRH recombination through the combined MAPDA and HJA treatments were also revealed by surface photovoltage (SPV) analysis through KPFM.

These technologies with first-hand novelty explore new defect passivation routes in kesterite solar cells, which can also be widely applied to other thin-film solar cells.

Acknowledgement

The research work presented in this thesis was carried out in Australian Centre for Advanced Photovoltaics, School of Photovoltaic and Renewable Energy Engineering, University of New South Wales. In this 4-year PhD pursuit period, it has undergone over 1-year lab closure for maintenance, 0.5-year out of control of experimental baseline recipes due to equipment resettlements and 1.5-year pandemic outbreak. In these depression downturns, this thesis would never be accomplished without the guidance, assistance, and support of many people.

First, I would like to thank my parents – mom Hongwei Huo and dad Fuyan Sun, who gave me great support and encouragement for my overseas study over nine years in Australia. In the second year of my bachelor's degree, my family encountered financial hardship, but hid it from me and continued paying expensive tuition fees year by year. The truth was finally unveiled until I was able to maintain the basic daily lives by myself after finished my bachelor's degree. There was a fork in the road after completion of my bachelor's degree: either worked in a company or accomplished a doctorate degree. At that time, I received both an offer from a consultant company providing renewable energy advice and an opportunity to pursue a PhD degree at university labs. My parents encouraged me to choose the latter without any hesitations under severe financial difficulties. I would also thank my wife Jiayi Zhang, who continuously understands and supports my research life. Without their support, I would never commence and finish my degree.

I would like to express my sincere gratitude to my supervisor, Associate Professor Xiaojing Hao, for her kind and patient guidance and support. It was rather difficult for me to commence my research career without fulfilling a master's degree. It was her who gave me

the valuable opportunity to practice the research skill as a research assistant. After acquiring the relevant experience over one year, I started the pursuit of my PhD degree with the support from her. I am deeply inspired and motivated by her academic zeal and enthusiasm, diligence, and uncompromising attitudes towards tough issues. Without her solid support, helpful academic guidance, and far-seeing advice, I would never commence and finish my thesis here. My great thank would also go to my joint supervisor Scientia Professor Marin Green. I appreciate his encouragement, warm discussions, constructive suggestions and particularly, the inspiration from the power of a role model.

I would like to appreciate my co-supervisor Professor Fangyang Liu and Dr Jialiang Huang. Professor Liu brought me from a green hand to a sophisticated processor at grips of CZTS fabrication skills and of fundamental knowledge of CZTS solar cells during my research assistant stage and the beginning of my PhD study. I was instructed and trained by him on CZTS device fabrication, characterization techniques, digestion of the literature, manuscript drafting, etc. The work in Chapter 3 was proposed and supervised by him. After Professor Liu commenced his new career in China at the beginning of 2018, Dr Huang became my co-supervisor, who brought me from a sophisticated processor to a researcher. He not only imparted profound characterization techniques, but more importantly the ways to be a good researcher. He instructed me on the strategies of initiation of a research project, design and proceeding of the project, data analysis, presentation of the research outcomes, paper drafting and so on. The work in Chapter 4, 5 and 6 was supervised by him. I would also thank Dr Jianjun Li for his guidance based on his proficient academic writing skills and experiment experience, which greatly support the work from Chapter 4 to 6. I would also acknowledge Dr Jae Sung Yun for his expertise in Kelvin probe force microscopy measurements, which greatly contribute to the work in Chapter 6. Keeping in mind these suggestions, I obtained the

research outcomes efficiently without many detours. Without their supports, I would not finish this thesis.

Besides, I would like to appreciate the researchers who have great contributions to my thesis work. Thanks Dr Jialiang Huang, Dr Jianjun Li, Dr Kaiwen Sun, Associate Professor Xiaojing Hao and Dr Matthew Wright for insightful discussions and manuscript review. Acknowledges Dr Jialiang Huang for complicated characterizations, including TEM, *C-V*, AS. Thanks Dr Kaiwen Sun for PL measurement and fabrication assistance, Dr Chang Yan for CZTS composition control and other fabrication assistance, Professor Fangyang Liu for the supervision in Chapter 3, Dr Trevor Young for the equipment design contributing to the work in Chapter 4, 5 and 6, Dr Jae Sung Yun and Mr Adam O'Neill for KPFM measurements in Chapter 6, Mr Jialin Cong for AS measurement, Dr Michael Nielsen and Ms Xueyun Zhang for photoreflectance measurement in Chapter 4 and 5, Dr Bin Gong for his ToF-SIMS and XPS expertise, Dr Yin Yao for training C-AFM used in Chapter 6, Dr Anne Rich for Raman training, Dr David Mitchell and Dr Gilberto Casillas Garcia at the University of Wollongong Electron Microscopy Centre for the use of facilities and assistance, Mr Patrick Campbell, Mr Tom Puzzer and Mr Mark Griffin for maintaining the good condition of the sputtering machine, Mr Bernhard Vogl for maintaining the sulfurization furnace, and Mr Alan Yee for maintaining all machines for the basic device characterizations.

I would like to thank my other colleagues and friends who worked together: Dr Jongsung Park, Dr Xin Cui, Professor Hongtao Cui, Dr Aobo Pu, Dr Yuanfang Zhang, Ms Caixia Li, Mr Mingrui He, Dr Yajie Jiang, Dr Lei Shi, Dr Xu Liu, Dr Ziheng Liu, Dr Robert Lee, Dr Yiyu Zeng, Dr Chaowei Xue, Mr Xiaojie Yuan, Mr Ao Wang, Mr Guojun He, Dr Fajun Ma,

Dr Mahesh Suryawanshi, Ms Yasaman Tabari-Saadi, Dr Pengfei Zhang, Mr Yihao Wang, Dr Daniel Chen, Dr Ning Song, Dr Yicong Hu, Dr Yan Zhu, Dr Li Wang, Mr Zhen Yang, Mr Wei Zhang, Dr Moonyong Kim, Mr Bruno Vicari Stefani, Dr Arman Mahboubi Soufiani, Dr Chuqi Yi, Ms Rong Deng and Dr Jingnan Tong for their encouragement and kindly assistance in research and daily lives.

“我成功的秘诀：知识、汗水、灵感、机遇。

科学研究要勇于探索，勇于创新，这个是关键。搞科研，应该尊重权威但不能迷信权威，应该多读书但不能迷信书本。科研的本质是创新，如果不尊重权威、不读书，创新就失去了基础；如果迷信权威、迷信书本，创新就没有了空间。”

————— 袁隆平

Table of Content

Abstract	iv
Acknowledgement	vi
List of Abbreviations	xvi
List of Symbols	xix
List of Chemical Nomenclature	xxi
Chapter 1 Introduction	1
1.1 Global Warming – the Common Enemy of Human Being	1
1.2 The Energy from the Sun	3
1.3 The Opportunities of Thin Film Solar Cells	7
1.4 Kesterite $\text{Cu}_2\text{ZnSnS}_4$ (CZTS) Photovoltaics – a Promising Thin Film Technology ..	9
1.5 Thesis Objectives – Healing the Heterojunction	10
1.6 Thesis Outline	12
1.7 Reference.....	15
Chapter 2 Backgrounds	19
2.1 Properties of Kesterite Compounds.....	19
2.1.1 Structure of Kesterite Compounds.....	19
2.1.2 Band Structure and Properties from the First-Principles Modeling.....	20
2.1.3 Optical Properties from the First-Principles Modeling.....	23
2.2 Kesterite Reaction Equilibrium.....	25
2.3 Loss Mechanisms and the Relevant Approaches	26

2.3.1	Voc Deficit – the Major Bottleneck of Kesterite Solar Cell Development.....	26
2.3.2	Zero-Dimensional Defects	27
2.3.3	Two-Dimensional Defects	33
2.3.4	Three-Dimensional Defects	36
2.4	Fabrication of CZTS Solar Cells	39
2.5	Reference.....	43
 Chapter 3 Buffer/Absorber Heterointerface Passivation of High-Efficiency CZTS Solar Cells Using an Ultrathin Intermediate Stannic Oxide Layer via a Solution Method		
3.1	Introduction	56
3.2	Experimental	58
3.3	Results and Discussion.....	60
3.3.1	Method Verification and Validation	60
3.3.2	Effectiveness of CdS/CZTS Heterointerface Passivation.....	62
3.3.3	Improvement in Device Performance	63
3.3.4	Impacts of Device Performance from Different SnO ₂ Thickness.....	65
3.3.5	Limitations	69
3.3.6	Change in CdS	70
3.3.7	Thinner CdS for Parasitic Absorption Mitigation.....	71
3.3.8	Mechanisms of the CdS/CZTS Heterointerface Passivation	73
3.4	Summary	75
3.5	Reference.....	77

Chapter 4 Elemental Redistribution Induced Heterojunction Modification by

Moisture-assisted Post-deposition Annealing.....	80
4.1 Introduction	80
4.2 Experimental	81
4.3 Results and Discussion.....	85
4.3.1 Manipulation of Critical Trace Elements.....	85
4.3.2 The Increased Disorder	94
4.3.3 Diffusion and Activation of Cd at Low Temperature	96
4.3.4 Defect Investigations	99
4.3.5 Modification in the CZTS/CdS Heterointerface	102
4.3.6 Improvement in Device Performance	104
4.4 Summary	107
4.5 Reference.....	108

Chapter 5 Efficient CZTS Solar Cells with Significant Optimization of Heterojunction by Combined Post Annealing: Moisture-Assisted Post-Deposition Annealing and

Heterojunction Annealing	115
5.1 Introduction	115
5.2 Experiment	116
5.3 Results and Discussion.....	118
5.3.1 Further Modification of Elemental Distributions	118
5.3.2 Further Improvement in Device Performance	120
5.3.3 Variations of the CdS Layer due to the Post-Annealing Treatments.....	126

5.4	Summary	130
5.5	Reference.....	131
Chapter 6 In-depth Study of Moisture-assisted Post-deposition Annealing & Heterojunction Air Annealing by Nanoscale Optoelectronic Characterization Techniques		
		135
6.1	Introduction	135
6.2	KPFM Operation Principle, Applications of Chalcopyrite/Kesterite Semiconductors & Methods.....	136
6.3	The Effect of Excessive Na and K at the CZTS Surface	141
6.4	Direct Observations of the V_{OC} Improvement in a Nanoscale View.....	144
6.5	Investigation of the CdS Variations due to MAPDA and HJA.....	152
6.6	Summary	158
6.7	Reference.....	158
Chapter 7 Summary and Future Work		163
7.1	Overall Conclusions	163
7.2	Future Work	165
7.2.1	Investigation of the Correlation among CdS Compositional, Structural and Optoelectrical Properties due to MAPDA and HJA	166
7.2.2	Upgrading of the MAPDA Technology by Adding a Cd Ion Soaking Process Before the CdS Deposition	166
7.2.3	An Efficient Li Doping Strategy by MAPDA and LiCl Post-deposition Treatment.....	166

7.2.4	Promoting V_{oc} by Passivating Acceptor-like Interface Defects via MAPDA plus $ZnCl_2$ or $Zn(CH_3COO)_2$ Post-treatment	167
7.3	Reference.....	168
Appendix A – List of Publications.....		169

List of Abbreviations

Abbreviation	Description
AFM	Atomic force microscopy
ALD	Atomic layer deposition
AM	Air mass
APT	Atomic probe tomography
ARC	Anti-reflection coating
AS	Admittance spectroscopy
BIPV	Building-integrated photovoltaics
BZ	Brillouin zone
C-AFM	Conductive-atomic force microscopy
CB	conduction band
CBD	Chemical bath deposition
CBM	Conduction band maximum
CBO	Conduction band offset
CPD	Contact potential difference
DC	Direct current
DI	Deionized
DLCP	Drive-level capacitance profiling
DOS	Density of States
EDX	Energy dispersive x-ray
EQE	External quantum efficiency
FEG	Field emission gun

Abbreviation	Description
FIB	Focused ion beam
FP-LAPW	Full-potential linearized augmented plane wave
FWHM	Full width at half maximum
GB	Grain boundary
GGA	Generalized gradient approximation
GI	Grain interior
GS	Grain surface
GW	gigawatt
HADDF	High-angle annular dark field
HJA	Heterojunction air annealing
IoT	Internet of things
IPCC	Intergovernmental Panel on Climate Change
ITO	Indium tin oxide
ITRPV	International Technology Roadmap for Photovoltaic
KPFM	Kelvin probe force microscopy
kWh	Kilowatt hours
MAPDA	Moisture-assisted Post-deposition Annealing
PCE	Power conversion efficiency
PDA	Post-deposition annealing
PDT	Post-deposition treatment
PIPV	Product-integrated photovoltaics
PV	Photovoltaic
PVD	Physical vapour deposition
QFLS	Quasi-Fermi level splitting

Abbreviation	Description
RF	Radio frequency
RH	Relative humidity
RTP	Rapid thermal processing
SCR	Space charge region
SILAR	Successive ionic layer adsorption and reaction
SLG	Soda lime glass
SPV	Surface photovoltage
SQ	Shockley-Queisser
SRH	Shockley-Read-Hall
STEM	Scanning transmission electron microscopy
TMA	Trimethylaluminum
ToF-SIMS	Time-of-flight secondary ion mass spectrometry
TRPL	Time-resolved photoluminescence
TW	terawatt
UAV	Unmanned aerial vehicle
UNSW	University of New South Wales
VB	Valence band
VBM	Valence band maximum
VBO	Valence band offset
VIPV	Vehicle-integrated photovoltaics
WBG	Wide band gap
XPS	X-ray photoelectron spectroscopy
XRD	X-ray diffraction

List of Symbols

Symbol	Description
A	Ideality factor
C	Capacitance
c	Light speed
$C-V$	Capacitance-voltage
E_a	Activation energy
E_g	Band gap
E_{ph}	Photon energy
F_{ES}	Electrostatic force
FF	Fill factor
J_0	Reverse saturation current density
J_{SC}	Short circuit current density
$J-V$	Current density - voltage
k	Boltzmann constant
N_a	Acceptor concentration
N_{CV}	Carrier concentration by CV
N_d	Donor concentration
N_{DL}	Carrier concentration by DLCP
N_T	Defect concentration
p.FF	Pseudo fill factor
q	Unit charge
R_S	Series resistance

Symbol	Description
R_{SH}	Shunt resistance
T	Temperature
V	Voltage
V_a	Applied bias potential
V_{bi}	Built-in potential
V_{CPD}	Contact potential difference
V_{OC}	Open circuit voltage
V_{sample}	Potential of sample surface
V_{tip}	Potential of tip
W_d	Depletion width
α	Absorption coefficient
$\Delta\mu$	Quasi-Fermi level splitting
ε	Permittivity
η	Power conversion efficiency
ν_0	Attempt-to-escape frequency of defect
σ	Charge density per unit area
ω	Angular frequency
ω_0	Inflection angular frequency
Φ_{sample}	Work function of sample surface
Φ_{tip}	Work function of tip

List of Chemical Nomenclature

Abbreviation	Description
Ag	Silver
Al	Aluminium
Al(CH ₃) ₃	Trimethylaluminum
Al ₂ O ₃	Aluminium oxide
Ba	Barium
Cd	Cadmium
CdS	Cadmium sulfide
CdSO ₄	Cadmium sulfate
CdTe	Cadmium telluride
CH ₄	Methane
CIGSe	Cu(In,Ga)Se ₂
Co	Cobalt
CO ₂	Carbon dioxide
c-Si	Crystalline Si
Cu	Copper
Cu ₂ S	Copper (I) sulfide
CuS	Copper (II) sulfide
CZTS	Cu ₂ ZnSnS ₄
CZTSe	Cu ₂ ZnSnSe ₄
CZTSSe	Cu ₂ ZnSn(S,Se) ₄
Fe	Iron
GaAs	Gallium arsenide

Symbol	Description
Ge	Germanium
H	Hydrogen
H ₂ O	Water
H ₂ S	Hydrogen sulfide
In	Indium
i-ZnO	Intrinsic zinc oxide
K	Potassium
MgF ₂	Magnesium fluoride
Mn	Manganese
Mo	Molybdenum
MoS ₂	Molybdenum disulfide
N ₂	Nitrogen gas
Na	Sodium
Na ₂ CO ₃	Sodium carbonate
Na ₂ O	Sodium oxide
NaHCO ₃	Sodium hydrogen carbonate
NaOH	Sodium hydroxide
NH ₄ OH	Ammonium hydroxide
Ni	Nickel
O	Oxygen
OH	Hydroxide
S	Sulfur
Se	Selenium
Si	Silicon

Symbol	Description
Sn	Tin
Sn(OH) ₄	Tin (IV) hydroxide
SnCl ₄	Tin (IV) chloride
SnO ₂	Tin (IV) oxide
SnS	Tin (II) sulfide
SnS ₂	Tin (IV) sulfide
Te	Tellurium
Zn	Zinc
ZnS	Zinc sulfide
ZnSe	Zinc selenide

Chapter 1

Introduction

1.1 Global Warming – the Common Enemy of Human Being

It has just entered 2021 and the news about the global-scale pandemics, extreme weathers and natural disasters bombarded people's visions in the recent years. Date back to the beginning of January 2020, the plane I took descended into Sydney airport through layers of thick smoke which generated from the abnormally intense bushfires, swept across the entire Australia and lasted for months. One of the main causes is the continuous drought and increase in average temperature induced by climate change globally, ¹ as well as the impacts from the El Niño event ² which is intensified by the global warming ³. Between 2019 – 2020, massive forests – the “lung” of the Earth, burned worldwide: tropical rainforests in Amazon, Congo and Queensland, boreal taiga forests in North America and Siberia. Again, the global warming is one of the major factors contributing to these extreme events.

Lenton et al., proposed a concept of “tipping points” ⁴ to describe large-scale subsystems of the Earth system that can be changed, under certain conditions, into a qualitatively different state by small perturbations ⁵. The examples of the typical tipping points are shown in Figure 1.1 ⁶. The loss of these forests is included as the tipping points, which alters their role from carbon sinks to carbon sources, accelerating the emission of gigaton- (Gt-) scale of CO₂ – a type of greenhouse gas – into the atmosphere. Additionally, considerably large volume of greenhouse gases, including CO₂ and CH₄, is releasing from the thawing of permafrost across the Arctic region where the rise of temperature is at least twice as quickly as the global average ⁶. Ice melting in Arctic regions, particular in the Amundsen Sea embayment of West

Antarctica and Greenland ⁷ where the tipping points are approached or even passed, can substantially raise the sea level and threaten the living conditions of the low-lying population centres and the archipelagoes countries. As depicted in Figure 1.1, most of the tipping points are interrelated ⁶. The melting of Greenland and the arctic-sea ice ejects freshwater into the Atlantic Ocean, slowing down the Atlantic circulation which alters the regional climates, such as the destabilization of the West African monsoon and thereby triggering the expansion of Sahara Desert. Moreover, the shallow-water coral bleaching in massive area is another heart-breaking vision, which I witnessed myself at the end of 2018 in Agincourt Reef, a pearl in the Great Barrier Reef. It is only the tip of the iceberg that more than half of the shallow-water corals on the Reef were gone, indicating a profound loss of biodiversity.

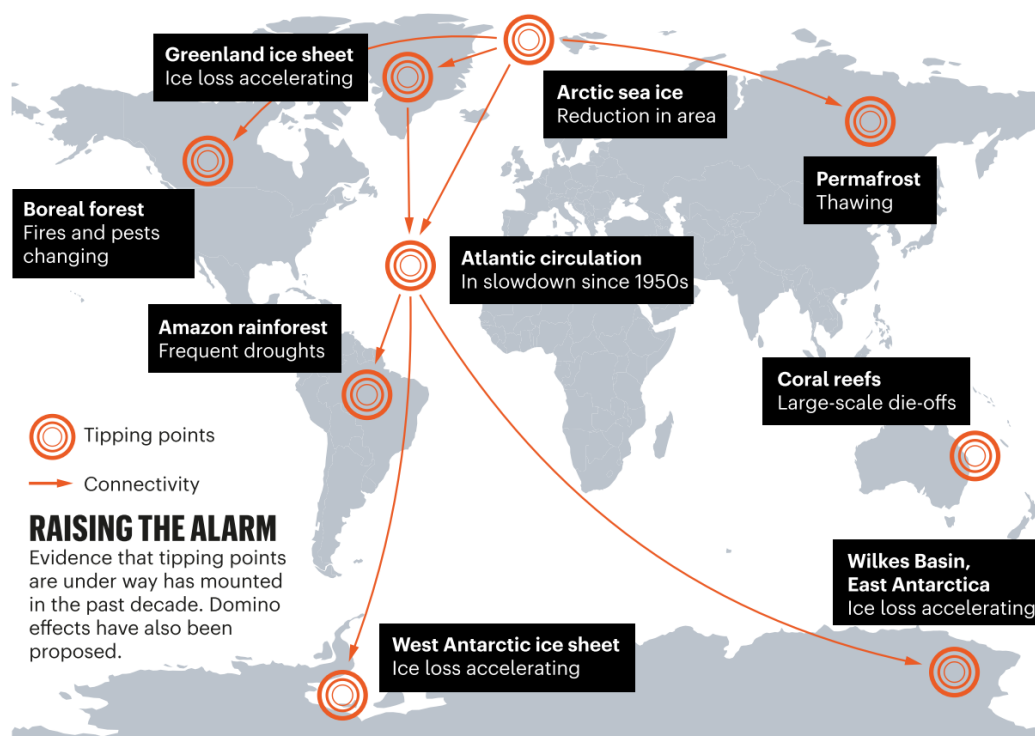


Figure 1.1 Examples of some critical tipping points and the interaction between these points ⁶.

Reproduced with permission ⁶. © 2020 Springer Nature Limited.

Aiming to curtail the rise in global temperatures, the Paris Agreement, as the successor of the expired Kyoto Protocol, chartered in 2015 set a long-term temperature goal that maintains the global average temperature well below 2 °C above pre-industrial levels, and pursues the rise within 1.5 °C ⁸. According to the recent report from the Intergovernmental Panel on Climate Change (IPCC) ^{9,10}, the carbon emissions must be curbed by at least 49% of the levels in 2017 by another decade and the carbon neutrality must be achieved by 2050. To achieve this goal, only 500 Gt of CO₂ can be emitted ⁶. However, big fractions of emission budget are inevitable from the dieback of Amazon and boreal forests (~ 200 Gt ¹¹, without consideration of the dieback from other large forests) and the thaw of permafrost (~100 Gt ¹¹, without consideration of CH₄ emission from deep permafrost or undersea hydrates). In addition to above 40 Gt global emission per year, the remaining budget could be erased already ⁶. Therefore, international action must be taken immediately to save the Earth – our home planet.

1.2 The Energy from the Sun

In order to meet the 1.5 °C target, Grubler et al. ¹² proposed a global scenario, so called “Low Energy Demand” and updated new structures of world energy by demand and by resource, as respectively shown in Figure 1.2a-b. The figures were plotted using the historical data by 2014, projection until 2050 through this model and post 2050 via a simplified scenario model. Based on this projection, electricity demand will be dominant in the global energy consumptions, and solar energy will be the major energy resource by 2050. In contrast to the limited sources of fossil fuels, which originated from the sediments of primeval lifeforms, photons – the gift from the Sun – delivers sustainable energy without restrictions in geography, pollution and green-house gas emissions.

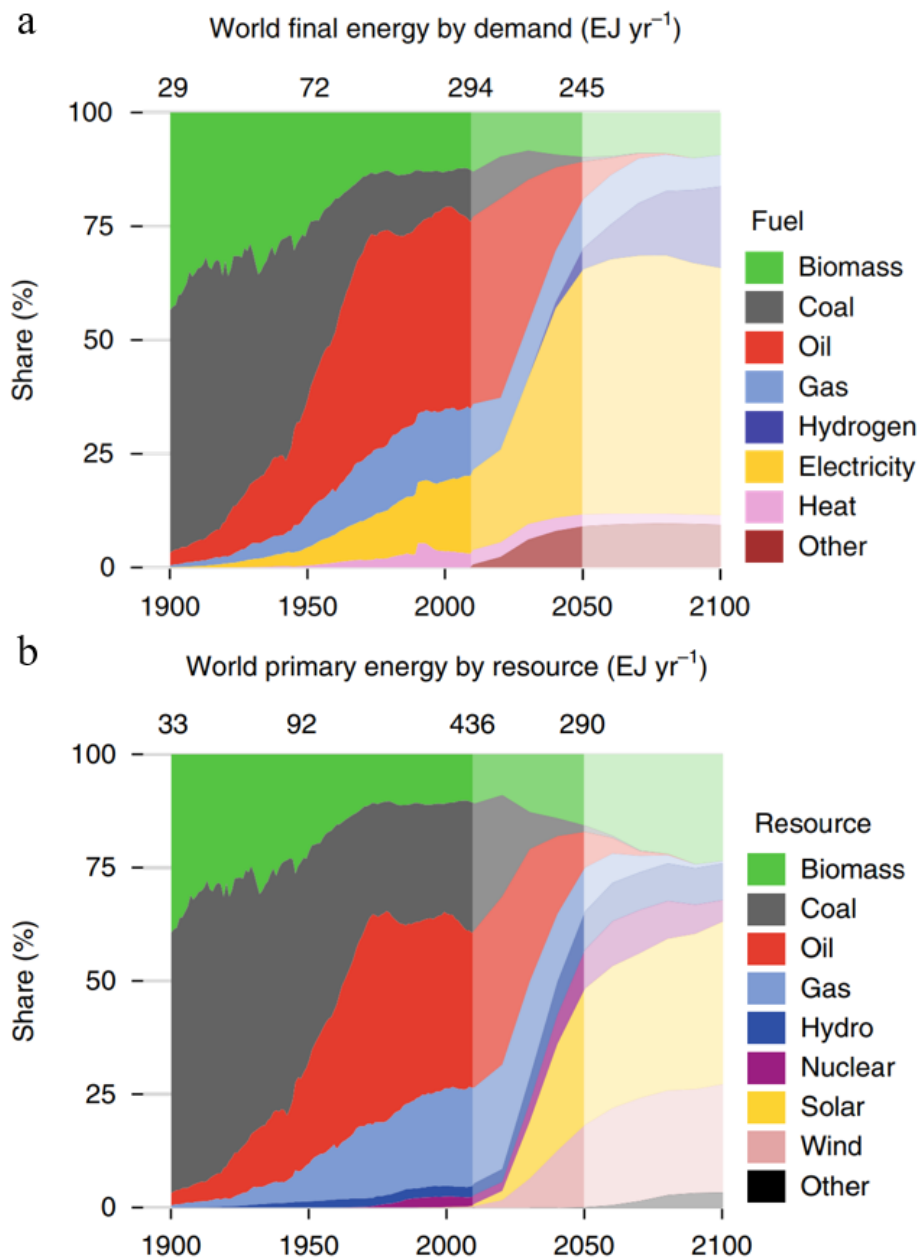
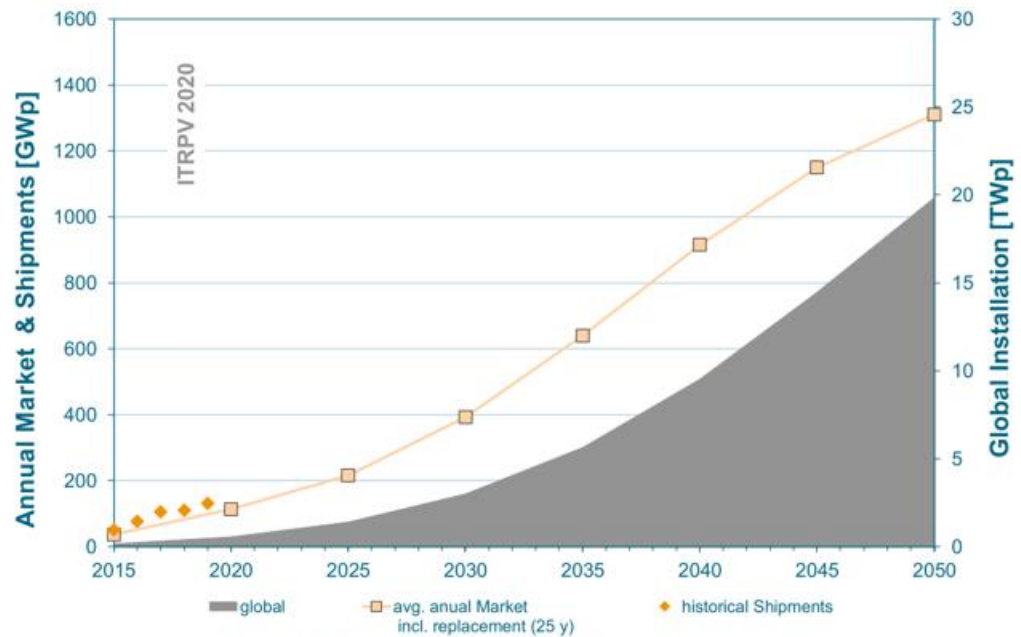


Figure 1.2 a. Final energy shares by fuel. b. Primary energy shares by resource. Constructed via the collection of historical data to 2014 (darkest tint), the Low Energy Demand scenario to 2015 (lighter tint), and simplified scenario extended to 2100 (lightest tint).¹² Reproduced with permission¹². © 2021 Springer Nature Limited.

Photovoltaic (PV) is the most promising sector in solar energy for electricity-generation purpose, which has made great strides in recent decades. As Figure 1.3a illustrated, the global installation and annual market grow exponentially, predicting the global installation of 19.8 TWp by 2050. This projection was proposed based on the assumption of ~20% (31 PWh) of global primary demand fulfilled by PV ¹³, which is adopted in the report of International Technology Roadmap for Photovoltaic 2020 (ITRPV 2020) ¹⁴. Figure 1.3b ¹⁴ presents the learning curve for module price as a function of cumulative shipments. It shows the reduction in the average selling price according to the learning rate of 23.5% as every doubling of cumulative PV module shipment, in consideration of the period from 1976 to 2019. After the end of long-period Si shortage due to the mass production of crystalline silicon (c-Si) PV in China in 2006, the learning rate increases to 40% from this year onward ¹⁴. The cost reduction relies on both of the rapid improvement in conversion efficiencies of solar cells and growing economies of scale in this rapidly expanding market, decreasing the levelized electricity-generation cost to as low as 0.027 – 0.036 USD/kWh ¹⁵, significantly lower than that of coal at 0.05 – 0.13 USD/kWh. Such low cost is thus promoting the dominance of PV in the global energy market, paving the pathway to fulfill the goal of zero net carbon emission by 2050.

a Global PV Installation and corresponding PV market

Progressive scenario (all sectors)



b

Learning curve for module price as a function of cumulative shipments

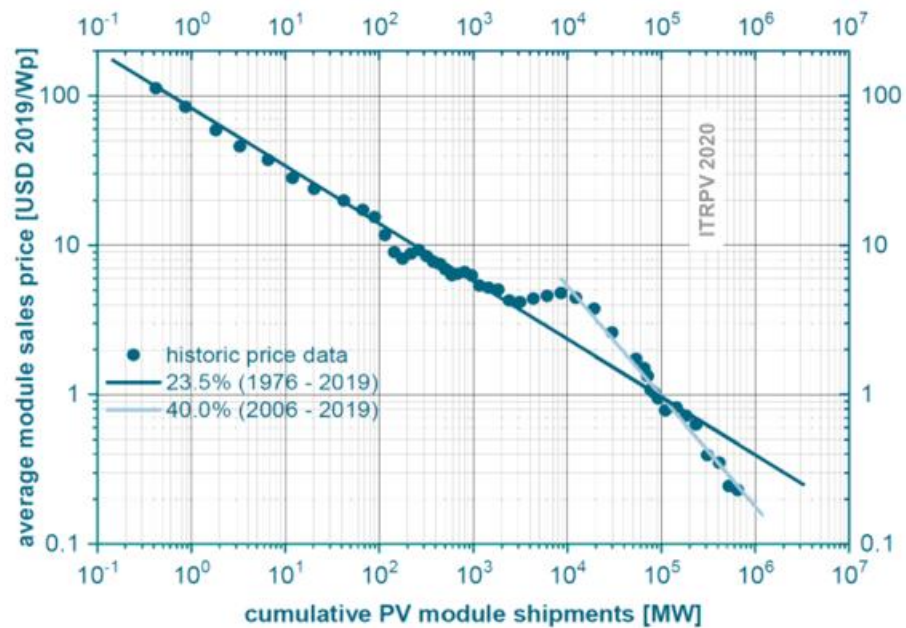


Figure 1.3 a. Annual PV market and corresponding cumulated global installation in 35 years from 2015, including the consideration of replacements after 25 years¹³. b. Learning curve of module spot market price as a function of cumulative PV module shipments from 1976 to 2019. Each spot represents a single year from this range. The calculated learning rates for the

overall period and 2006 to 2019 are marked by straight lines. ¹⁴ Reproduced with permission

¹⁴.

1.3 The Opportunities of Thin Film Solar Cells

Although Si modules dominates the present PV market (> 95% of global market ¹⁶), some of the critical, emerging, high-value markets are underserved or overlooked by the rigid Si modules including aerospace, unmanned aerial vehicles (UAV), micro-integrated products, portable charging, as well as vehicle- (VIPV) and building-integrated photovoltaics (BIPV). Beyond the value of cost, efficiency, and reliability for the standard Si modules, flexibility and portability as two additional value propositions are critical in these booming markets, which can be quantified via specific power with the unit of watts per kilogram ¹⁷.

The emergence of thin film modules has filled the market vacancies with high potential in lower cost, lightweight/high specific power applications. For instance, thin film chalcopyrite Cu(In,Ga)Se₂ (CIGS) grown on flexible stainless steel ¹⁸ or polyimide substrates ^{19,20} can be applied in BIPV, transportation and flexible charging applications. Although technologies based on group III-V elements, with high specific power, have been widely employed in aerospace, their annual production is still far below GW scale. In contrast, both CdTe and CIGS, being forerunners in thin film technologies, have reached GW-scale annual production ¹⁷. Figure 1.4 a&b ¹⁷ reveal the learning curves for the thin film technologies, in comparison with Si. Through examining the historic experience curve in Figure 1.4a, thin-film PV technologies require lower costs at equivalent volumes relative to Si PV. As seen in Figure 1.4b, ~ 8 billion USD was required to reach 1 GW for Si PV, while the costs in CdTe and CIGS were around 1 billion USD. Analysis through combining these two figures, reduction

of the cost to 1 USD/W costed 155 billion USD for Si PV, but 2 billion and 0.4 billion would consume for CdTe and CIGS technologies, respectively.

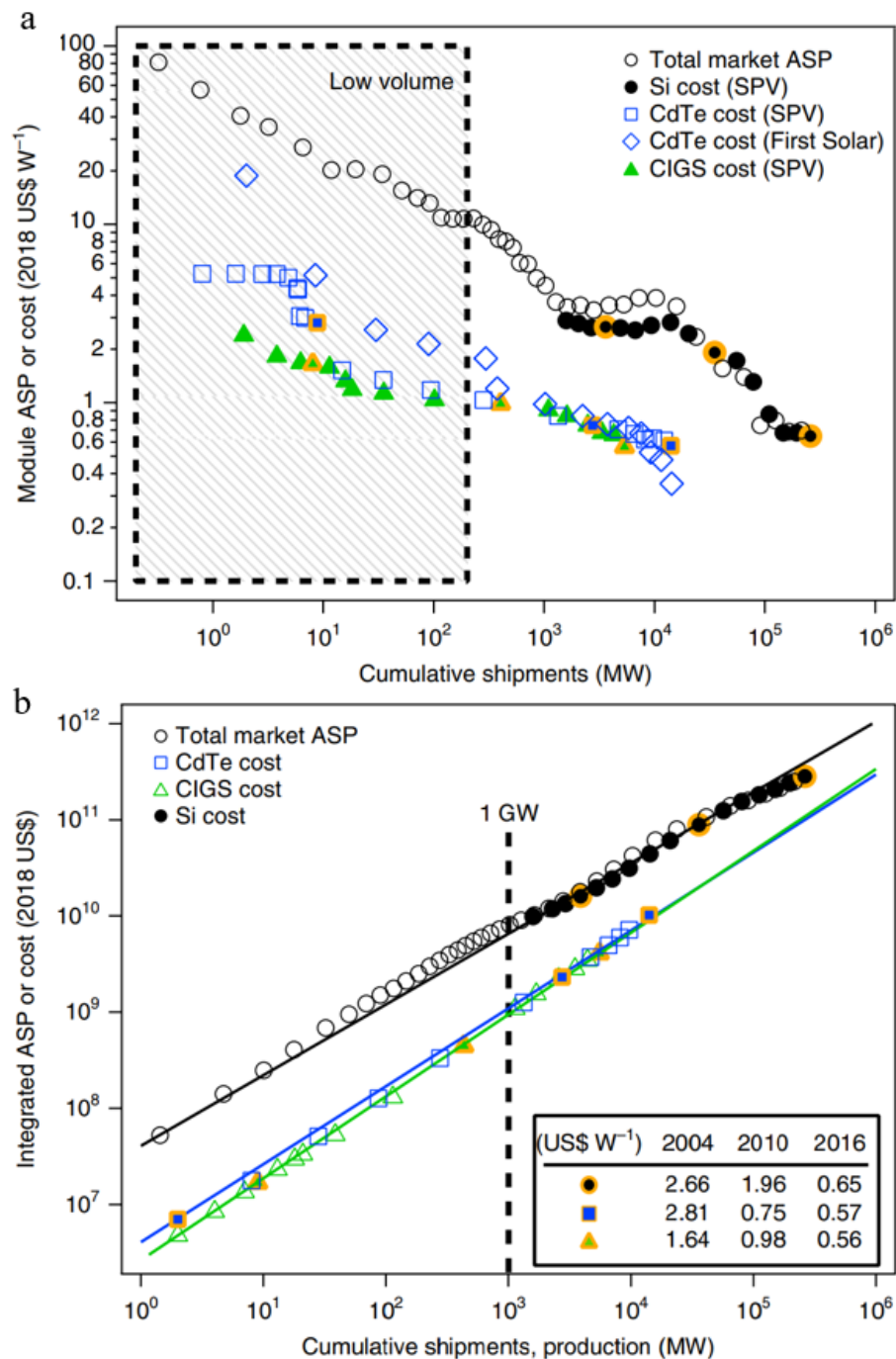


Figure 1.4 Learning curves for GW-scale PV technologies. a. Historic experience curve of module production costs from Solar PV Market Research (SPV), First Solar costs from quarterly reports, and total market average selling price (ASP) as a function of global

cumulative shipments.¹⁷ b. Integrated experience curve of integrated ASP or cost as a function of cumulative shipments. The occurrence of 1 GW of cumulative shipments is denoted in the dashed vertical line.¹⁷ Reproduced with permission¹⁷. © 2021 Springer Nature Limited.

Possessing the advantages of flexibility, high specific power, compatibility of wide variety of substrates makes the thin film technologies practicable in BIPV (tiles, facades, windows, etc.), VIPV, and product-integrated PV (PIPV, such as bus canopy, wearable products²¹), as well as portable charging and micro-integrated products (e.g., used in Internet of Things (IoT)). Furthermore, due to the colour tunability through controlling the optical interference from the thickness of the top layers²², thin film technologies can also be employed in PV applications with aesthetic requirements.

1.4 Kesterite $\text{Cu}_2\text{ZnSnS}_4$ (CZTS) Photovoltaics – a Promising Thin Film Technology

Previous section introduced the advantages of thin film solar cells in general. CdTe and CIGS photovoltaics, as forerunners in thin-film fields, have reached the conversion efficiency beyond 22 and 23 %, respectively^{23,24}. However, the terawatt-scale demand would not be satisfied due to the limitations of these champion thin film photovoltaics in the toxicity of Cd and the scarcity of Te and In in the Earth's Crust²⁵. Among a wide range of alternative thin film candidates, kesterite $\text{Cu}_2\text{ZnSnS}_4$ (CZTS), as a derivative from CIGS semiconductor, is of particular interest due to the following preferential features:

1. Favourable direct band gap (E_g) of ~ 1.5 eV with high absorption coefficient beyond 10^4 cm^{-1} ²⁶, which is suitable as a top cell with lower E_g semiconductor (such as Si) as bottom cell in tandem cell application.
2. Abundance of constituent elements in the Earth's Crust (Cu: 25 ppm, Zn: 71 ppm, Sn: 5.5 ppm²⁷, S: 260 ppm²⁸, much larger than 0.05 ppm In²⁵ exploited in CIGS solar cells).
3. Non-toxic element constituents.
4. Durability of physical properties.
5. E_g can be tuned by alloying with extrinsic elements, such as Ag²⁹, Cd³⁰, Ge³¹, Se³², etc.

In terms of the raw material cost, CZTS is only $\sim 20\%$ of CIGS and $\sim 5\%$ of CdTe³³. If considering the ultrathin thickness (~ 800 nm) of CZTS used in PV devices, the material cost will be much lower. Additionally, the adoptable commercialized CIGS modules³⁴ will further reduce the manufacture cost of the CZTS counterpart.

1.5 Thesis Objectives – Healing the Heterojunction

The biggest obstacle to push kesterite CZTS into the market entry is the poor conversion efficiency, at 11.01% ³⁵, significantly lags behind that of champion chalcopyrite solar cell at 23.35% ²⁴. Among the deficiencies of device performance parameters, the open circuit voltage (V_{oc}) deficit (defined as $E_g/q - V_{oc}$) is the main factor restricting the improvement of conversion efficiency.

To elucidate the deficiency in V_{OC} , Gunawan et al., revealed that kesterite solar cells suffer from strong recombination loss at the buffer/absorber heterointerface, using the temperature-dependent V_{OC} measurement^{36,37}. Figure 1.5³⁶ shows the linear relation of V_{OC} and temperature (T)³⁸ for CIGS (denoted as CIGS-A) and CZTSSe cells. The CZTSSe cells with two different E_g were used, marked as CZTSSe-A (1.05 eV) and CZTSSe-B (1.21 eV). In contrast to the CIGS counterpart, both CZTSSe cells have significantly lower E_A relative to their E_g , indicating that the recombination mechanism is strongly influenced by the recombination at the buffer/absorber heterointerface³⁶. This gives rise to the large V_{OC} deficit.

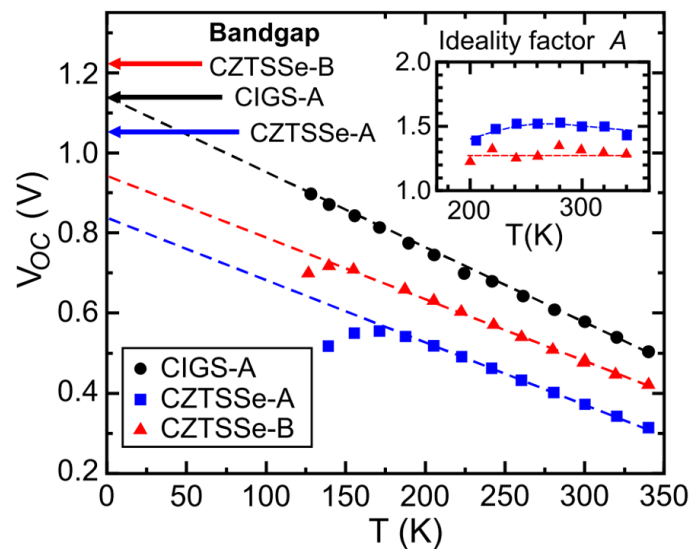


Figure 1.5 V_{OC} as a function of temperature. The activation energy E_A of the recombination process is derived from the intercept of V_{OC} axis by the linear extrapolation to 0 K. CZTSSe cells have lower E_A than their E_g (those of CZTSSe-A and CZTSSe-B are 1.05 and 1.21 eV, respectively.) In contrast, the value is equivalent to E_g (1.14 eV) for CIGS-A cell. The inset shows the plot of ideality factor A as a function of temperature.³⁶ Reproduced with permission³⁶. © 2021 AIP Publishing LLC.

The motivation of this thesis is to develop innovative post-deposition treatment methods at the as-formed CZTS surface to “cure” the CdS buffer/CZTS absorber heterointerface and the heterojunction. These treatments after the formation of CZTS films are defect-oriented, and thus providing effective outcomes through targetedly removing/deactivating the imperfections presented in the as-formed CZTS surface or within the heterojunction region.

1.6 Thesis Outline

This thesis is comprised of 7 chapters. In Chapter 1, the global issues that motivate this research in PV are presented. The advantages of thin film PV, particularly kesterite CZTS materials are introduced, followed by the objectives and outline of this thesis.

Chapter 2 begins with the introduction of properties of kesterite compounds and reaction equilibrium, deep into the loss mechanisms and the related approaches, providing a justification for the research objectives in this thesis. This is followed by the introduction of device fabrication applied in this thesis.

In Chapter 3, an ultrathin stannic oxide (SnO_2) intermediate layer was applied to passivate the CZTS/CdS heterointerface. The effectiveness of passivation was evidenced by photoluminescence characterization. This treatment results in an improvement of conversion efficiency from 6.82 to 8.47 %, with the major contribution from V_{oc} and FF improvement.

Chapter 4 introduces a novel post-annealing method – moisture-assisted post-deposition annealing (MAPDA) to modify the heterojunction through controllable reduction in Na

density within CZTS layer, and in turn facilitating the spontaneous Cd diffusion during the CdS deposition at 70 °C. The modified elemental distributions significantly reduce the density of deep-level defects at the heterointerface, create preferable shallow acceptor defects and promote the conversion efficiency to 8.67 %.

In Chapter 5, a champion efficiency of 9.40 % was obtained using a follow-up heterojunction annealing (HJA) in the air at 150 °C, showing further modified elemental distributions, particularly strengthened Cd diffusion and replenishment of sacrificed Na induced by MAPDA. Significant alleviation of SRH recombination was observed at the heterojunction region of the combined MAPDA- and HJA-cells. Furthermore, CdS changes due to these post-annealing treatments are discussed.

Chapter 6 provides in-depth analyses of the promising MAPDA and HJA treatments with the aid of nanoscale optoelectronic characterization techniques. Kelvin probe force microscopy (KPFM) and conductive-atomic force microscopy (C-AFM) measurements are used to study the optoelectronic properties of CZTS surface with excessive Na and K. We utilized the KPFM-based surface photovoltage (SPV) measurement for investigating the nanoscale V_{OC} change due to MAPDA and HJA and provided the nanoscale V_{OC} maps. SPV measurement at low photon injection was also conducted for revealing the excellent effects of SRH recombination mitigation. Eventually, we exploited the light intensity-dependent SPV measurement to explore the optoelectronic variations of the CdS layer due to these post-annealing treatments.

In Chapter 7, the conclusions drawn from this work and their implications and contributions to photovoltaics are presented, followed by suggestions and outlooks for the future work.

1.7 Reference

- 1 Van Oldenborgh, G. J. *et al.* Attribution of the Australian bushfire risk to anthropogenic climate change. *Natural Hazards and Earth System Sciences Discussions*, 1-46 (2020).
- 2 Wang, G. & Cai, W. Two-year consecutive concurrences of positive Indian Ocean Dipole and Central Pacific El Niño preconditioned the 2019/2020 Australian “black summer” bushfires. *Geoscience Letters* **7**, 1-9 (2020).
- 3 Ham, Y.-G. El Niño events will intensify under global warming. *Nature* **564**, 192-193 (2018).
- 4 Lenton, T. M. *et al.* Tipping elements in the Earth's climate system. *Proceedings of the national Academy of Sciences* **105**, 1786-1793 (2008).
- 5 Lenton, T. M. Early warning of climate tipping points. *Nature climate change* **1**, 201-209 (2011).
- 6 Lenton, T. M. *et al.* Climate tipping points — too risky to bet against. *Nature* **575**, 592-595 (2019).
- 7 Hock, R. *et al.* IPCC Special Report on the Ocean and Cryosphere in a Changing Climate. *IPCC - Intergovernmental Panel on Climate Change*, 131-202 (2019).
- 8 Rogelj, J. *et al.* Paris Agreement climate proposals need a boost to keep warming well below 2 C. *Nature* **534**, 631-639 (2016).
- 9 Masson-Delmotte, V. *et al.* Global warming of 1.5 °C. *An IPCC Special Report on the impacts of global warming of 1.5 °C*, 1-9 (2018).
- 10 Tollefson, J. IPCC says limiting global warming to 1.5 °C will require drastic action. Report No. 0028-0836, 172-173 (Nature, 2018).
- 11 Steffen, W. *et al.* Trajectories of the Earth System in the Anthropocene. *Proceedings of the National Academy of Sciences* **115**, 8252-8259 (2018).

- 12 Grubler, A. *et al.* A low energy demand scenario for meeting the 1.5 °C target and sustainable development goals without negative emission technologies. *Nature energy* **3**, 515-527 (2018).
- 13 Hoffmann, W. & Metz, A. in *Proceedings of the 36th European Photovoltaic Solar Energy Conference, Marseille, France*. 9-13.
- 14 Fischer, M.. *et al.* International Technology Roadmap for Photovoltaic – ITRPV 2019 Results (11th Edition). *ITRPV* (2020).
- 15 Maisch, M. Solar electricity can retail for \$0.027-0.036/KWh as renewables close in on global grid parity. *PV Magazine* (2019).
- 16 Feldman, D. & Margolis, R. Q4 2019/Q1 2020 Solar Industry Update. (National Renewable Energy Lab (NREL), Golden, CO, United States (2020).
- 17 Reese, M. O. *et al.* Increasing markets and decreasing package weight for high-specific-power photovoltaics. *Nature Energy* **3**, 1002-1012 (2018).
- 18 Reinhard, P. *et al.* Review of progress toward 20% efficiency flexible CIGS solar cells and manufacturing issues of solar modules. *2012 IEEE 38th Photovoltaic Specialists Conference (PVSC) PART 2*. 1-9 (2012).
- 19 Chirilă, A. *et al.* Potassium-induced surface modification of Cu (In, Ga) Se 2 thin films for high-efficiency solar cells. *Nature materials* **12**, 1107 (2013).
- 20 Chirilă, A. *et al.* Highly efficient Cu (In, Ga) Se 2 solar cells grown on flexible polymer films. *Nature Materials* **10**, 857-861 (2011).
- 21 Min, J.-H. *et al.* Flexible high-efficiency CZTSSe solar cells on diverse flexible substrates via an adhesive-bonding transfer method. *ACS applied materials & interfaces* **12**, 8189-8197 (2020).

- 22 Cho, D. H., Lee, W. J., Kim, M. E., Shin, B. & Chung, Y. D. Color tuning in Cu (In, Ga) Se₂ thin-film solar cells by controlling optical interference in transparent front layers. **28**, 798-807 (2020).
- 23 Green, M. A. *et al.* Solar cell efficiency tables (version 56). *Progress in Photovoltaics: Research and Applications* **28**, 629-638 (2020).
- 24 Nakamura, M. *et al.* Cd-free Cu (In, Ga)(Se, S) ₂ thin-film solar cell with record efficiency of 23.35%. *IEEE Journal of Photovoltaics* **9**, 1863-1867 (2019).
- 25 Taylor, S. R. & McLennan, S. M. The continental crust: its composition and evolution. *N.P.* (1985).
- 26 Persson, C. Electronic and optical properties of Cu₂ZnSnS₄ and Cu₂ZnSnSe₄. *Journal of Applied Physics* **107**, 053710 (2010).
- 27 Mitzi, D. B., Gunawan, O., Todorov, T. K., Wang, K. & Guha, S. The path towards a high-performance solution-processed kesterite solar cell. *Solar Energy Materials and Solar Cells* **95**, 1421-1436 (2011).
- 28 Katagiri, H. *et al.* Development of CZTS-based thin film solar cells. *Thin Solid Films* **517**, 2455-2460 (2009).
- 29 Wang, D. *et al.* Formation of the front-gradient bandgap in the Ag doped CZTSe thin films and solar cells. *Journal of Energy Chemistry* **35**, 188-196 (2019).
- 30 Su, Z. *et al.* Cation substitution of solution-processed Cu₂ZnSnS₄ thin film solar cell with over 9% efficiency. *Advanced Energy Materials* **5**, 1500682 (2015).
- 31 Ford, G. M., Guo, Q., Agrawal, R. & Hillhouse, H. W. J. C. o. M. Earth abundant element Cu₂Zn (Sn_{1-x}Ge_x) S₄ nanocrystals for tunable band gap solar cells: 6.8% efficient device fabrication. **23**, 2626-2629 (2011).

- 32 Riha, S. C., Parkinson, B. A. & Prieto, A. L. Compositionally Tunable Cu₂ZnSn (S_{1-x}Se_x)₄ Nanocrystals: Probing the Effect of Se-Inclusion in Mixed Chalcogenide Thin Films. *Journal of the American Chemical Society* **133**, 15272-15275 (2011).
- 33 Wadia, C., Alivisatos, A. P. & Kammen, D. M. Materials availability expands the opportunity for large-scale photovoltaics deployment. *Environmental science & technology* **43**, 2072-2077 (2009).
- 34 Feurer, T. *et al.* Progress in thin film CIGS photovoltaics—Research and development, manufacturing, and applications. *Progress in Photovoltaics: Research and Applications* **25**, 645-667 (2017).
- 35 Yan, C. *et al.* Cu₂ZnSnS₄ solar cells with over 10% power conversion efficiency enabled by heterojunction heat treatment. *Nature Energy* **3**, 764-772 (2018).
- 36 Gunawan, O., Todorov, T. K. & Mitzi, D. B. Loss mechanisms in hydrazine-processed Cu₂ZnSn (Se, S)₄ solar cells. *Applied Physics Letters* **97**, 233506 (2010).
- 37 Todorov, T. K. *et al.* Beyond 11% efficiency: characteristics of state-of-the-art Cu₂ZnSn (S, Se)₄ solar cells. *Advanced Energy Materials* **3**, 34-38 (2013).
- 38 Nadenau, V., Rau, U., Jasenek, A. & Schock, H. Electronic properties of CuGaSe₂-based heterojunction solar cells. Part I. Transport analysis. *Journal of Applied Physics* **87**, 584-593 (2000).

Chapter 2

Backgrounds

2.1 Properties of Kesterite Compounds

2.1.1 Structure of Kesterite Compounds

Kesterite quaternary compound is one of the various categories of chalcogenide family, in the formula of $\text{Cu}_2\text{M}^{\text{II}}\text{M}^{\text{IV}}\text{Ch}^{\text{VI}}_4$, where M^{II} and M^{IV} are divalent (Zn, Cd, Mn, Fe, Co, Ni) and tetravalent metals (Sn, Ge, Si), respectively, and Ch represents a chalcogen (S, Se, Te) ¹. The formation of the quaternary compound can be regarded as the result of sequential cation mutation through maintaining the overall neutral charge, according to the theory developed by Goodman ² and Pamplin ³. Figure 2.1a displays the evolution of quaternary kesterite compound CZTS from the binary ZnS and the ternary CIS compounds. The derivation of these structures is shown in Figure 2.1b ⁴. The cation mutations upon the zinc-blend binary II-VI semiconductor can generate two possible structures with the lowest energies – the chalcopyrite structure and the CuAu structure, dependent on the group I and III atoms ordering. In contrast to the parent binary compound, with the aid of enhanced structural and chemical freedom, the ternary semiconductors possess more flexible properties, exhibiting a much lower band gap (E_g) which is favourable for photovoltaic application. Based on the rule of charge neutrality and structures with the lowest energies, a ternary semiconductor can have three possible structures: kesterite (derived from chalcopyrite structure), stannite and PMCA (generated from CuAu structure). First-principles calculations revealed by Chen et al. ⁵ that the kesterite structure has lower energy than the stannite structure, with a binding energy difference at around 3 meV/atom ⁶. The experimental evidence also confirmed the kesterite structure of CZTS films via X-ray diffraction (XRD) results, showing the diffraction

peaks at (112), (200), (220/204), (312/116), (002), (008), (101), (103), (105), (110), (211), (213), (224) and (332) while (112) is the preferred orientation, which is commonly observed⁷⁻¹⁰.

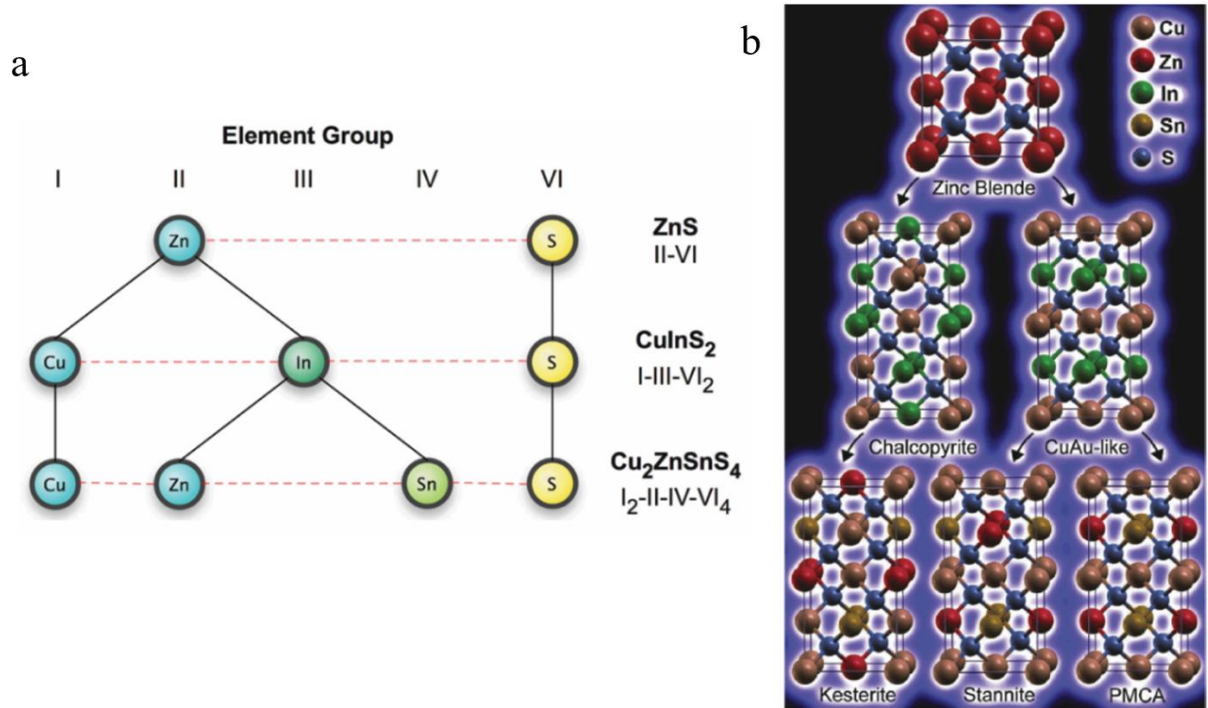


Figure 2.1 a. Evolution of quaternary kesterite from binary to ternary and quaternary semiconductors¹¹. b. The crystal structures of the corresponding multinary semiconductors with lowest formation energies⁴. Reproduced with permission⁴. © 1999-2021 John Wiley & Sons, Inc.

2.1.2 Band Structure and Properties from the First-Principles Modeling

The band structure of kesterite CZTS shown in Figure 2.2a-b^{12,13} calculated via the all-electron and full-potential linearized augmented plane wave (FP-LAPW) method^{12,14}, using the generalized gradient approximation (GGA) plus an onsite Coulomb interaction U_d for the Cu-d states¹³, the full band parameterization and the parabolic band approximation. Like CIGSe, CZTS is a direct-gap semiconductor with E_g at around 1.5 eV¹⁵⁻¹⁷. In contrast to the

most semiconductors, no coupling between the lowest conduction band (CB) in CZTS and the other nearest bands occurs at the Brillouin Zone (BZ) edge, due to the low crystalline symmetry. This results in a relatively flat band dispersion at the bottommost CB and thereby yields small indirect E_g (2.2 and 1.7 eV for the CBM at the $(0,1,0) = (0,0,1)$ and $(1,1,2) = (1,1,0)$ BZ edge, respectively). The direct E_g is also small for k-points away from the Γ -point due to a relatively flat valence band maximum (VBM) accompanied with relatively flat lowest CB, indicating a higher density of states (DOS) present near the band edges which could enhance the optical absorption. However, it may limit the electronic transport due to relatively larger effective electron and hole masses in the vicinity of Γ -point, compared to CIGSe compounds¹⁸.

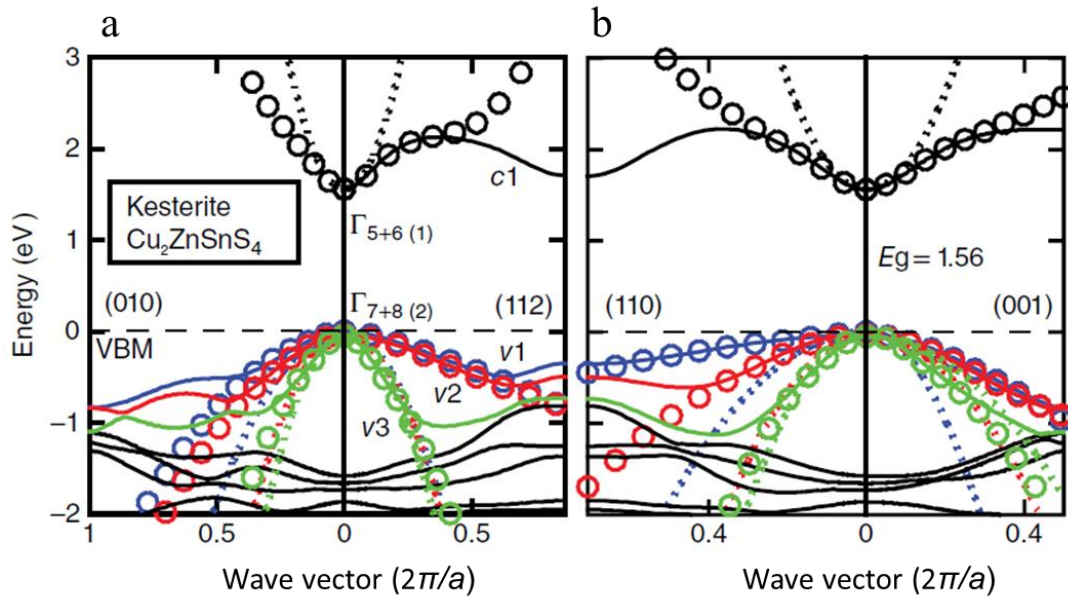


Figure 2.2 The electronic band structure of kesterite CZTS along four symmetry directions, referring to the valence band maximum (dashed lines). The spin-orbit interaction is considered, but the index of valence bands (v1 as topmost valence band, v2, and v3) and the lowest conduction band (c1) refers to spin-independent bands. Energy bands in solid and dotted lines are obtained from the generalized gradient approximation/full-potential linearized augmented plane wave calculations and the parabolic band approximation,

respectively. The results shown in the open circles are derived from the full band parameterization.^{12,13} Reproduced with permission¹³. © 1999-2021 John Wiley & Sons, Inc.

The flat valence bands (VBs) at around -1 eV are contributed to the Cu *d*-like bands, as shown in the atom-resolved DOS distributions of kesterite CZTS (Figure 2.3). The distributions are calculated by the GW_0 method with partial self-consistency and frequency-dependence¹². The significance relies on the broad energy range of the VBs for the hybridization between Cu $3d^{10}$ and S $3p^4$ bands and thereby determining the DOS near the VBM, partially affected by the other cations Zn-*p* and Sn-*sp* bonding with the anion S-*p* bands. As the DOS distributions shown, the lowest CB is determined by the antibonding states of Sn-*s* and S-*p* states. As abovementioned, the bottommost CB of CZTS does not involve degeneration with other closest CBs, resulting in more localized energy bands. Therefore, the E_g can be easily tuned through shifting the Sn-determined CBM by alloying Sn sites with other group-IV elements (such as Ge¹⁹⁻²¹).

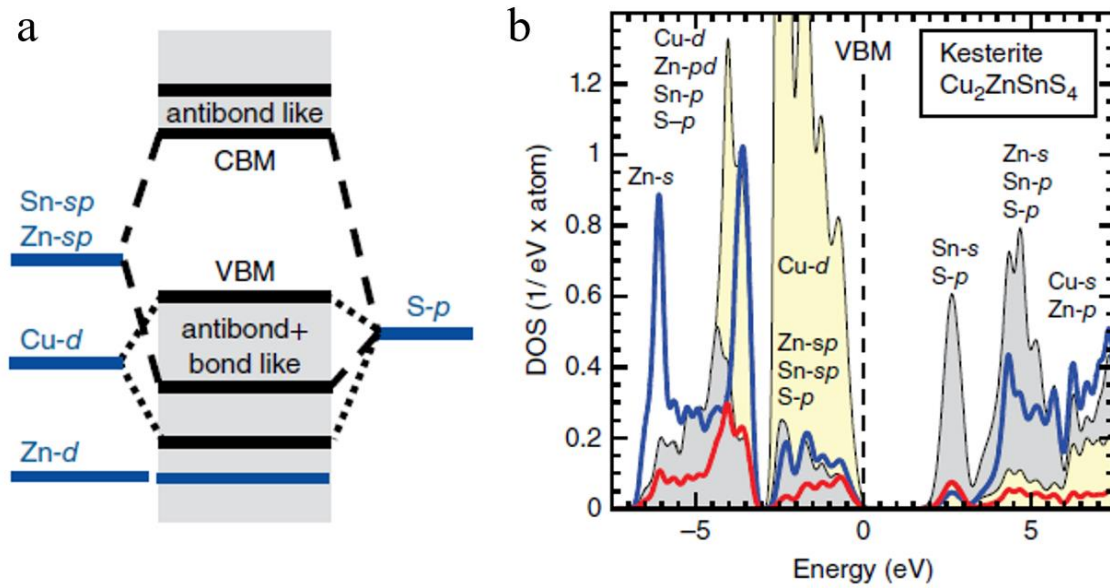


Figure 1.3 a. Schematic illustration of the band edges in CZTS ¹³. b. Atomic- and angular-momentum resolved density of state distributions of kesterite CZTS ¹². Reproduced with permission ¹³. © 1999-2021 John Wiley & Sons, Inc.

As a p-type semiconductor, the doping of CZTS stems from the large density of Cu-related states. V_{Cu} and Cu_{Zn} are generally considered as the major doping contributors in p-type kesterite absorbers, according to the First-principles calculations ^{22,23}, while Cu_{Zn} has a deeper energy level than that of V_{Cu} ²⁴. However, the formation energy of V_{Cu} (~ 0.57 eV) is much larger than that of Cu_{Zn} in kesterite absorbers (~ 0.01 eV) ²⁴, which is reported in a wide composition range ²³. Therefore, Cu_{Zn} is believed to be the dominant defect contributing to the doping level ²⁴⁻²⁸.

2.1.3 Optical Properties from the First-Principles Modeling

The optical absorption coefficient can be directly derived from the complex dielectric function (i.e. $\epsilon_0(\omega) = \epsilon_1(\omega) + i\epsilon_2(\omega)$) by using the equation

$$\varepsilon_1^{\alpha\beta}(\omega)^2 + \varepsilon_2^{\alpha\beta}(\omega)^2 = \left[\varepsilon_1^{\alpha\beta}(\omega) + \frac{\alpha^{\alpha\beta}(\omega)^2 c^2}{2\omega^2} \right]^2 \quad (2.1)$$

where c is light speed and the expressions of the real part ($\varepsilon_1^{\alpha\beta}(\omega)$) and the imaginary part ($\varepsilon_2^{\alpha\beta}(\omega)$) of the dielectric functions are not mentioned here for brevity²⁹. The average absorption coefficient profiles for the kesterite and the stannite CZTS and CZTSe are presented in Figure 2.4a-b^{12,13}. Since the absorption is dependent on the dielectric response and the latter is also affected by the joint DOS, some local features in the absorption coefficient curves can be related to the DOS peaks mentioned above. For instance, the peaks at around 3.25 and 2.50 eV, as illustrated as black dotted lines in Figure 2.4a, corresponds to the DOS peaks (Figure 2.3b) induced by Sn-s and chalcogen-p, respectively¹³. The absorption coefficient for high energy photons among all four compounds is similar, considering the E_g difference at around 0.5 eV. A close-up of absorption coefficient near- E_g was plotted in Figure 2.4b where the energy scale is shifted by $\hbar\omega - E_g$. CZTS has a higher absorption coefficient than CZTSe, which could be related to the relatively flat bands at the Γ -points. Furthermore, the intrinsic absorption in CZTS nearly doubles that in GaAs and ZnSe. Such strong absorption in CZTS enables over 90% of incident light (regardless of reflection loss) absorbed by 1-2 μm CZTS absorber³⁰.

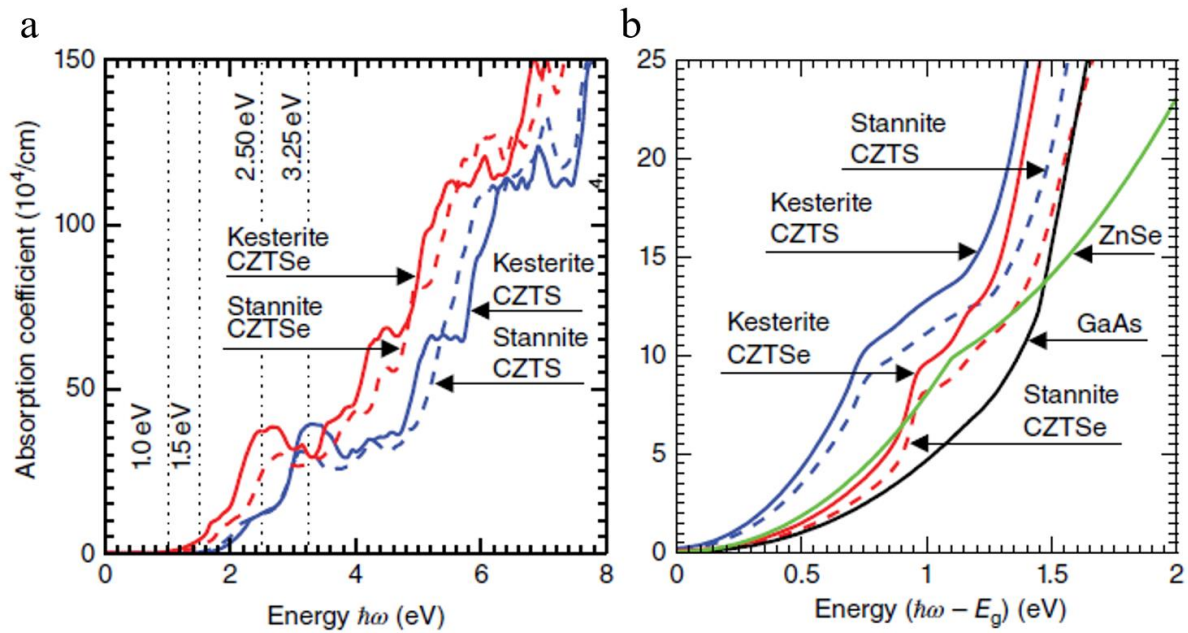
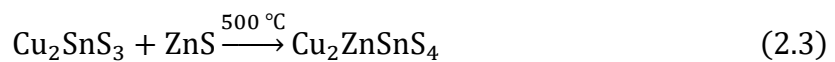


Figure 2.4 Absorption coefficient of a. CZTS and CZTSe as a function of photon energy. b. Close-up of absorption coefficient of CZTS(e), GaAs, and ZnSe as a function of photon energy shifted by E_g , aiming to compare the absorption for materials with different E_g .^{12,13} Reproduced with permission¹³. © 1999-2021 John Wiley & Sons, Inc.

2.2 Kesterite Reaction Equilibrium

Different reaction routes of kesterite films during sulfurization or selenization have been reported based on the deposition techniques and precursor compositions³¹⁻³⁷. This thesis only involves the compound precursors through a sputtering process for pure sulfide CZTS semiconductors. The relevant reaction equilibrium in this thesis could take the following reaction route as a reference³⁶:



2.3 Loss Mechanisms and the Relevant Approaches

2.3.1 Voc Deficit – the Major Bottleneck of Kesterite Solar Cell Development

Through comparing the device performance of the champion kesterite solar cells with the champion chalcogenide solar cells, such as CdTe, CIGSSe solar cells, and other forerunners in thin-film photovoltaics ³⁸, it is not hard to observe that the large V_{OC} deficit, expressed as $E_g - V_{OC}/q$ (where q is the unit charge), is the most significant limitation in the current kesterite solar cells. Considering the Shockley-Queisser (SQ) limit of the CZTS solar cell with E_g of 1.5 eV, the SQ limits for V_{OC} , J_{SC} and FF are 1210 mV, 29 mA/cm² and 91 %, respectively ³⁹, whereas these parameters of the current 11 % champion CZTS device only reached 730 mV, 21.7 mA/cm² and 69.3 %, respectively ⁴⁰, equivalent to 60.3 %, 74.8 % and 76.2 % of the corresponding SQ limit values. Our simulation results ⁴¹ based on baseline device with PCE ~ 7 % demonstrate that Voc loss at the interfaces is the main culprit of such large Voc deficit, occupying more than 50 % of overall Voc loss.

The deficit in V_{OC} is believed primarily arisen from the severe Shockley-Reed-Hall (SRH) recombination associated with the unfavourable defects ⁴²⁻⁴⁴ at the heterointerface, the space charge region, the neutral charge region and the detrimental band alignment at CZTS/CdS heterointerface ^{39,45}. To date, zero-, two-, and three-dimensional defects have been intensively studied in the literature, including point defects, heterointerfaces and grain boundaries, voids and secondary phases, respectively. The defects involved in this thesis are discussed in this section. The detrimental band alignment at the heterointerface is included in section 2.3.3. Strategies to address the issues arisen from the detrimental defects are introduced accordingly.

2.3.2 Zero-Dimensional Defects

Zero-dimensional defects, or point defects, are formed through the disturbance of a crystal structure at isolated sites (including vacancies, interstitials, and anti-sites) or aggregation into isolated defect clusters. In terms of a quaternary compound, kesterite compounds involve more intrinsic lattice defects relative to those of binary and ternary compounds which have been well studied, including vacancies (V_{Cu} , V_{Zn} , V_{Sn} and V_S), interstitials (Cu_i , Zn_i , Sn_i and S_i), antisites (Cu_{Zn} , Zn_{Cu} , Zn_{Sn} , Sn_{Zn} , Cu_{Sn} , etc.) As mentioned hereinbefore, the doping concentration and electrical conductivity are believed mainly contributed by Cu_{Zn} , while the formation energies and ionization energy levels of other acceptor-like defects are relatively higher. Additionally, all donor-like defects have relatively high formation energy. However, as shown in Figure 2.5a, the donor-like defects (Zn_{Cu} , Sn_{Zn} , V_S , etc.) can be ionized and decrease the formation energy to a lower value when the Fermi level is close to VBM. When considering the optimal compositions with Cu depletion and Zn enrichment, the formation energies of V_{Cu} and Zn_{Sn} are decreased while those of Cu_{Zn} and Sn_{Zn} are, in turn, increased. Zn_{Sn} , as a deep acceptor (Figure 2.5b), is unfavourable in kesterite photovoltaic devices. V_S was regarded as deep donor-like states. If V_S forms accompanied with S loss during the sulfurization process, the oxidization of S would result in the reduction of Sn ($Sn^{4+} \rightarrow Sn^{2+}$)⁴⁶ and therefore yielding more Sn^{2+} related defects. Based on the first-principles calculation performed by Walsh et al.⁴³, the charge of V_S can be nullified through obtaining electrons from the reduction of Sn, resulting in a donor level lying below the VBM. Whereas it, in turn, can be excited to charged V_S donors through capturing holes and creating deep donor defects within the E_g , providing an efficient nonradiative recombination channel within the CZTS layer, together with the reduced Sn^{2+} -related defects. Above that, Sn_{Zn} deep donor has also been identified as the origin of persistent electron trapping/de-trapping in kesterite sulfide CZTS devices⁴³.

The charged defects can be partially compensated through the formation of neutral defect clusters due to Coulomb attraction between the acceptor- and the donor-like point defects. Among the likely formed defect clusters, $[\text{Cu}_{\text{Zn}} + \text{Zn}_{\text{Cu}}]$ has the lowest formation energy (Figure 2.6a), leading to a high population and thereby inducing the partial disorder of Cu and Zn on cation sites ²³. High concentration of $[\text{Cu}_{\text{Zn}} + \text{Zn}_{\text{Cu}}]$ clusters were used to be considered as the source of band tailing ⁴². However, the impact of these clusters on the band structure is weak (Figure 2.6b), which can be regarded as benign defect clusters. In contrast, the formation of clusters of $[\text{Cu}_{\text{Sn}} + \text{Sn}_{\text{Cu}}]$, $[\text{Zn}_{\text{Sn}} + \text{Sn}_{\text{Zn}}]$, $[\text{Sn}_{\text{Zn}} + \text{V}_{\text{Zn}}]$, $[\text{Sn}_{\text{Zn}} + 2\text{V}_{\text{Cu}}]$ and $[\text{Sn}_{\text{Zn}} + 2\text{Cu}_{\text{Zn}}]$ are detrimental and significantly decrease the E_g . If the off-stoichiometric compositions with Zn enrichment and Cu depletion are applied, these defects could be limited. Instead, both $[\text{V}_{\text{Cu}} + \text{Zn}_{\text{Cu}}]$ and $[\text{Zn}_{\text{Sn}} + 2\text{Zn}_{\text{Cu}}]$ antisite pairs have decreased formation energy, which are favourable within the CZTS layer without large impacts on the band structure ²³.

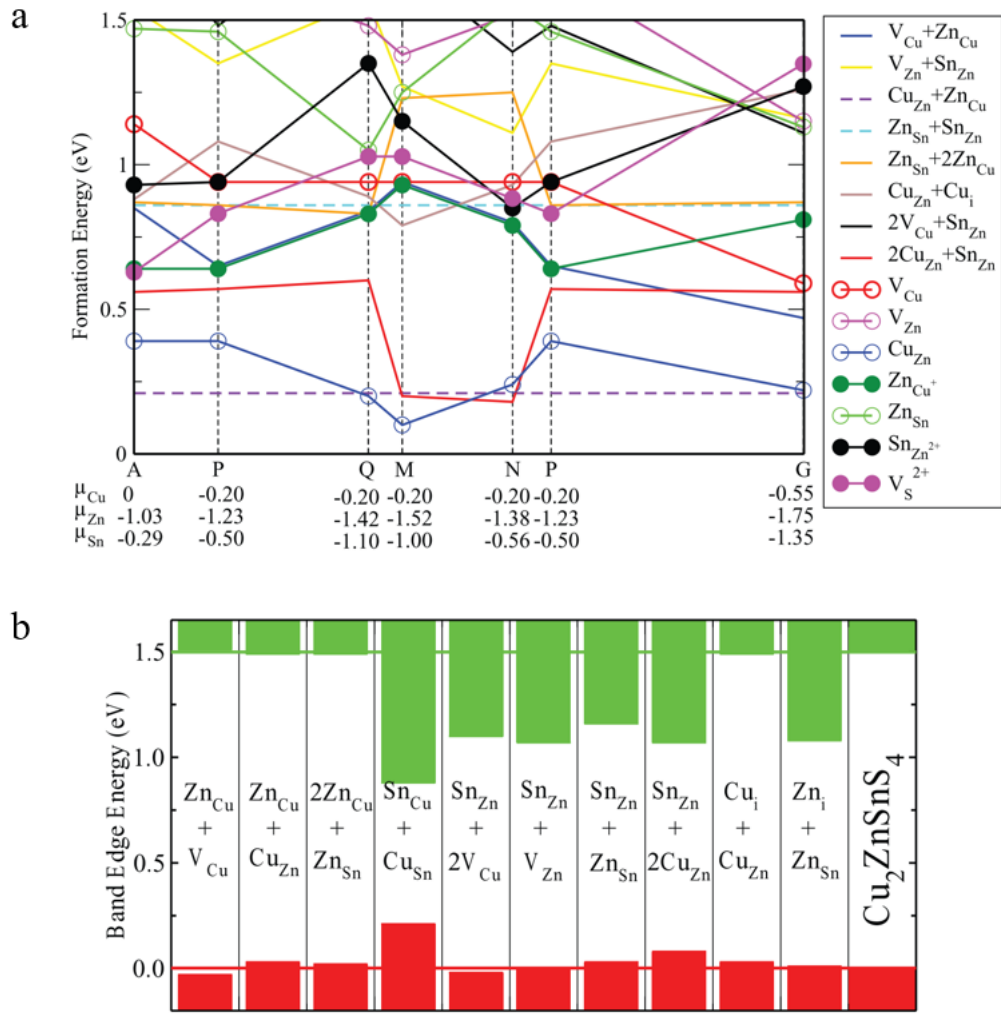


Figure 2.6 a. The calculated formation energy of point defects and defect clusters in a relatively low ionization energy in CZTS as a function of the chemical potential along the boundary surrounding the stable CZTS phase region presented in this citation ²³ and also found in Figure 2.10. The states of acceptor, donor and neutral clusters are marked in open, solid, and straight lines, respectively. b. The calculated band shifts of conduction (green) and valence (red) bands arisen from different defect clusters in CZTS where the defect density used as one defect cluster in per 128-atom supercell. ²⁵ Reproduced with permission ²³. © 1999-2021 John Wiley & Sons, Inc.

The band tailing problem is considered as one of the major factor limiting the V_{oc} improvement ⁴². The schematic diagram in Figure 2.7a shows the formation of band tails within CZTS materials. Under the condition with high defect density, the impurity band merges with the valence band maximum and thus reducing the E_g . As shown in Figure 2.7b, the cause of band tailing can originate from either the electrostatic potential fluctuation induced by high defect density with a high degree of compensation but without strong impacts on the E_g , or the E_g fluctuation arisen from crystalline or compositional inhomogeneities ⁴⁷, or the E_g fluctuation caused by a high density of the defect clusters as mentioned above. Rey et al. found that the E_g fluctuation is the cause of the band-edge fluctuation, with the aid of temperature- and excitation-dependent photoluminescence technique ⁴⁸. The Cu-Zn disorder was considered as the main source of the large band tailing. However, the increased Cu-Zn disorder obtained from the heat treatment did not reveal any differences in band tailing ⁴⁸. Instead, the prevention of the formation of those defect clusters which have large impacts on the E_g , as abovementioned, is critical to reducing the band tailing.

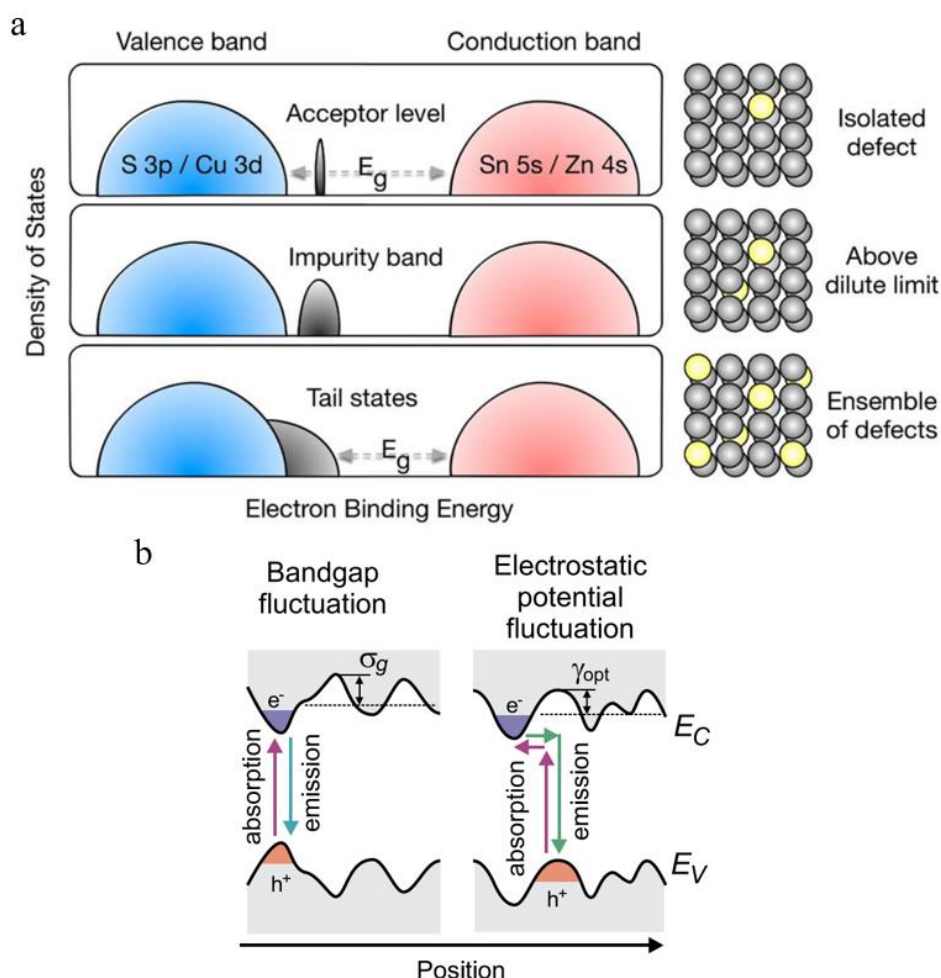


Figure 2.7 a. Schematics showing defect energy level originated from isolated acceptor defects broadening to an impurity band with the increased defect density, until the formation of tail states in the presence of sufficiently high defect density.⁴⁹ b. Schematics of bandgap fluctuation and electrostatic potential fluctuation.⁴² Reproduced with permission^{49,42}. © 2021 American Chemical Society, © 2021 AIP Publishing LLC.

Approaches for reducing the band tailing have been widely reported through elemental substitution by extrinsic isovalent elements into CZTS layers, such as Cu by Ag⁵⁰, Zn by Cd⁵¹ and Ba⁵² as well as Sn by Ge^{19,53,54}. Furthermore, the suppression of detrimental intrinsic defects and defect clusters was achieved by controlling the oxidation states of cations (Cu and

Sn) during the growth of CZTSe films by using a soft-selenization process ²⁸. Relying on this approach, the current champion efficiency at 12.5 % of the CZTSe solar cell was obtained.

2.3.3 Two-Dimensional Defects

It has been reported that significant SRH recombination occurs at the CdS/CZTS heterointerface regions, through temperature-dependent V_{OC} measurement, revealing lower activation energy (E_a) at 0 K than the E_g of CZTS absorber layer ^{40,55}. The large SRH recombination at the heterointerface was induced by the intensive undercoordinated atoms (dangling bonds) originated from the surface relaxation of both CZTS and CdS films, the lattice mismatch between these layers (~7 % mismatch), and by the unfavourable band alignment ^{16,45}. The heterointerface or surface recombination losses can be reduced using two different passivation strategies ⁵⁶ – chemical passivation and field-effect passivation, where the former aims to reduce the interface defect density induced by dangling bonds, and the latter is used to reduce the free carrier concentration at the interface region via a built-in electric field. Most post-treatments used for passivation of CZTS/CdS heterointerface can be considered as the mixed passivation strategies. For instance, Cd incorporation within the heterojunction not only reduces the defect density, but also optimizes the band alignment at the heterojunction ⁴⁰. Besides the field-effect passivation effect, the application of the atomic-layer-deposited (ALD) Al_2O_3 passivation layer can facilitate Na diffusion at the heterointerface, which also plays a critical role to passivate the local defects via a built-in field ⁵⁷.

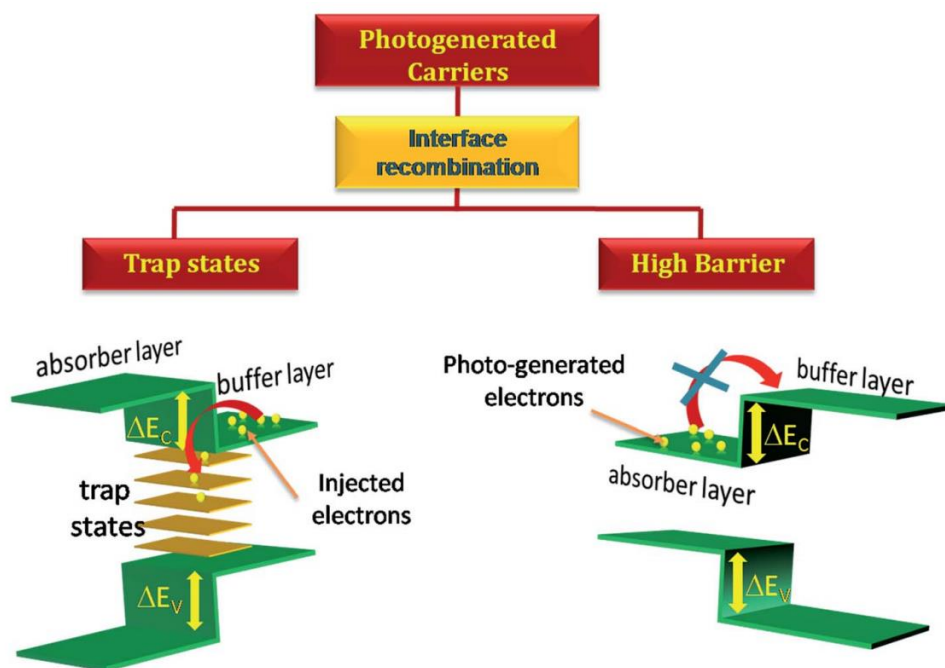


Figure 2.8 Schematics of the recombination mechanisms of photo-generated electrons at two types of conduction band offset (CBO) at absorber/buffer heterointerface: “cliff”-like and “spike”-like CBOs are demonstrated in the left- and right-hand sides, respectively.⁵⁸ Reproduced with permission⁵⁸. © Royal Society of Chemistry 2021.

In pure sulfide CZTS solar cells, the “cliff”-like conduction band offset (CBO) formed by bringing CZTS and CdS with relatively higher electron affinity together^{16,45,59}. This type of CBO gives rise to a significantly large SRH recombination rate⁶⁰, as depicted in Figure 2.8⁵⁸. High potential barrier (> 0.4 eV)⁶⁰ resulted from a “spike”-like CBO also strengthens the interface recombination due to the weaker charge separation. To tackle this problem, alternative buffer layers, such as $\text{Zn}_{1-x}\text{Cd}_x\text{S}$ ⁶¹ and ZnSnO ⁶²⁻⁶⁴ with smaller electron affinity, were applied to replace the conventional CdS buffer, demonstrating the significant reduction of V_{OC} deficit. Furthermore, the band alignment at the heterojunction region can also be modified through elemental grading (such as Ag grading at the front)⁶⁵⁻⁶⁷ or Cd alloying through a heterojunction heat treatment^{40,63}.

Being another kind of 2D defects, grain boundaries (GB) or GB core, in terms of the narrow definition, can be regarded as two adjoining lattices where the lattice symmetries are interrupted in a spatial distance < 1 nm. However, the defects, disordered region, segregated impurities, and diffused elements can spread tens of nanometers from the GB core^{68,69}. The accumulation of charged defects at GBs results in various local potential, even in different band bending directions when opposite charges trapped, as shown in Figure 2.9a-b. Simulation results^{70,71} reveal that an upward band bending benefits photovoltage and a downward bending contributes to the carrier collection, whereas the latter can increase the recombination rate. In most thin-film forerunners, such as CIGS and CdTe semiconductors, large downward bending at GBs is generally observed⁷²⁻⁷⁶, even involved type inversion. Therefore, this bending type forms minority-carrier collection channels and exhibits enhanced carrier collection. On the other hand, the real scenario is complex that the local chemistry change has strong impacts on the E_g near GBs. For instance, Cu-enriched GBs in CIGS films can lift the local valence band maximum⁷⁷, resulting in poorer carrier collection⁷². Xiao et al. reported the band edge positions for both CB and VB at GBs of different kesterite materials using scanning tunnelling spectroscopy⁷⁸. The opposite bending direction of CB and VB away from the forbidden gap was observed in Se-enriched GBs of CZTSe and CZTSSe materials. However, detrimental inward bending was found in pure sulfide CZTS materials, resulting in enhanced carrier recombination. Different band bending directions at GBs of kesterite materials have been reported^{57,79-83}, which could be arisen from the variation of local compositions by the diffusion of either intrinsic^{77,84,85} or extrinsic elements^{82,86}. As one of the critical trace elements, Na accommodation at GBs is widely observed^{40,87,88}, increasing the donor states density and thereby contributing to lower local work function⁷³. However, different local chemical compositions may result in the accumulation

of different types of charges, overwhelming the impacts from Na with a much lower concentration, which could alter the bending direction.

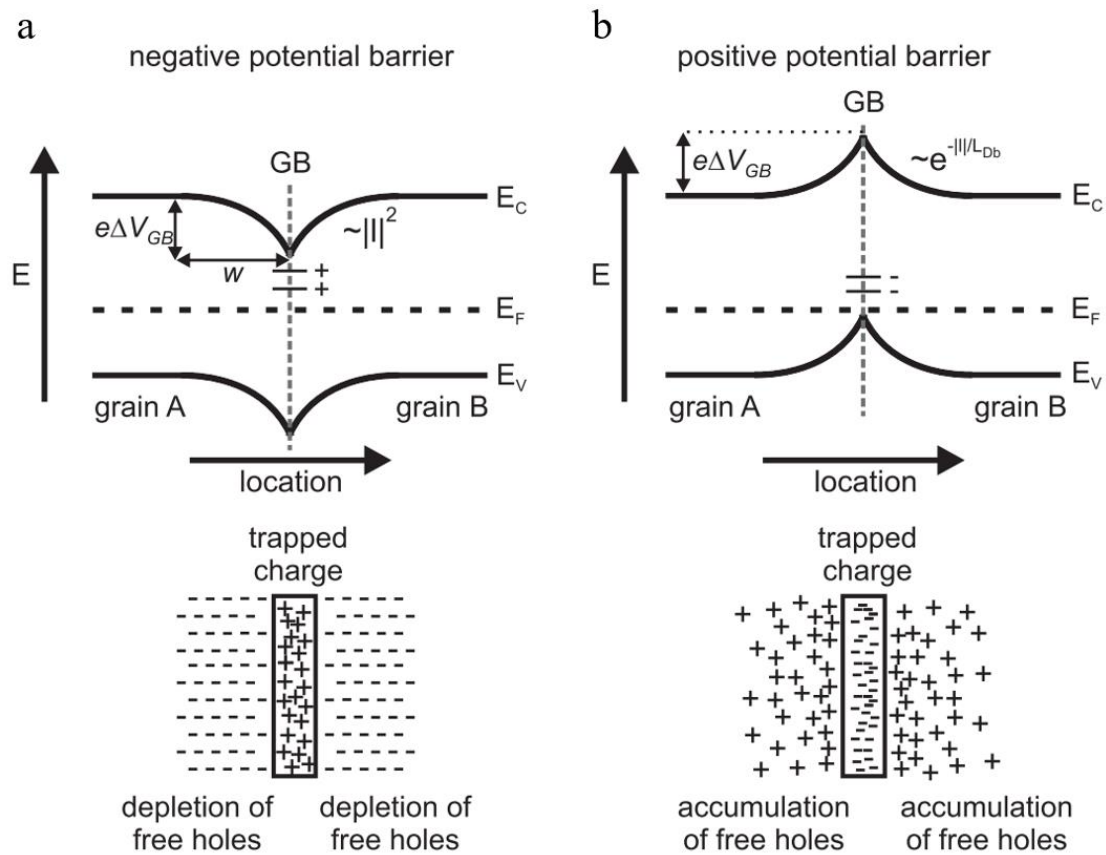
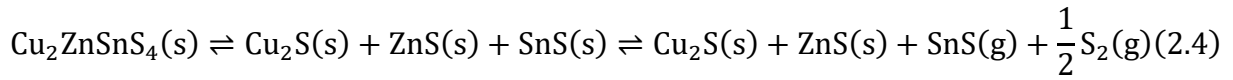


Figure 2.9 Electronic band diagrams in the vicinity of GBs of p-type semiconductors for a. negative and b. positive potential barriers. Specific charge compensation mechanisms are presented in the schematics below.⁸⁹ Reproduced with permission⁸⁹. © 2014 Elsevier B.V.

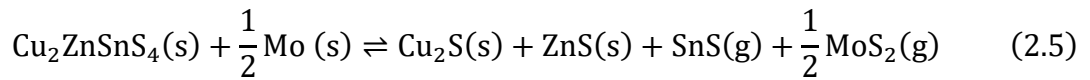
2.3.4 Three-Dimensional Defects

The three-dimensional defects in kesterite solar cells primarily include voids/pinholes and secondary phases, involving the change of a crystal pattern over a finite volume. The voids are generally believed to be the vacancy remainders from the evaporation of volatile SnS phases from the CZTS films. The formation of such secondary phases can be induced by the improper compositions of constitutional elements within the precursor materials, and by the

decomposition of CZTS under improper S₂ and SnS partial pressure ⁴⁶. The decomposition of CZTS can be expressed in the following equation ^{90,91}:



Apart from the self-decomposition of the CZTS films, the energetically favourable reaction between the CZTS and the underlying Mo contact can also result in the CZTS decomposition, as shown in the following equation ⁹¹,



Therefore, void-free and pinhole-free CZTS films can be obtained through using the optimal compositions (Cu/Sn ~ 1.75 – 1.8 and Zn/Sn ~ 1.15 – 1.2 ^{23,92-94}), using proper S₂ and SnS partial pressure during the sulfurization process and applying an intermediate barrier layer via an interface deactivation strategy at the rear interface between CZTS and Mo ⁹⁵⁻⁹⁹.

As the phase diagram in Figure 2.10 shown, the stable phase region of CZTS against Cu₂S, CuS, ZnS, SnS, SnS₂ and Cu₂SnS₃ is very narrow as depicted in the shaded area. Therefore, the formation of these secondary phases seems inevitable for growing CZTS films. In addition to the abovementioned mechanisms accompanied with SnS phases, ZnS can easily form due to the optimal but off-stoichiometric (Zn-rich and Cu-depleted) compositions. Using catalyzed chemical etching method ¹⁰⁰, nanoscale ZnS domains with a median diameter of 80 nm were detected within the CZTS grains, not only as the commonly observed at the front and the rear surfaces.

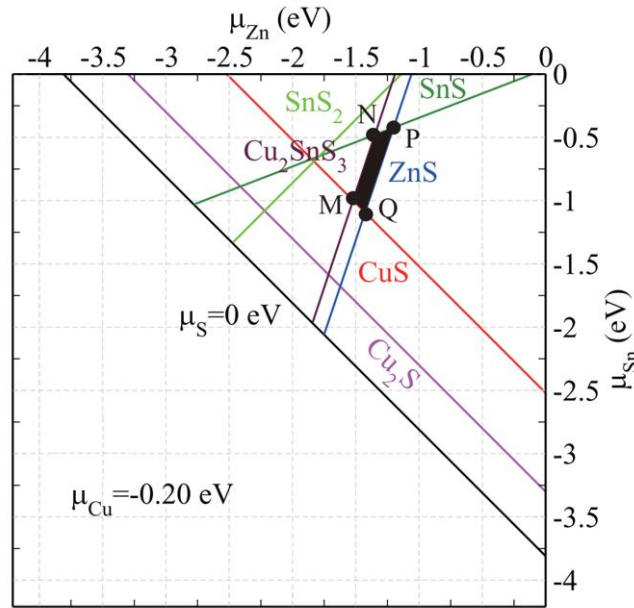


Figure 2.10 The calculated stable chemical-potential region (in black polygon) of CZTS phase in Zn and Sn chemical potential planes at Cu chemical potential of -0.20 eV.^{23,24}

Reproduced with permission²³. © 1999-2021 John Wiley & Sons, Inc.

The formation of these secondary phases can deteriorate the device performance in different ways associated with the E_g of these phases. In general, the secondary phases with lower E_g than CZTS will limit the V_{OC} of the solar cell, such as low- E_g SnS (at 1.0 eV indirect and 1.3 eV direct^{101,102}), Cu_2SnS_3 (at 1.0 eV¹⁰³) and highly conductive Cu_2S (at 1.2 eV¹⁰⁴) phases. By contrast, those with higher E_g are much less detrimental, such as ZnS (at 3.7 eV¹⁰⁵) phases, whereas the existence of too much ZnS phases can increase the series resistance, and even worse, block the transport. Moreover, the formation of MoS_2 from the reaction with sulfur or CZTS¹⁰⁶ is of importance to provide quasi-ohmic contact with high work function, but MoS_2 with too many thickness yields high series resistance and thus deteriorates the device efficiency.

2.4 Fabrication of CZTS Solar Cells

Fabrication of kesterite absorber layers have been reported using a great variety of techniques, including magnetron sputtering ¹⁰⁷⁻¹⁰⁹, evaporation ¹¹⁰⁻¹¹², pulsed laser deposition ¹¹³, hydrazine-based solution process ^{55,114,115}, sol-gel process ¹¹⁶⁻¹¹⁹, spray pyrolysis ¹²⁰, inkjet printing ¹²¹ and successive ionic layer adsorption and reaction ^{122,123}, w/ or w/o a follow-up chalcogenization process. The highest efficiencies of kesterite solar cells reported to date are 12.60 % using extremely toxic and hazardous hydrazine-based process ¹¹⁴ and 12.62 % obtained employing harmless magnetron sputtering ¹²⁴. Regarding pure sulfide CZTS solar cell, which is the scope of this thesis work, we reported 11.01% champion efficiency using hydrazine-free magnetron sputtering technique ⁴⁰.

Figure 2.11 shows the process flow of CZTS solar cells at the University of New South Wales (UNSW). The key technique (approx. half of the overall processes) is the magnetron sputtering (AJA International, Inc., model ATC-2200), as a physical vapour deposition (PVD) technique, allowing mass production of high-quality thin films. In physics, sputtering is a phenomenon when microscopic particles are ejected from the surface of the desired solid materials (i.e., target materials), facilitated from the bombardment by energetic particles of the plasma (ionized Ar⁺ used in this thesis work). The ejected micro-particles deposit on the oppositely mounted substrate under high vacuum condition ($\sim 10^{-7}$ Torr). Both direct current (DC) and radio frequency (RF) current supplies were used for metal targets and insulator/semiconductor targets, respectively. The former can generate a high deposition rate, and the latter can be used to eliminate the electrical breakdown and discharge arcs induced by charge accumulation at the surface of poorly conductive targets. The addition of a magnetic field aims to enhance the plasma-target collision rate, and thus increase the deposition rate.

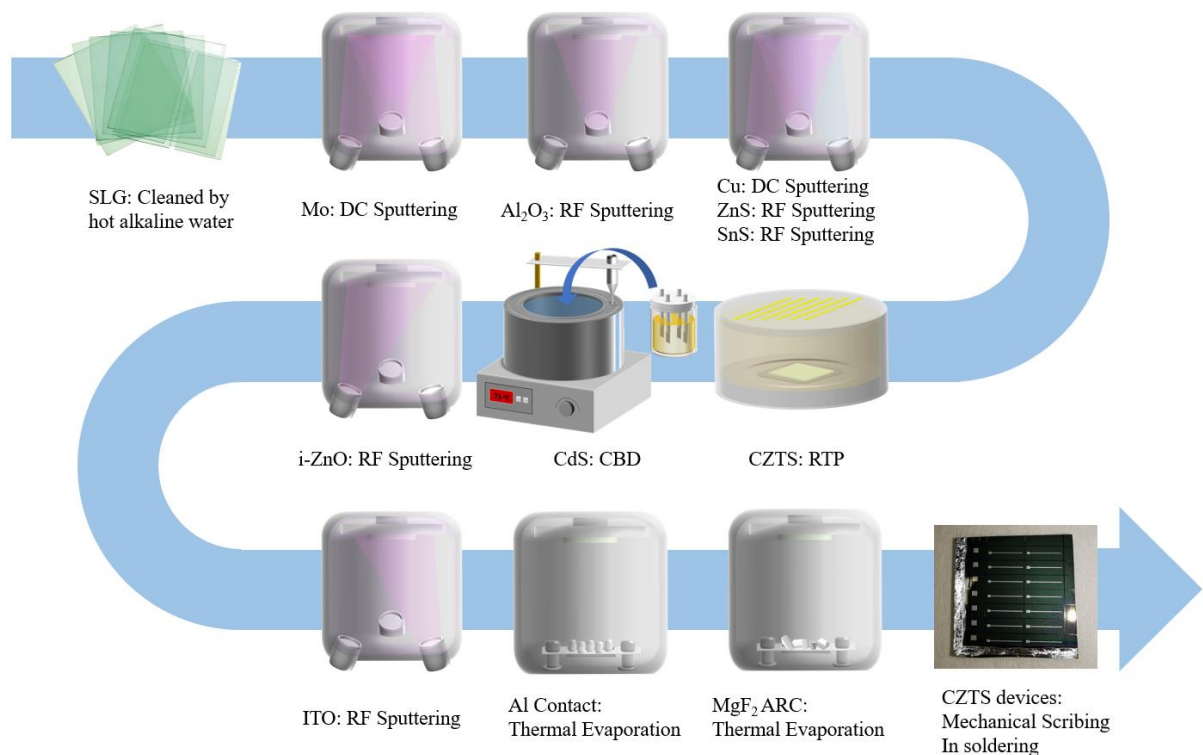


Figure 2.11 The process flow of CZTS solar cells fabricated at University of New South Wales

The structure of the typical CZTS device fabricated in UNSW is shown in Figure 2.12. The fabrication process starts from cleaning soda-lime glass (SLG) in hot alkaline water, followed by deposition of Mo using DC sputtering. The conventional double Mo layers were employed: the bottom layer has relatively higher resistivity which has matched the thermal expansion coefficient with the underlying SLG. A bottom layer with a thickness of 200 nm was deposited at 15 mTorr, and a 600 nm-thick top layer was coated at 1.5 mTorr, using Ar as the working gas. An ultrathin (~ 2 nm) Al_2O_3 intermediate layer was employed using RF sputtering at 1.5 mTorr, to partially inhibit the formation of MoS_2 and to simultaneously prevent the decomposition of the CZTS at the rear, thereby limiting the formation of voids

and secondary phases ⁹⁵. CZTS absorbers were fabricated using the “two-step” method ¹²⁵ – alloy precursor deposition followed by sulfurization, which was well developed and employed in chalcopyrite solar cells. At the initial step, the CZTS alloy precursor was prepared by co-sputtering Cu (DC), ZnS (RF) and SnS (RF) under 1.5 mTorr. The deposition rates were adjusted through input power to confine the off-stoichiometric compositions with Cu/Sn ratio in a range of 1.75 – 1.80 and Zn/Sn ratio in 1.15 – 1.20. The duration was chosen to determine precursor thickness of ~500 nm, aiming to obtain the final sulfurized CZTS film thickness of 700 – 800 nm. Targets used in this process were 3 inch in diameter and impurities on a scale of 99.99 % (4 N). Sulfurization, as the second step, was processed using a Rapid Thermal Processor (RTP, AS-One 100) within combined sulphur and SnS atmosphere at a peak temperature at 560 °C for 3 minutes. The ramping and cooling rates were controlled at 10 and 30 °C/min, respectively. CdS buffer layer was then deposited by chemical bath deposition (CBD) method using the precursor solution of CdSO₄ (0.16 mol/L), thiourea (1.6 mol/L) and aqueous ammonia (1.2 mol/L) at 75 °C for 7 min. After that, a thin (~60 nm), high-resistivity intrinsic ZnO (i-ZnO) layer was fabricated via RF sputtering with a 3-inch target at 3 mTorr using a slow ramping rate to prevent the bombardment damage of the heterojunction. An indium tin oxide (ITO) layer was deposited using a 3-inch target by RF sputtering at 1.5 mTorr. 240 nm ITO layer was fabricated to obtain the sheet resistance lower than 30 Ω/sq. Aluminium (Al) contact was evaporated via thermal evaporation with a height of ~2.5 μm. The aspect ratio, together with the spacing, were designed in consideration of the sheet resistance of the ITO layer and the optical loss from shading. MgF₂ layer with a thickness of 91 – 100 nm was thermally evaporated to form an anti-reflection coating (ARC). The desired thickness aims to minimize the reflection loss at 550 nm. The device finished by mechanical scribing and indium (In) soldering to isolate the unit cells and to form the rear contact, respectively. The defined unit cell area was ~0.23 cm².

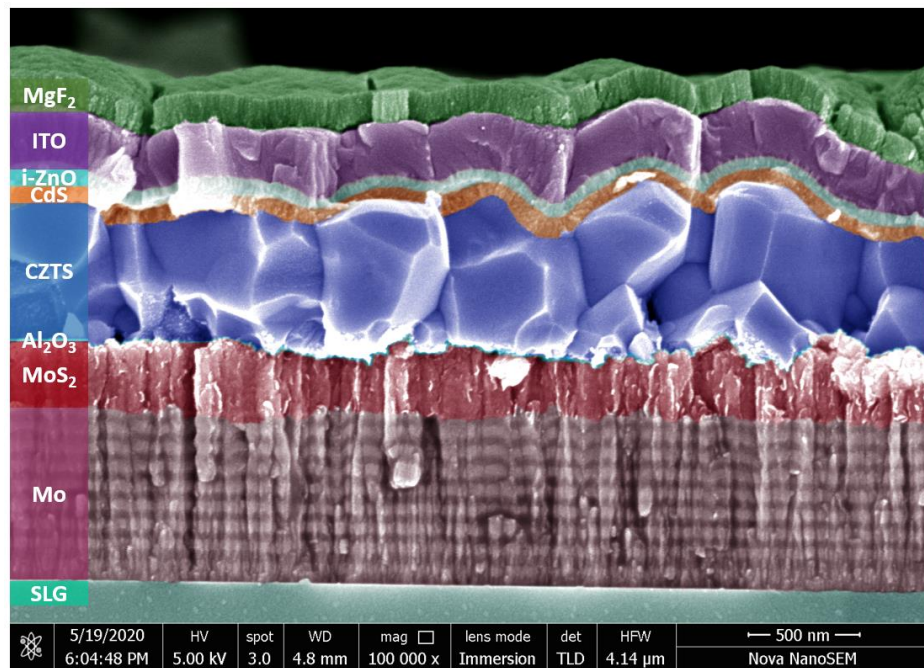


Figure 2.12 Coloured cross-sectional SEM image displaying a typical structure of CZTS device fabricated at University of New South Wales

2.5 Reference

- 1 Shin, D., Saparov, B. & Mitzi, D. B. Defect engineering in multinary earth-abundant chalcogenide photovoltaic materials. *Advanced Energy Materials* **7**, 1602366 (2017).
- 2 Goodman, C. The prediction of semiconducting properties in inorganic compounds. *Journal of Physics and Chemistry of Solids* **6**, 305-314 (1958).
- 3 Pamplin, B. A systematic method of deriving new semiconducting compounds by structural analogy. *Journal of Physics and Chemistry of Solids* **25**, 675-684 (1964).
- 4 Walsh, A., Chen, S., Wei, S. H. & Gong, X. G. Kesterite Thin-Film Solar Cells: Advances in Materials Modelling of Cu₂ZnSnS₄. *Advanced Energy Materials* **2**, 400-409 (2012).
- 5 Chen, S., Gong, X., Walsh, A. & Wei, S.-H. J. A. P. L. Crystal and electronic band structure of Cu₂ZnSnX₄ (X= S and Se) photovoltaic absorbers: First-principles insights. *Applied Physics Letters* **94**, 041903 (2009).
- 6 Valakh, M. Y. *et al.* Raman scattering and disorder effect in Cu₂ZnSnS₄. *physica status solidi (RRL)–Rapid Research Letters* **7**, 258-261 (2013).
- 7 Shin, S. W. *et al.* Studies on Cu₂ZnSnS₄ (CZTS) absorber layer using different stacking orders in precursor thin films. *Solar Energy Materials and Solar Cells* **95**, 3202-3206 (2011).
- 8 Tanaka, T., Kawasaki, D., Nishio, M., Guo, Q. & Ogawa, H. J. p. s. s. C. Fabrication of Cu₂ZnSnS₄ thin films by co-evaporation. *physica status solidi C* **3**, 2844-2847 (2006).
- 9 Pawar, S. *et al.* Effect of laser incident energy on the structural, morphological and optical properties of Cu₂ZnSnS₄ (CZTS) thin films. *Current Applied Physics* **10**, 565-569 (2010).

- 10 Cao, M. & Shen, Y. J. J. o. C. G. A mild solvothermal route to kesterite quaternary Cu₂ZnSnS₄ nanoparticles. *Journal of Crystal Growth* **318**, 1117-1120 (2011).
- 11 Zhou, H. *et al.* CZTS nanocrystals: a promising approach for next generation thin film photovoltaics. *Energy & Environmental Science* **6**, 2822-2838 (2013).
- 12 Persson, C. Electronic and optical properties of Cu₂ZnSnS₄ and Cu₂ZnSnSe₄. *Journal of Applied Physics* **107**, 053710 (2010).
- 13 Ito, K. Copper zinc tin sulfide-based thin-film solar cells. *John Wiley & Sons* (2014).
- 14 Blaha, P. *et al.* An Augmented Plane Wave+ Local Orbitals Program for Calculating Crystal Properties, Techn. (2001).
- 15 Gao, F., Yamazoe, S., Maeda, T., Nakanishi, K. & Wada, T. J. J. J. o. A. P. Structural and optical properties of in-free Cu₂ZnSn (S, Se)₄ solar cell materials. *Japanese Journal of Applied Physics* **51**, 10NC29 (2012).
- 16 Haight, R. *et al.* Band alignment at the Cu₂ZnSn (S_xSe_{1-x})₄/CdS interface. *Applied Physics Letters* **98**, 253502 (2011).
- 17 He, J. *et al.* Composition dependence of structure and optical properties of Cu₂ZnSn (S, Se)₄ solid solutions: an experimental study. *Journal of Alloys and Compounds* **511**, 129-132 (2012).
- 18 Persson, C. J. A. P. L. Anisotropic hole-mass tensor of CuIn_{1-x}Ga_x(S, Se)₂: Presence of free carriers narrows the energy gap. *Applied Physics Letters* **93**, 072106 (2008).
- 19 Kim, S., Kim, K. M., Tampo, H., Shibata, H. & Niki, S. Improvement of voltage deficit of Ge-incorporated kesterite solar cell with 12.3% conversion efficiency. *Applied Physics Express* **9**, 102301 (2016).
- 20 Kim, S. *et al.* Ge-incorporated Cu₂ZnSnSe₄ thin-film solar cells with efficiency greater than 10%. *Solar Energy Materials and Solar Cells* **144**, 488-492 (2016).

- 21 Ford, G. M., Guo, Q., Agrawal, R. & Hillhouse, H. W. J. C. o. M. Earth abundant element $\text{Cu}_2\text{Zn}(\text{Sn}_{1-x}\text{Ge}_x)\text{S}_4$ nanocrystals for tunable band gap solar cells: 6.8% efficient device fabrication. *Chemistry of Materials* **23**, 2626-2629 (2011).
- 22 Han, D. *et al.* Deep electron traps and origin of p-type conductivity in the earth-abundant solar-cell material $\text{Cu}_2\text{ZnSnS}_4$. *Physical Review B* **87**, 155206 (2013).
- 23 Chen, S., Walsh, A., Gong, X. G. & Wei, S. H. Classification of lattice defects in the kesterite $\text{Cu}_2\text{ZnSnS}_4$ and $\text{Cu}_2\text{ZnSnSe}_4$ earth-abundant solar cell absorbers. *Advanced Materials* **25**, 1522-1539 (2013).
- 24 Chen, S., Gong, X., Walsh, A. & Wei, S.-H. J. A. P. L. Defect physics of the kesterite thin-film solar cell absorber $\text{Cu}_2\text{ZnSnS}_4$. *Applied Physics Letters* **96**, 021902 (2010).
- 25 Chen, S., Yang, J.-H., Gong, X.-G., Walsh, A. & Wei, S.-H. Intrinsic point defects and complexes in the quaternary kesterite semiconductor $\text{Cu}_2\text{ZnSnS}_4$. *Physical Review B* **81**, 245204 (2010).
- 26 Li, J. *et al.* Tailoring the defects and carrier density for beyond 10% efficient CZTSe thin film solar cells. *Solar Energy Materials and Solar Cells* **159**, 447-455 (2017).
- 27 Huang, W.-C., Wei, S.-Y., Cai, C.-H., Ho, W.-H. & Lai, C.-H. The role of Ag in aqueous solution processed $(\text{Ag}, \text{Cu})_2\text{ZnSn}(\text{S}, \text{Se})_4$ kesterite solar cells: antisite defect elimination and importance of Na passivation. *Journal of Materials Chemistry A* **6**, 15170-15181 (2018).
- 28 Li, J. *et al.* Defect Control for 12.5% Efficiency $\text{Cu}_2\text{ZnSnSe}_4$ Kesterite Thin-Film Solar Cells by Engineering of Local Chemical Environment. *Advanced Materials* **32**, 2005268 (2020).

- 29 Gajdoš, M., Hummer, K., Kresse, G., Furthmüller, J. & Bechstedt, F. J. P. R. B. Linear optical properties in the projector-augmented wave methodology. *Physical Review B* **73**, 045112 (2006).
- 30 Mitzi, D. B., Gunawan, O., Todorov, T. K., Wang, K. & Guha, S. The path towards a high-performance solution-processed kesterite solar cell. *Solar Energy Materials and Solar Cells* **95**, 1421-1436 (2011).
- 31 Hsu, W.-C. *et al.* Reaction pathways for the formation of $\text{Cu}_2\text{ZnSn}(\text{Se}, \text{S})_4$ absorber materials from liquid-phase hydrazine-based precursor inks. *Energy & Environmental Science* **5**, 8564-8571 (2012).
- 32 Fairbrother, A. *et al.* On the formation mechanisms of Zn-rich $\text{Cu}_2\text{ZnSnS}_4$ films prepared by sulfurization of metallic stacks. *Solar Energy Materials and Solar Cells* **112**, 97-105 (2013).
- 33 Fella, C. M. *et al.* Formation mechanism of $\text{Cu}_2\text{ZnSnSe}_4$ absorber layers during selenization of solution deposited metal precursors. *Journal of Alloys and Compounds* **567**, 102-106 (2013).
- 34 Berg, D. M. *et al.* Simplified formation process for $\text{Cu}_2\text{ZnSnS}_4$ -based solar cells. *Thin Solid Films* **573**, 148-158 (2014).
- 35 Bodeux, R., Mollica, F., Delbos, S. J. S. E. M. & Cells, S. Growth of $\text{Cu}_2\text{ZnSnSe}_4$ by cosputtering and reactive annealing atmosphere. *Solar Energy Materials and Solar Cells* **132**, 67-73 (2015).
- 36 Jung, H. R. *et al.* Phase evolution of $\text{Cu}_2\text{ZnSnS}_4$ (CZTS) kesterite thin films during the sulfurization process. *Ceramics International* **41**, 13006-13011 (2015).
- 37 Hernández-Martínez, A. *et al.* Insights into the formation pathways of $\text{Cu}_2\text{ZnSnSe}_4$ using rapid thermal processes. *ACS Applied Energy Materials* **1**, 1981-1989 (2018).

- 38 Green, M. A. *et al.* Solar cell efficiency tables (version 56). *Progress in Photovoltaics: Research and Applications* **28**, 629-638 (2020).
- 39 Siebentritt, S. J. T. s. f. Why are kesterite solar cells not 20% efficient? *Thin Solid Films* **535**, 1-4 (2013).
- 40 Yan, C. *et al.* Cu₂ZnSnS₄ solar cells with over 10% power conversion efficiency enabled by heterojunction heat treatment. *Nature Energy* **3**, 764-772 (2018).
- 41 Pu, A. *et al.* Sentaurus modelling of 6.9% Cu₂ZnSnS₄ device based on comprehensive electrical & optical characterization. *Solar Energy Materials and Solar Cells* **160**, 372-381 (2017).
- 42 Gokmen, T., Gunawan, O., Todorov, T. K. & Mitzi, D. B. Band tailing and efficiency limitation in kesterite solar cells. *Applied Physics Letters* **103**, 103506 (2013).
- 43 Kim, S., Park, J.-S. & Walsh, A. Identification of killer defects in kesterite thin-film solar cells. *ACS Energy Letters* **3**, 496-500 (2018).
- 44 Scragg, J. J. *et al.* Effects of back contact instability on Cu₂ZnSnS₄ devices and processes. *Chemistry of Materials* **25**, 3162-3171 (2013).
- 45 Bär, M. *et al.* Cliff-like conduction band offset and KCN-induced recombination barrier enhancement at the CdS/Cu₂ZnSnS₄ thin-film solar cell heterojunction. *Applied Physics Letters* **99**, 222105 (2011).
- 46 Scragg, J. J., Ericson, T., Kubart, T., Edoff, M. & Platzer-Bjorkman, C. Chemical insights into the instability of Cu₂ZnSnS₄ films during annealing. *Chemistry of Materials* **23**, 4625-4633 (2011).
- 47 Werner, J. H., Mattheis, J. & Rau, U. Efficiency limitations of polycrystalline thin film solar cells: case of Cu (In, Ga) Se₂. *Thin Solid Films* **480**, 399-409 (2005).
- 48 Rey, G. *et al.* On the origin of band-tails in kesterite. *Solar Energy Materials and Solar Cells* **179**, 142-151 (2018).

- 49 Wallace, S. K., Mitzi, D. B. & Walsh, A. The steady rise of kesterite solar cells. *ACS Energy Letters* **2**, 776-779 (2017).
- 50 Gershon, T. *et al.* Photovoltaic device with over 5% efficiency based on an n-type $\text{Ag}_2\text{ZnSnSe}_4$ absorber. *Advanced Energy Materials* **6**, 1601182 (2016).
- 51 Yan, C. *et al.* Beyond 11% Efficient Sulfide Kesterite $\text{Cu}_2\text{Zn}_x\text{Cd}_{1-x}\text{SnS}_4$ Solar Cell: Effects of Cadmium Alloying. *ACS Energy Letters* **2**, 930-936 (2017).
- 52 Chen, Z. *et al.* Solution-processed trigonal $\text{Cu}_2\text{BaSnS}_4$ thin-film solar cells. *ACS Applied Energy Materials* **1**, 3420-3427 (2018).
- 53 Nagaya, K. *et al.* Very small tail state formation in $\text{Cu}_2\text{ZnGeSe}_4$. *Applied Physics Letters* **113**, 093901 (2018).
- 54 Sahayaraj, S. *et al.* Optoelectronic properties of thin film $\text{Cu}_2\text{ZnGeSe}_4$ solar cells. *Solar Energy Materials and Solar Cells* **171**, 136-141 (2017).
- 55 Todorov, T. K. *et al.* Beyond 11% efficiency: characteristics of state-of-the-art $\text{Cu}_2\text{ZnSn}(\text{S}, \text{Se})_4$ solar cells. *Advanced Energy Materials* **3**, 34-38 (2013).
- 56 Hoex, B., Gielis, J., Van de Sanden, M. & Kessels, W. J. J. o. A. P. On the c-Si surface passivation mechanism by the negative-charge-dielectric Al_2O_3 . *Journal of Applied Physics* **104**, 113703 (2008).
- 57 Cui, X. *et al.* Cd-Free $\text{Cu}_2\text{ZnSnS}_4$ solar cell with an efficiency greater than 10% enabled by Al_2O_3 passivation layers. *Energy & Environmental Science* **12**, 2751-2764 (2019).
- 58 Kaur, K., Kumar, N. & Kumar, M. Strategic review of interface carrier recombination in earth abundant Cu–Zn–Sn–S–Se solar cells: current challenges and future prospects. *Journal of Materials Chemistry A* **5**, 3069-3090 (2017).
- 59 Yan, C. *et al.* Band alignments of different buffer layers (CdS , $\text{Zn}(\text{O}, \text{S})$, and In_2S_3) on $\text{Cu}_2\text{ZnSnS}_4$. *Applied Physics Letters* **104**, 173901 (2014).

- 60 Minemoto, T. *et al.* Theoretical analysis of the effect of conduction band offset of window/CIS layers on performance of CIS solar cells using device simulation. *Solar Energy Materials and Solar Cells* **67**, 83-88 (2001).
- 61 Sun, K. *et al.* Over 9% efficient kesterite Cu₂ZnSnS₄ solar cell fabricated by using Zn_{1-x}Cd_xS buffer layer. *Advanced Energy Materials* **6**, 1600046 (2016).
- 62 Li, X. *et al.* 8.6% Efficiency CZTSSe solar cell with atomic layer deposited Zn-Sn-O buffer layer. *solar Energy Materials and Solar Cells* **157**, 101-107 (2016).
- 63 Tajima, S., Umehara, M. & Mise, T. Photovoltaic properties of Cu₂ZnSnS₄ cells fabricated using ZnSnO and ZnSnO/CdS buffer layers. *Japanese Journal of Applied Physics* **55**, 112302 (2016).
- 64 Cui, X. *et al.* Enhanced Heterojunction Interface Quality To Achieve 9.3% Efficient Cd-Free Cu₂ZnSnS₄ Solar Cells Using Atomic Layer Deposition ZnSnO Buffer Layer. *Chemistry of Materials* **30**, 7860-7871 (2018).
- 65 Yuan, Z. K. *et al.* Engineering solar cell absorbers by exploring the band alignment and defect disparity: the case of Cu-and Ag-based kesterite compounds. *Advanced Functional Materials* **25**, 6733-6743 (2015).
- 66 Wang, D. *et al.* Formation of the front-gradient bandgap in the Ag doped CZTSe thin films and solar cells. *Journal of Energy Chemistry* (2019).
- 67 Qi, Y. *et al.* Elemental Precursor Solution Processed (Cu_{1-x} Ag_x)₂ZnSn (S, Se)₄ Photovoltaic Devices with over 10% Efficiency. *ACS applied materials & interfaces* **9**, 21243-21250 (2017).
- 68 Grovenor, C. Grain boundaries in semiconductors. *Journal of Physics C: Solid State Physics* **18**, 4079 (1985).
- 69 Mönch, W. Semiconductor surfaces and interfaces. *Springer Science & Business Media* **26** (2013).

- 70 Metzger, W. & Gloeckler, M. J. J. o. A. P. The impact of charged grain boundaries on thin-film solar cells and characterization. *Journal of Applied Physics* **98**, 063701 (2005).
- 71 Taretto, K. & Rau, U. Numerical simulation of carrier collection and recombination at grain boundaries in Cu (In, Ga) Se₂ solar cells. *Journal of applied physics* **103**, 094523 (2008).
- 72 Raghuwanshi, M. *et al.* Evidence of enhanced carrier collection in Cu (In, Ga) Se₂ grain boundaries: correlation with microstructure. *ACS Applied Materials & Interfaces* **10**, 14759-14766 (2018).
- 73 Jiang, C.-S. *et al.* Local built-in potential on grain boundary of Cu (In, Ga) Se₂ thin films. *Applied physics letters* **84**, 3477-3479 (2004).
- 74 Jiang, C.-S. *et al.* Does the local built-in potential on grain boundaries of Cu (In, Ga) Se₂ thin films benefit photovoltaic performance of the device? *Applied physics letters* **85**, 2625-2627 (2004).
- 75 Jiang, C. S. *et al.* in *2017 IEEE 44th Photovoltaic Specialist Conference (PVSC)*. 1312-1316 (IEEE).
- 76 Li, C. *et al.* Grain-boundary-enhanced carrier collection in CdTe solar cells. *Physical review letters* **112**, 156103 (2014).
- 77 Stokes, A., Al-Jassim, M., Diercks, D., Clarke, A. & Gorman, B. Impact of Wide-Ranging Nanoscale Chemistry on Band Structure at Cu (In, Ga) Se₂ Grain Boundaries. *Scientific reports* **7**, 14163 (2017).
- 78 Ma, Y. *et al.* Band bending near grain boundaries of Cu₂ZnSn(S, Se)₄ thin films and its effect on photovoltaic performance. *Nano Energy* **51**, 37-44 (2018).

- 79 Li, J. B., Chawla, V. & Clemens, B. M. J. A. M. Investigating the role of grain boundaries in CZTS and CZTSSe thin film solar cells with scanning probe microscopy. *Advanced Materials* **24**, 720-723 (2012).
- 80 Kim, G. Y. *et al.* Surface potential on grain boundaries and intragains of highly efficient Cu₂ZnSn (S, Se) 4 thin-films grown by two-step sputtering process. *Solar Energy Materials and Solar Cells* **127**, 129-135 (2014).
- 81 Kim, G. Y. *et al.* Nanoscale observation of surface potential and carrier transport in Cu₂ZnSn (S, Se) 4 thin films grown by sputtering-based two-step process. *Nanoscale Research Letters* **9**, 10 (2014).
- 82 Xin, H. *et al.* Lithium-doping inverts the nanoscale electric field at the grain boundaries in Cu₂ZnSn (S, Se) 4 and increases photovoltaic efficiency. *Physical Chemistry Chemical Physics* **17**, 23859-23866 (2015).
- 83 Park, J. *et al.* The Role of Hydrogen from ALD-Al₂O₃ in Kesterite Cu₂ZnSnS₄ Solar Cells: Grain Surface Passivation. *Advanced Energy Materials* **8**, 1701940 (2018).
- 84 Jeong, W. L. *et al.* Impact of Na Doping on the Carrier Transport Path in Polycrystalline Flexible Cu₂ZnSn (S, Se) 4 Solar Cells. *Advanced Science* **7**, 1903085 (2020).
- 85 Raghuwanshi, M., Wuerz, R. & Cojocaru-Mirédin, O. Interconnection between Trait, Structure, and Composition of Grain Boundaries in Cu (In, Ga) Se₂ Thin-Film Solar Cells. *Advanced Functional Materials* **30**, 2001046 (2020).
- 86 Nicoara, N. *et al.* Direct evidence for grain boundary passivation in Cu (In, Ga) Se₂ solar cells through alkali-fluoride post-deposition treatments. *Nature Communications* **10**, 1-8 (2019).
- 87 Schwarz, T. *et al.* Atom probe tomography study of internal interfaces in Cu₂ZnSnSe₄ thin-films. *Journal of Applied Physics* **118**, 095302 (2015).

- 88 Tajima, S. *et al.* Sodium distribution in solar-grade Cu₂ZnSnS₄ layers using atom-probe tomographic technique. *Japanese Journal of Applied Physics* **54**, 112302 (2015).
- 89 Baier, R., Leendertz, C., Abou-Ras, D., Lux-Steiner, M. C. & Sadewasser, S. Properties of electronic potential barriers at grain boundaries in Cu (In, Ga) Se₂ thin films. *Solar Energy Materials and Solar Cells* **130**, 124-131 (2014).
- 90 Redinger, A., Berg, D. M., Dale, P. J. & Siebentritt, S. The consequences of kesterite equilibria for efficient solar cells. *Journal of the American Chemical Society* **133**, 3320-3323 (2011).
- 91 Scragg, J. J. *et al.* A detrimental reaction at the molybdenum back contact in Cu₂ZnSn (S, Se) ₄ thin-film solar cells. *Journal of the American Chemical Society* **134**, 19330-19333 (2012).
- 92 Todorov, T. K., Reuter, K. B. & Mitzi, D. B. J. A. m. High-efficiency solar cell with earth-abundant liquid-processed absorber. *Advanced Energy Materials* **22**, E156-E159 (2010).
- 93 Katagiri, H. *et al.* Development of CZTS-based thin film solar cells. *Thin Solid Films* **517**, 2455-2460 (2009).
- 94 Tanaka, K., Fukui, Y., Moritake, N., Uchiki, H. J. S. E. M. & Cells, S. Chemical composition dependence of morphological and optical properties of Cu₂ZnSnS₄ thin films deposited by sol–gel sulfurization and Cu₂ZnSnS₄ thin film solar cell efficiency. *Solar Energy Materials and Solar Cells* **95**, 838-842 (2011).
- 95 Liu, F. *et al.* Beyond 8% ultrathin kesterite Cu₂ZnSnS₄ solar cells by interface reaction route controlling and self-organized nanopattern at the back contact. *NPG Asia Materials* **9**, e401 (2017).

- 96 Shin, B., Zhu, Y., Bojarczuk, N. A., Jay Chey, S. & Guha, S. Control of an interfacial MoSe₂ layer in Cu₂ZnSnSe₄ thin film solar cells: 8.9% power conversion efficiency with a TiN diffusion barrier. *Applied Physics Letters* **101**, 053903 (2012).
- 97 Scragg, J. J. *et al.* Effects of back contact instability on Cu₂ZnSnS₄ devices and processes. *Chemistry of Materials* **25**, 3162-3171 (2013).
- 98 Cui, H. *et al.* Boosting Cu₂ZnSnS₄ solar cells efficiency by a thin Ag intermediate layer between absorber and back contact. *Applied Physics Letters* **104**, 041115 (2014).
- 99 Lee, Y. S. *et al.* Atomic Layer Deposited Aluminum Oxide for Interface Passivation of Cu₂ZnSn (S, Se) 4 Thin-Film Solar Cells. *Advanced Energy Materials* **6**, 1600198 (2016).
- 100 Xue, C. *et al.* Revealing Nanoscale Domains in Cu₂ZnSnS₄ Thin Films by Catalyzed Chemical Etching. *physica status solidi–Rapid Research Letters* **14**, 2000283 (2020).
- 101 Vidal, J. *et al.* Band-structure, optical properties, and defect physics of the photovoltaic semiconductor SnS. *Applied Physics Letters* **100**, 032104 (2012).
- 102 Sinsermsuksakul, P., Heo, J., Noh, W., Hock, A. S. & Gordon, R. G. Atomic layer deposition of tin monosulfide thin films. *Advanced Energy Materials* **1**, 1116-1125 (2011).
- 103 Berg, D. M. *et al.* Thin film solar cells based on the ternary compound Cu₂SnS₃. *Thin Solid Films* **520**, 6291-6294 (2012).
- 104 Liu, G., Schulmeyer, T., Brötz, J., Klein, A. & Jaegermann, W. Interface properties and band alignment of Cu₂S/CdS thin film solar cells. *Thin Solid Films* **431**, 477-482 (2003).
- 105 Cardona, M. & Peter, Y. Y. Fundamentals of semiconductors. *Springer* (2005).

- 106 Shin, B., Bojarczuk, N. A. & Guha, S. On the kinetics of MoSe₂ interfacial layer formation in chalcogen-based thin film solar cells with a molybdenum back contact. *Applied Physics Letters* **102**, 091907 (2013).
- 107 Liu, F. *et al.* In situ growth of Cu₂ZnSnS₄ thin films by reactive magnetron co-sputtering. *Solar Energy Materials and Solar Cells* **94**, 2431-2434 (2010).
- 108 Fernandes, P., Salomé, P., Da Cunha, A. & Schubert, B.-A. Cu₂ZnSnS₄ solar cells prepared with sulphurized dc-sputtered stacked metallic precursors. *Thin Solid Films* **519**, 7382-7385 (2011).
- 109 Ericson, T., Kubart, T., Scragg, J. J. & Platzer-Björkman, C. Reactive sputtering of precursors for Cu₂ZnSnS₄ thin film solar cells. *Thin Solid Films* **520**, 7093-7099 (2012).
- 110 Garcia-Llamas, E. *et al.* Cu₂ZnSnS₄ thin film solar cells grown by fast thermal evaporation and thermal treatment. *Solar Energy* **141**, 236-241 (2017).
- 111 Schubert, B. A. *et al.* Cu₂ZnSnS₄ thin film solar cells by fast coevaporation. *Progress in Photovoltaics: Research and Applications* **19**, 93-96 (2011).
- 112 Shi, C., Shi, G., Chen, Z., Yang, P. & Yao, M. Deposition of Cu₂ZnSnS₄ thin films by vacuum thermal evaporation from single quaternary compound source. *Materials Letters* **73**, 89-91 (2012).
- 113 Vanalakar, S. *et al.* A review on pulsed laser deposited CZTS thin films for solar cell applications. *Journal of Alloys and Compounds* **619**, 109-121 (2015).
- 114 Wang, W. *et al.* Device characteristics of CZTSSe thin-film solar cells with 12.6% efficiency. *Advanced Energy Materials* **4**, 1301465 (2014).
- 115 Mitzi, D. B. Solution processing of chalcogenide semiconductors via dimensional reduction. *Advanced Materials* **21**, 3141-3158 (2009).

- 116 Su, Z. *et al.* Fabrication of Cu₂ZnSnS₄ solar cells with 5.1% efficiency via thermal decomposition and reaction using a non-toxic sol–gel route. *Journal of Materials Chemistry A* **2**, 500-509 (2014).
- 117 Liu, F. *et al.* Kesterite Cu₂ZnSn (S, Se) solar cells with beyond 8% efficiency by a sol–gel and selenization process. *ACS applied materials & interfaces* **7**, 14376-14383 (2015).
- 118 Haass, S. G. *et al.* 11.2% efficient solution processed kesterite solar cell with a low voltage deficit. *Advanced Energy Materials* **5**, 1500712 (2015).
- 119 Su, Z. *et al.* Cation substitution of solution-processed Cu₂ZnSnS₄ thin film solar cell with over 9% efficiency. *Advanced Energy Materials* **5**, 1500682 (2015).
- 120 Nakayama, N. & Ito, K. Sprayed films of stannite Cu₂ZnSnS₄. *Applied Surface Science* **92**, 171-175 (1996).
- 121 Lin, X., Kavalakkatt, J., Lux-Steiner, M. C. & Ennaoui, A. Inkjet-Printed Cu₂ZnSn (S, Se) solar cells. *Advanced science* **2**, 1500028 (2015).
- 122 Su, Z. *et al.* Preparation of Cu₂ZnSnS₄ thin films by sulfurizing stacked precursor thin films via successive ionic layer adsorption and reaction method. *Applied Surface Science* **258**, 7678-7682 (2012).
- 123 Sun, K. *et al.* Flexible Cu₂ZnSnS₄ solar cells based on successive ionic layer adsorption and reaction method. *RSC Advances* **4**, 17703-17708 (2014).
- 124 Son, D.-H. *et al.* Effect of solid-H₂S gas reactions on CZTSSe thin film growth and photovoltaic properties of a 12.62% efficiency device. *Journal of Materials Chemistry A* (2019).
- 125 Katagiri, H. *et al.* Preparation and evaluation of Cu₂ZnSnS₄ thin films by sulfurization of E–B evaporated precursors. *Solar Energy Materials and Solar Cells* **49**, 407-414 (1997).

Chapter 3

Buffer/Absorber Heterointerface Passivation of High-Efficiency CZTS

Solar Cells Using an Ultrathin Intermediate Stannic Oxide Layer via a Solution Method¹

3.1 Introduction

As discussed in Chapter 2, the SRH recombination at the buffer/absorber heterointerface is regarded as one of the main V_{oc} deficit culprits in kesterite solar cells. One effective approach of alleviating the heterointerface recombination is introducing a wide-bandgap (WBG) dielectric layer between the buffer and the absorber layers. For kesterite solar cells, various WBG oxide materials have been applied as the intermediate layer. The insertion of CeO_2 , for instance, had been applied to CZTS solar cells and yielded higher V_{oc} due to the reduced lattice mismatch between the buffer and the absorber and assumed optimization of band alignment ¹. However, the loss in current strongly limits the improvement of efficiency. Alumina (Al_2O_3), as a popular passivation material, has not only been applied to passivate Si surfaces in the manner of chemical and field-effect passivation ², but also used as the front heterointerface passivation layer in CIGSe ³, CZTSe ⁴ and CZTS ⁵ solar cells. Kim et al. deposited Al_2O_3 via atomic layer deposition (ALD) on top of the CZTSe film and shows significant improvement in device performance, resulting in a peak efficiency of 11.5 % ⁴. However, no Al signals at the CdS/CZTS heterojunction from SIMS measurement have been

¹ This Chapter is partially based on:

H. Sun, K. Sun, J. Huang, C. Yan, F. Liu, J. Park, A. Pu, J. A. Stride, M. A. Green, and X. Hao, *Efficiency enhancement of kesterite Cu_2ZnSnS_4 solar cells via solution-processed ultrathin tin oxide intermediate layer at absorber/buffer interface*, ACS Applied Energy Materials, 2017, 1, 154-160.

H. Sun, J. Huang, J. S. Yun, K. Sun, C. Yan, F. Liu, J. Park, A. Pu, J. Seidel, J. A. Stride, M. Green and X. Hao, *Solution-processed ultrathin SnO_2 passivation of absorber/buffer heterointerface and grain boundaries for high efficiency kesterite Cu_2ZnSnS_4 solar cells*, 2019 IEEE 46th Photovoltaic Specialists Conference (PVSC). IEEE, 2019, 2503-2506.

detected in the finished devices, which could be explained as the etching of Al_2O_3 by aqueous ammonia during the CdS-CBD process. We also observed that no ALD-deposited Al_2O_3 left after CdS deposition and, instead, the increase of H concentration at the CZTS/CdS heterointerface has been observed ⁶. The presence of H is believed to originate from the exposure of the hydrogen source like trimethylaluminum (TMA, $\text{Al}(\text{CH}_3)_3$) and H_2O during the ALD process ⁶. Later, the ALD- Al_2O_3 has been reported that it can be applied to the Cd-free CZTS devices with ZnSnO buffer from our work ⁵. The latter yielded the champion efficiency of 10.2 % for Cd-free pure-sulfide kesterite solar cells. The kesterite widely used and crowned as record efficiency still use CdS buffer. Therefore, the development of an aqueous ammonia-resisted dielectric intermediate layer is important for providing an intermediate passivation layer for the heterointerface defective CdS/CZTS solar cells.

Stannic oxide (SnO_2), as another type of WBG dielectric material, has been found that can effectively passivate the CdS/CZTSSe heterointerface and the CZTSSe GBs ⁷. The ALD- SnO_2 was employed in SnS solar cells for giving a marked effect in interface passivation ⁸. Furthermore, SnO_x , was in-situ grown through annealing CZTSSe film at 375 °C in the air at the Sn-rich grain surface (including GBs). However, SnO_x at the grain surface was easily removed during the CBD process. However, regarding our pure-sulfide CZTS film ^{9,10}, the noticeable Sn-enriched grain surface and boundaries were not yet observed. Therefore, the SnO_2 formation through air annealing in our samples is difficult, and an alternative way for the intentional deposition of the NH_4OH -resistant SnO_2 layer is required.

In this chapter, we successfully introduced an ultrathin dielectric SnO_2 intermediate layer at the CZTS/CdS heterointerface to facilitate the local passivation, resulting in the enhanced

minority carrier lifetime. By optimizing the thickness of this intermediate layer, 8.47 % peak efficiency is achieved. Furthermore, parasitic absorption of CdS was found reduced due to thinner CdS grown on the SnO₂-coated CZTS with a slower growth rate. The effect of the CdS thickness is investigated with the presence of this new passivation layer at the heterointerface. It is also revealed that employing this ultrathin layer at the CZTS/CdS heterointerface not only provides a chemical passivation route, but also optimizes the band alignment.

3.2 Experimental

From the literature ^{11,12}, SnO₂ had been synthesized through successive ionic layer adsorption and reaction (SILAR) method. One of the reports ¹² used aqueous ammonia as a complex agent which has a similar concentration to that for the CdS-CBD process. In this way, a weak-base resistant intermediate oxide layer can be obtained. The SILAR method is ideal for fabricating ultrathin films with excellent thickness control through the number of SILAR cycles.

In this work, the precursor solution for the SnO₂ nanolayer was prepared by dissolving SnCl₄·5H₂O (1.25 mM, AR) in deionized (DI) water. Aqueous ammonia (3 M, AR) was added into the SnCl₄ solution with constant stirring. The ionized Sn⁴⁺ cations associated with ammonia to form aqueous tin-ammonia complex ions ([Sn(NH₃)₄]⁴⁺) and to prevent the fast precipitation of Sn(OH)₄ in the solution. The sulfurized CZTS samples were dipped in the precursor solution to absorb [Sn(NH₃)₄]⁴⁺ complex ions at the CZTS surface at room temperature for 20 s. After air drying, the [Sn(NH₃)₄]⁴⁺-attached samples were immersed in 90 °C-hot DI water for 5 s to possibly form Sn(OH)₄ or other relevant chemicals at the CZTS

surface. One SILAR cycle finished by ultrasonicing the air-dried $\text{Sn}(\text{OH})_4$ -grown samples for 20 s to remove the agglomerates of $\text{Sn}(\text{OH})_4$. Several SILAR cycles were repeated to achieve the desired thickness. After the deposition, $\text{Sn}(\text{OH})_4$ -coated samples were undergone a 270 °C annealing in the air for 3 min to decompose $\text{Sn}(\text{OH})_4$ into SnO_2 . The total thickness of SnO_2 , prepared from hundreds of SILAR cycles, was measured through a profiler (Veeco Dektak 8 Advanced Development Profiler), which determines the growth rate per SILAR cycle is approx. 0.4 nm only, while the growth rate could be underestimated. Instead, in this Chapter, the number of the film thickness will be expressed as the number of cycles. The details of fabrication methods for other layers presented in Chapter 2 (Section 2.4). The device structure for the CZTS devices with SnO_2 passivation layer is depicted in Figure 3.1.

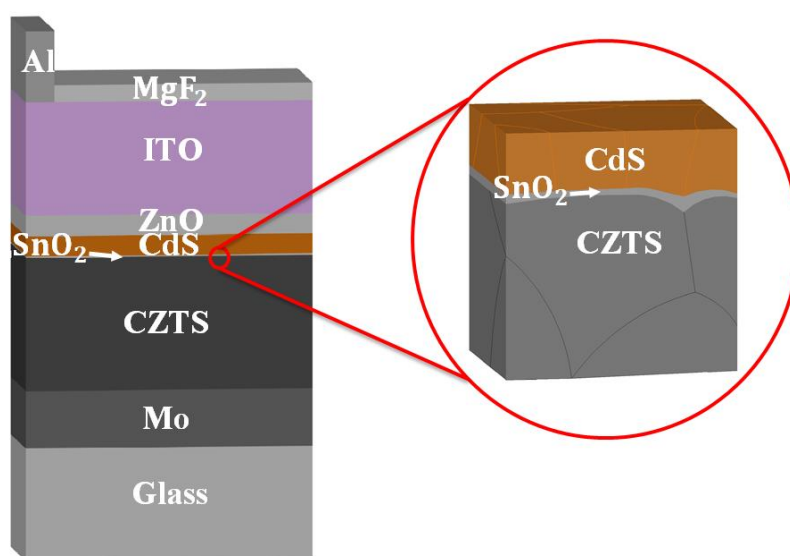


Figure 3.1 Schema of device structures with details of $\text{CdS}/\text{SnO}_2/\text{CZTS}$ heterojunctions (not to scale). This figure has been published as our work in ¹³. Reproduced with permission ¹³. © 2021 American Chemical Society.

For film characterizations, X-ray photoelectron spectroscopy (XPS) was employed to validate this SILAR method via an ESCALAB250Xi (Thermo Scientific, U.K.) under ultrahigh

vacuum ($< 2 \times 10^{-9}$ mbar). The band gap of the SnO_2 layer fabricated on the glass substrate was determined from optical transmittance measurement via UV-vis-near-IR spectrometer (PerkinElmer-Lambda 950). For device characterizations, time-resolved photoluminescence (TRPL) was carried out by applying the time-correlated single photon counting technique (MicroTime 200, PicoQuant) under laser excitation at 470 nm wavelength and 20 MHz pulse with tunable repetition. The current density – voltage (J - V) curves were tested using a simulator (Newport) under air mass (AM) 1.5 and one sun illumination, calibrated by a standard silicon reference cell. External quantum efficiency (EQE) measurement was conducted through a QEX10 spectral response system (PV Measurements, Inc.), using a monochromatic light chopping at 120 Hz. Capacitance-voltage (C - V) measurement was performed using an impedance analyzer at a frequency of 100 Hz and a DC bias voltage sweeping from -1.5 V to 0.5 V.

3.3 Results and Discussion

3.3.1 Method Verification and Validation

The XPS characterization has been conducted firstly to validate the method. Three samples were prepared for this measurement, including a SnO_2 layer with 10 SILAR cycles on the CZTS film, the CZTS film only and a SnO_2 layer with 100 SILAR cycles on quartz. Regarding the SnO_2 -coated CZTS sample, since the detection depth for XPS measurement can reach up to 10 nm, the signals of the underneath CZTS sample were also detected. As Figure 3.2a shows, two distinctive binding energy peaks (in red and green) for $\text{Sn } 3d^5$ can be seen at 486.2 and 487.4 eV, through fitting the measured XPS spectra (in blue), which has been confirmed by the binding energies of $\text{Sn } 3d^5$ in the pure CZTS samples (Figure 3.2b) and pure SnO_x samples (Figure 3.2c), respectively. The results match the previously reported

binding energies of Sn-S and Sn-O, respectively ¹⁴⁻¹⁶. The presence of Sn-O bonds conclusively demonstrates the formation of SnO_x at the CZTS surface. The Tauc's plot, shown in Figure 3.3 and derived from the transmittance measurement, determines the band gap of this SnO_x-layer (prepared from 200 SILAR cycles followed by air annealing) at 3.7 eV, consistent with that of SnO₂. It should be also noticed that the E_g of SnO₂ varies with thickness by using this SILAR method ¹², which indicates the E_g of SnO₂ with the optimal thickness (~1-3 cycles) applied to the CZTS devices may be higher than 3.7 eV.

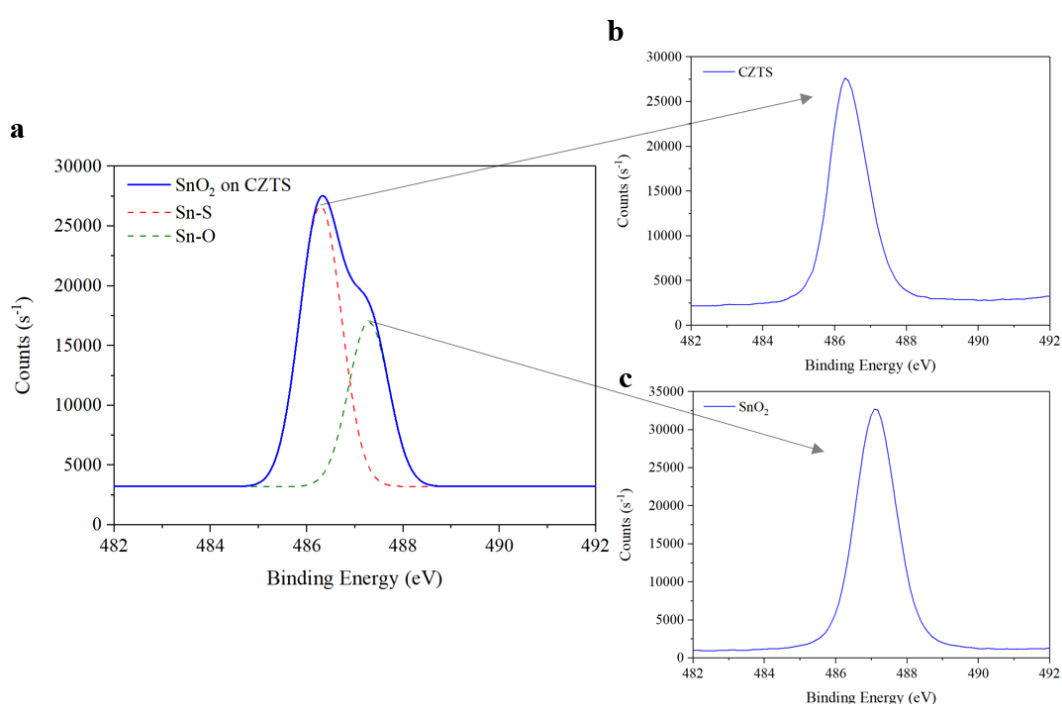


Figure 3.2 XPS Spectra of a. 10-SILAR cycle SnO₂ grown on CZTS absorber surface; b. As-grown CZTS after sulfurization; c. 100-SILAR cycle SnO₂ grown on quartz. This figure has been published as our previous work in ¹³. Reproduced with permission ¹³. © 2021 American Chemical Society, however, it has been modified for this work.

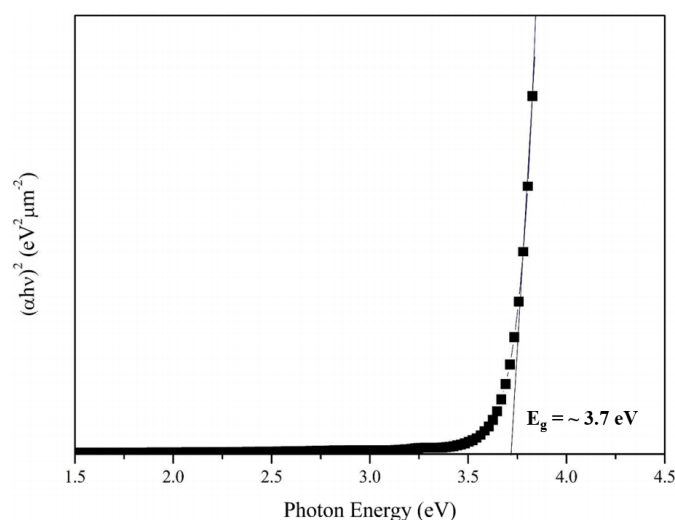


Figure 3.3 Tauc's Plot for determining the E_g of SnO_2 grown by SILAR method with 200 SILAR cycles. This figure has been published as our previous work in ¹³. Reproduced with permission ¹³. © 2021 American Chemical Society.

3.3.2 Effectiveness of CdS/CZTS Heterointerface Passivation

The passivation effect of this intermediate layer was supported by time-resolved photoluminescence (TRPL) measurement. Figure 3.4 illustrates the TRPL decay curves, where a 470 nm laser was used for the excitation of the CdS and the surface region of CZTS layer, and the PL only beyond 550 nm (feedback from the CZTS surface) was collected by the detector. The CZTS device with the SnO_2 layer shows much slower decay compared to that without this layer. Through fitting the decay curve using the biexponential function model fitting ¹⁷, minority carrier lifetime was obtained as 5.0 and 7.4 ns for the CZTS devices w/o and w/ the SnO_2 passivation layer, respectively.

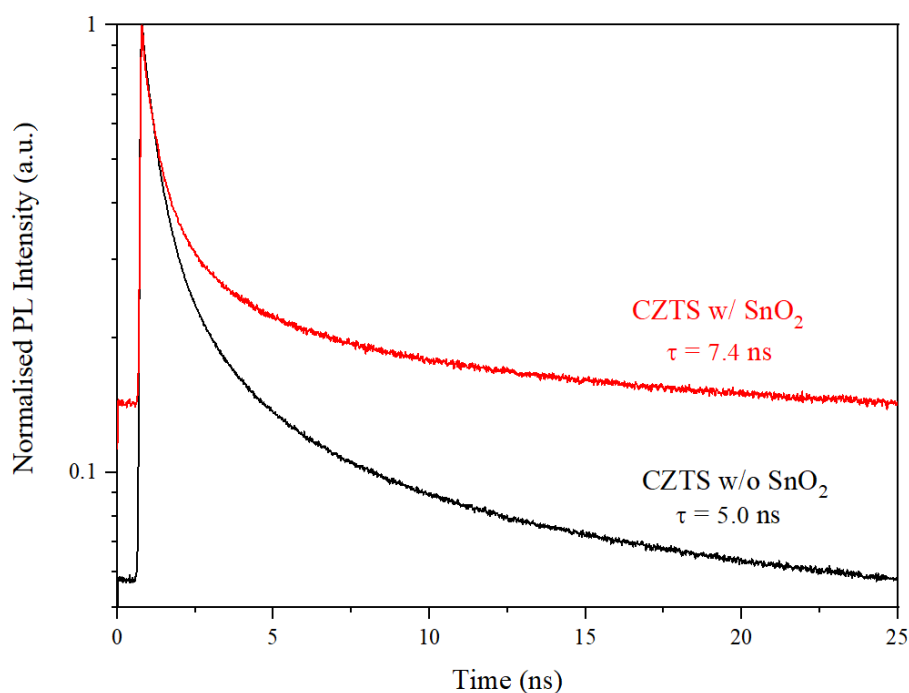


Figure 3.4 TRPL Transient of CZTS devices w/o and w/ SnO_2 passivation layer using 470 nm laser. This figure has been published as our previous work in ¹³. Reproduced with permission ¹³. © 2021 American Chemical Society, however, it has been modified for this work.

3.3.3 Improvement in Device Performance

The application of the SnO_2 intermediate layer between CZTS and CdS yields the improvement of PCE from 6.82 % to 8.47 %, particularly contributed to higher V_{OC} and FF, as shown in Figure 3.5a. Besides, the increase of shunt resistance (R_{SH}), as seen in Table 3.2, confirms this thin layer can be used as a shunt blocking layer, which contributed by quenching the undesired current drains across shunt pathways due to pinholes ¹⁸, local small grain size ¹⁹, high surface roughness, secondary phases, etc. Furthermore, J_{SC} remains stable due to a compromise between the enhanced short-wavelength response and the weakened red and infrared response, as presented in Figure 3.5b. The causes of such variations in optical response are discussed in Section 3.3.5 and 3.3.6.

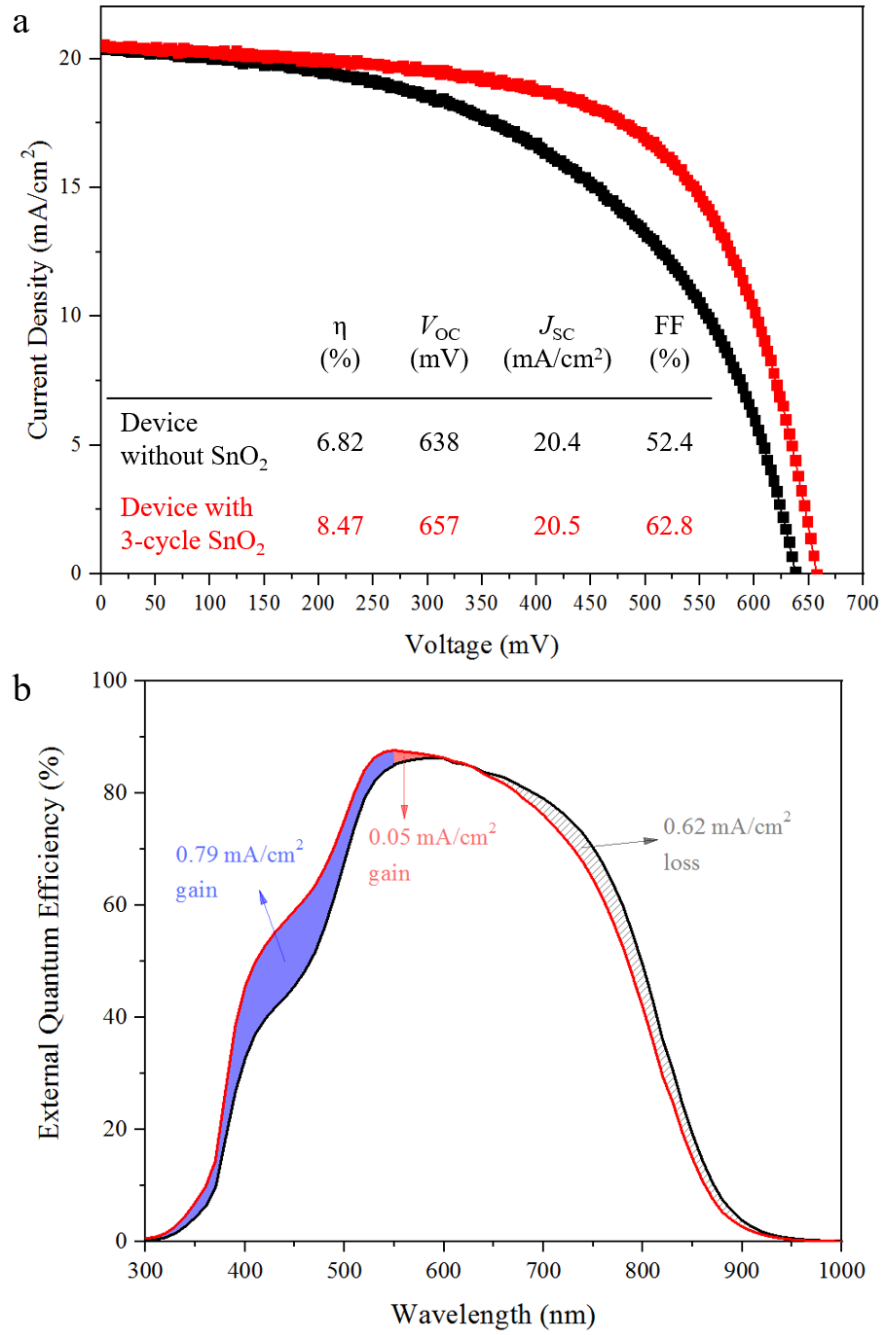


Figure 3.5 a. J - V curves of CZTS devices without and with SnO₂ layer, b. EQE spectra of the same devices in a. This figure has been published as our previous work in ²⁰. Reproduced with permission ²⁰. © Copyright 2021 IEEE.

3.3.4 Impacts of Device Performance from Different SnO₂ Thickness

The thickness and coverage of the SnO₂ layer are determined by SILAR cycles. The surface coverage cannot be guaranteed when this layer is too thin, and thus, the passivation effect could be limited. As demonstrated in Figure 3.6a and Table 3.1, V_{OC} and FF increase with SILAR cycles. However, as shown in Figure 3.7a, the excessive thickness of SnO₂ (8-cycle) results in a lower PCE, caused by the decrease in J_{sc} and FF from larger series resistance (R_s), although V_{OC} is further improved due to the enhanced passivation effect. The EQE result in Figure 3.7b shows the weakened optical response throughout the entire CdS and CZTS layers, particularly at the heterojunction region. This could be driven by the increased R_s of the resistive SnO₂ layer with a larger thickness.

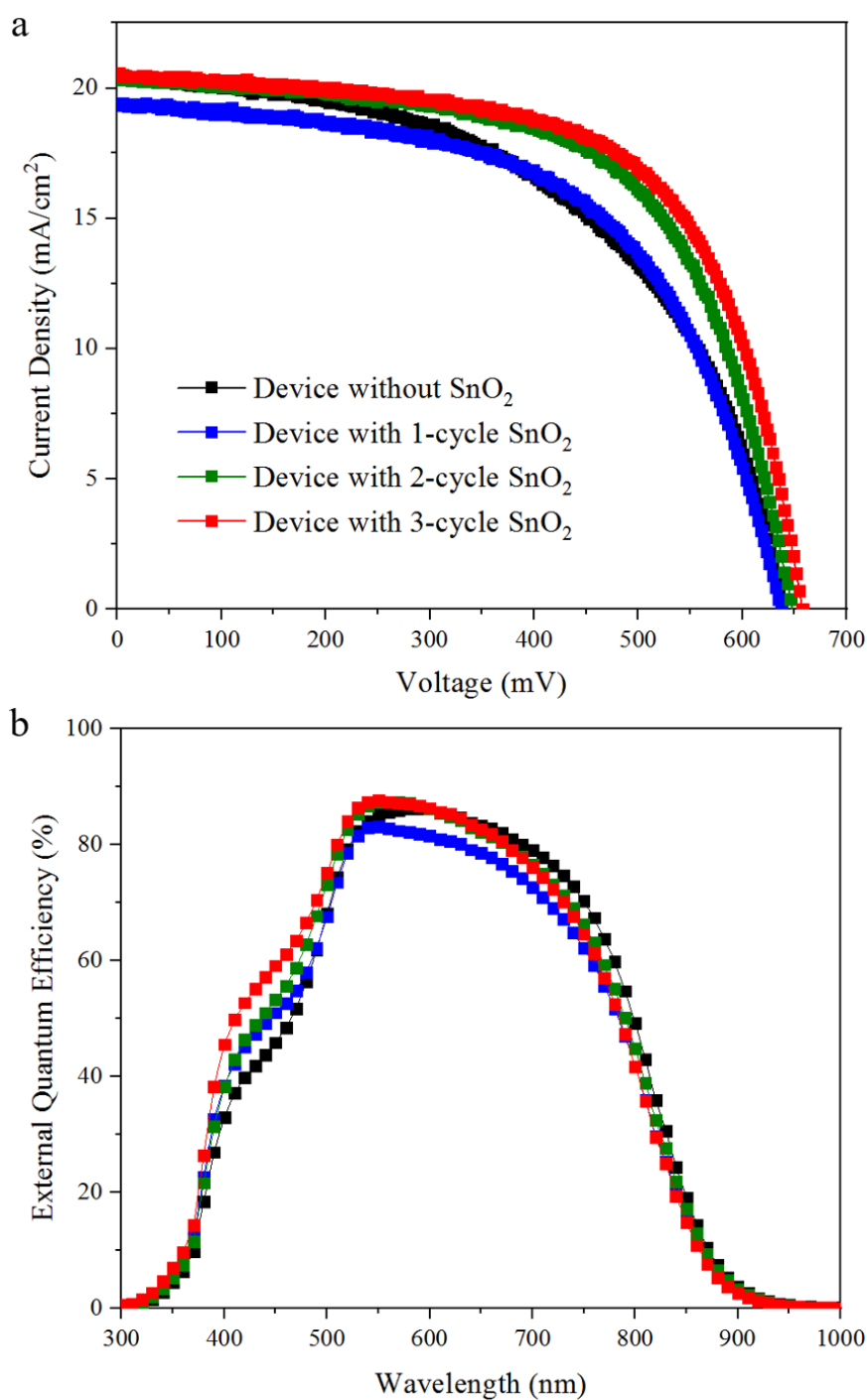


Figure 3.6 CZTS devices without and with SnO₂ in different thickness (determined by number of cycles) a. *J-V* curves, b. EQE spectra. This figure has been published as our previous work in ¹³. Reproduced with permission ¹³. © 2021 American Chemical Society.

Table 3.1 Summary of electric parameters of CZTS devices with different SnO₂ thickness.

This table has been published as our previous work in ¹³. Reproduced with permission ¹³. © 2021 American Chemical Society.

SnO ₂ thickness	η (%)	V_{oc} (mV)	J_{sc} (mA/cm ²)	FF (%)	R_s (Ω cm ²)	R_{sh} (Ω cm ²)
0-cycle SnO ₂	6.82	638	20.4	52.4	1.13	163
1-cycle SnO ₂	7.01	637	19.3	57.0	1.13	312
2-cycle SnO ₂	8.16	648	20.4	61.7	0.89	315
3-cycle SnO ₂	8.47	657	20.5	62.8	0.70	319

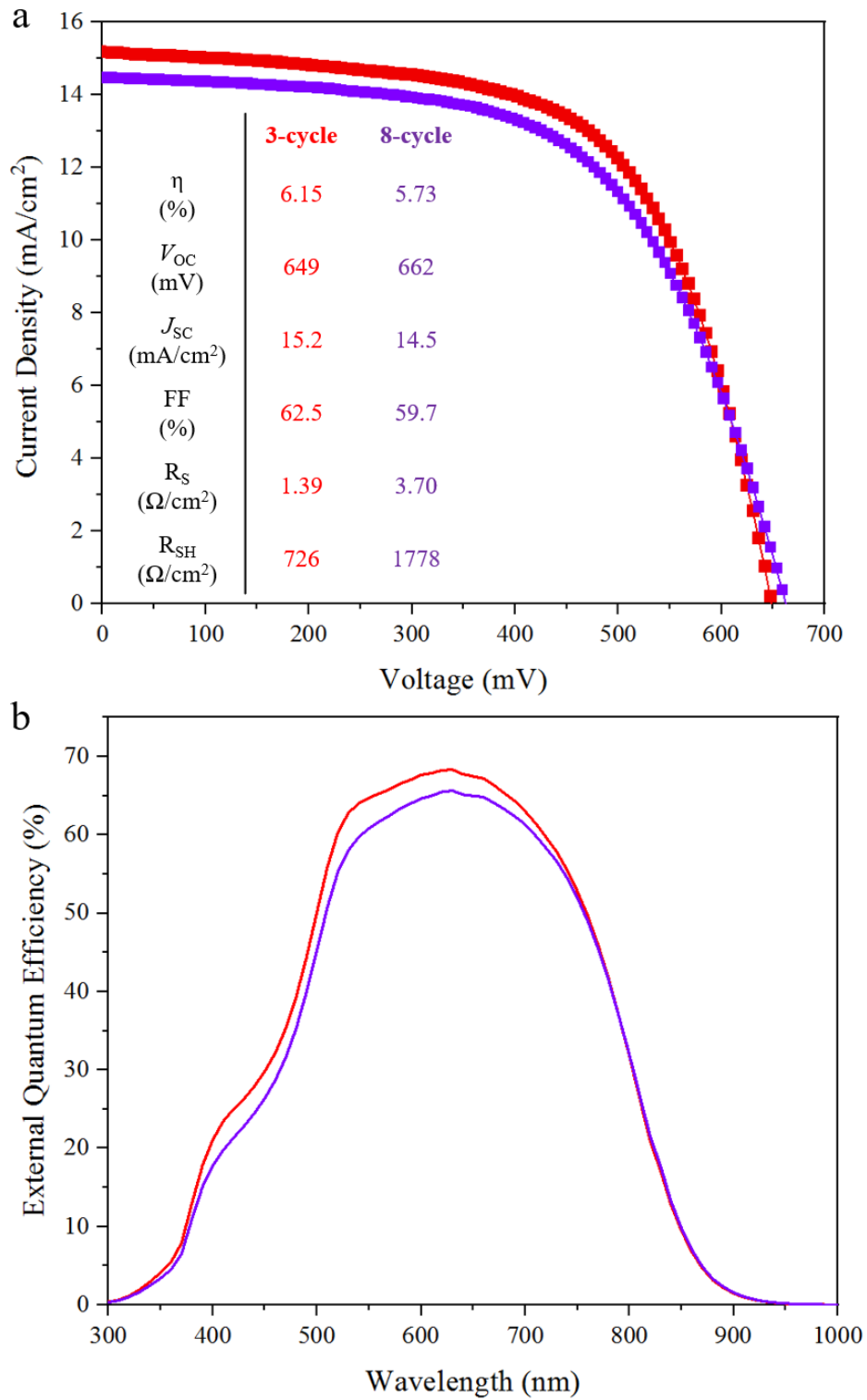


Figure 3.7 Comparison of device performance without antireflection coating upon passivation by SnO₂ by 3- and 8-SILAR cycle a. J - V curves, b. EQE spectra. This figure has been published as our previous work in ²⁰. Reproduced with permission ²⁰. © Copyright 2021 IEEE.

3.3.5 Limitations

As described in Section 3.3.3, weakened long-wavelength absorption restricted J_{SC} improvement, which can be explained by the reduction of depletion region width (W_d), measured from the C - V measurement, as shown in Figure 3.8. This, in turn, reduces the collection depth within CZTS. The reason for the W_d reduction may be associated with the polarization of the SnO_2 layer, which had been reported elsewhere ²¹. The polarization of SnO_2 results in the accumulation of negative charges at the CdS/CZTS interface, partially counteracting the electric field within the heterojunction. Consequently, it results in a shallower junction depth and weaker band bending, which can also partially limit the V_{OC} improvement.

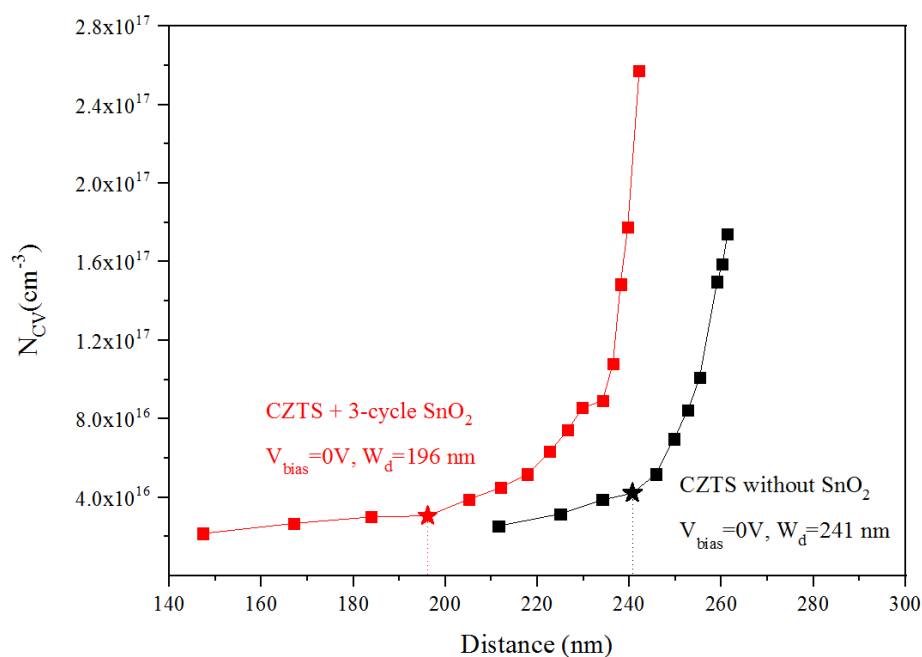


Figure 3.8 Doping profiles for the devices without and with SnO_2 from C - V measurement. This figure has been published as our previous work in ¹³. Reproduced with permission ¹³. © 2021 American Chemical Society.

3.3.6 Change in CdS

The improvement of short-wavelength response is arisen from the reduction of CdS parasitic absorption due to a thinner CdS layer grown on the SnO₂-coated CZTS during the CBD process, as seen in the TEM images in Figure 3.9. As the CdS films grown on these samples were fabricated in the same CBD batch with good uniformity, it is supposed that the growth rate of CdS on the SnO₂ matrix is lower than that epitaxially grown on the CZTS surface²⁰. The epitaxial growth on CZTS surface can be achieved due to their similar cubic lattice structure²². CdS has relatively low band gap energy at around 2.42 eV, leading to optical loss from the parasitic absorption of CdS in the short-wavelength region, which can be ameliorated by reducing CdS thickness. However, reduction of CdS thickness abates V_{OC} and FF which is commonly observed in chalcopyrite²³ and kesterite solar cells²⁴, showing the increased shunting problem. The application of the ultrathin SnO₂ layer seems to allow the reduction of CdS thickness without noticeably sacrificing R_{SH} .

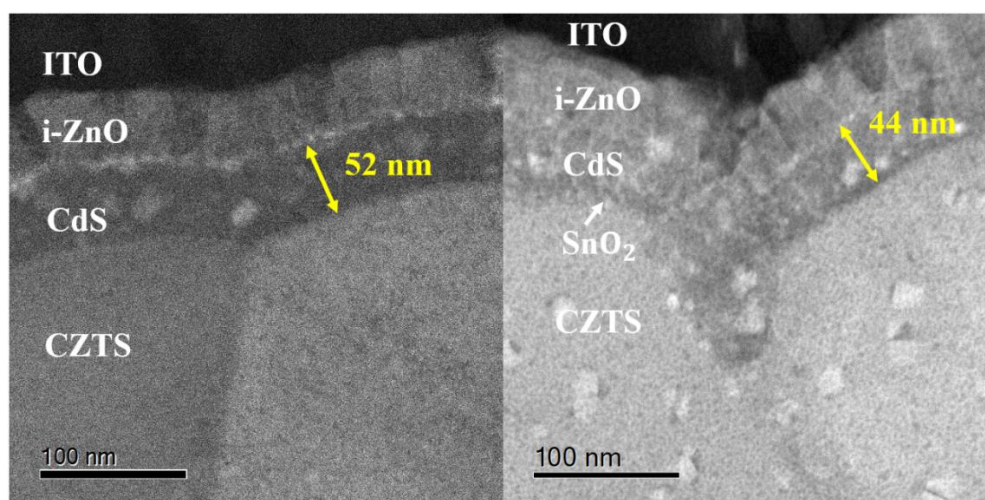


Figure 3.9 TEM images showing the reduction of CdS thickness grown on an ultrathin SnO₂ layer. This figure has been published as our previous work in¹³. Reproduced with permission¹³. © 2021 American Chemical Society.

3.3.7 Thinner CdS for Parasitic Absorption Mitigation

Considering the shunt-blocking feature of the SnO₂ layer, CdS buffer layers with smaller thickness were applied to the SnO₂-passivated CZTS devices. From the literature ²⁴, the reduction of CdS thickness results in a severe shunting problem, where substantial drops in FF and V_{OC} have been observed. The thickness of CdS can be roughly estimated from quantum efficiency measured between ~400 and 540 nm in EQE spectra. With the aid of the SnO₂ layer, as shown in Figure 3.10a and Table 3.2, a much larger drop in CdS thickness shows limited decreases in both V_{OC} and FF. Changing the CBD duration from 8 min to 6 min, though FF still decreased slightly, the decrement is much smaller than what reported in the literature ²⁴. Overall, better device performance can be expected due to the improvement of J_{SC} using the optimal CBD duration between 6-8 min with the aid of this SnO₂ shunt-blocking layer. The yield of V_{OC} at a mere 585 mV for SnO₂-passivated CZTS with 4-min CBD-CdS buffer does not arise from the shunting problem as FF does not drop a lot. Instead, it is caused by the limited quasi-fermi level splitting within the CdS n-type layer due to the inadequate W_d within such a thin CdS layer, which starts growing on CZTS between 3-4 min. Excluding the reduction of W_d within CZTS, the variation of CdS thickness does not deteriorate the photocarrier collection within the CZTS layer, as illustrated in Figure 3.10b. The decrease of CdS thickness leads to the reduction of CdS E_g ²⁵ which reduces the cliff-like band offset between SnO₂ and CdS while the valence band position does not change ²⁴. The modification of the heterointerface can also be seen from the enhanced charge collection between 550 and 650 nm in Figure 3.10b. Therefore, the insertion of this ultrathin SnO₂ intermediate layer between CdS and CZTS enables the use of thinner CdS with constrained shunting problems, resulting in not only the enhancement of current gain, but also the optimization of band alignment.

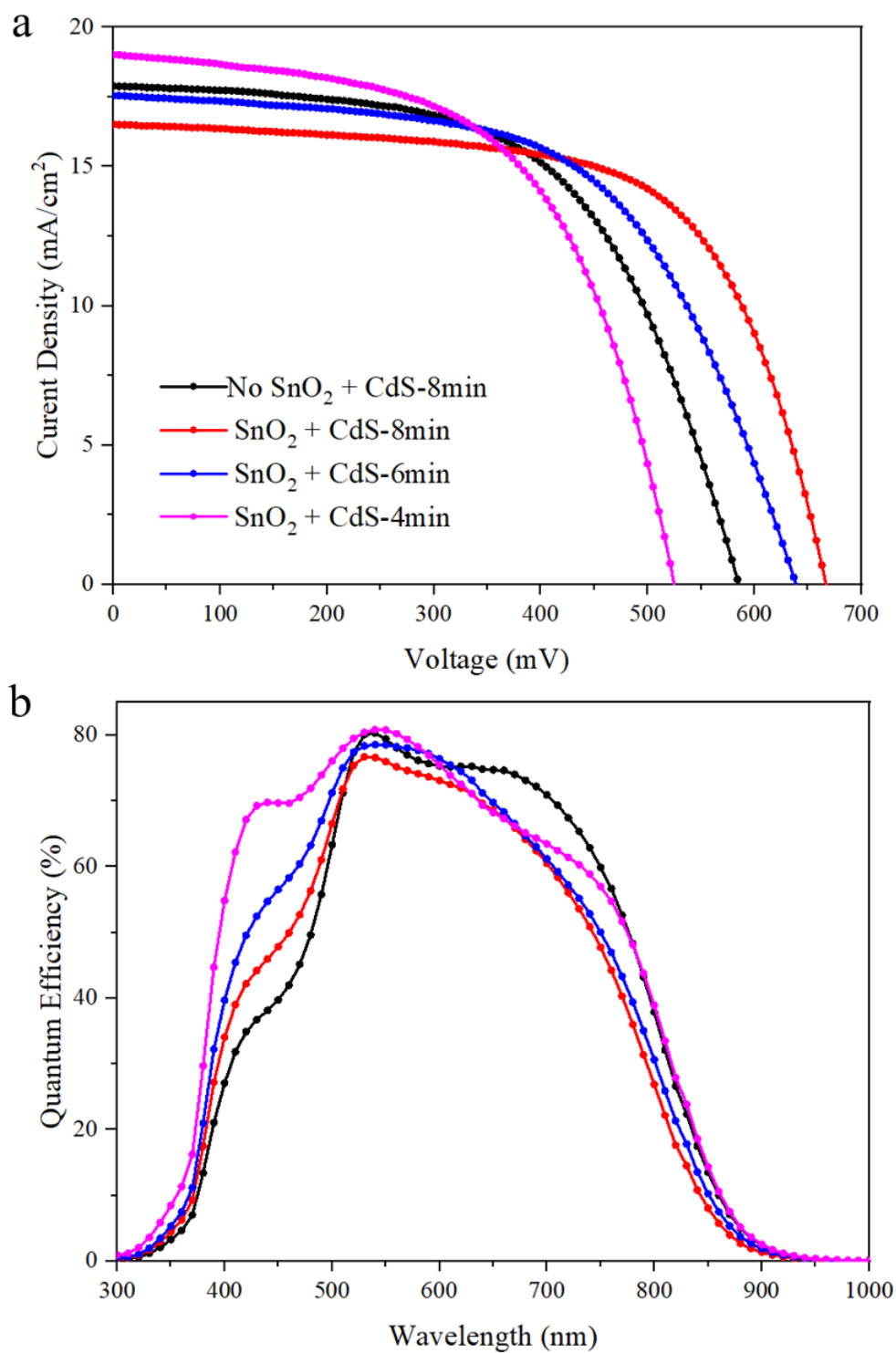


Figure 3.10 Comparison with the CZTS devices with different CdS thickness without and with SnO₂ passivation layer fabricated by 3 SILAR cycles. Note that these devices have not coated by antireflection coating.

Table 3.2 Electric parameters of devices in Figure 3.10

Device	V_{oc} (mV)	J_{sc} (mA/cm ²)	FF (%)	η (%)
No SnO ₂ + CdS-8min	585	17.9	58.1	6.08
SnO ₂ + CdS-8min	667	16.5	64.6	7.11
SnO ₂ + CdS-6min	639	17.5	58.2	6.84
SnO ₂ + CdS-4min	525	19.0	57.3	5.71

3.3.8 Mechanisms of the CdS/CZTS Heterointerface Passivation

The mechanisms of WBG dielectric layers used as passivation layer are generally investigated through chemical ⁸, field-effect/band-aligning ², lattice-matching ¹ and element-/shunt-blocking routes ^{4,8}. With respect to the passivation mechanisms of the ultrathin SnO₂ intermediate layer, three possible routes could be involved: 1. The shunt-blocking feature is obvious from the increase of R_{SH} and inhibition of degradation using thinner CdS. 2. Oxygen reacts with the CZTS surface, which passivates the local defects. The beneficial role of O has been reported in kesterite materials ^{26,27}. 3. The insertion of this WBG layer enhances the field effect for charge separation and modifies the band alignment.

To investigate how this WBG dielectric layer affects the band alignment at the junction region, the band diagram in Figure 3.11 has been plotted by considering the “cliff”-like CBO of -0.21 eV between CZTS and CdS (derived from XPS measurement with known bandgap ²⁸), SnO₂ band gap (3.7 eV, measured in this work, which may be underestimated due to

much thinner thickness applied in the CZTS devices) as well as the band alignment at the junction of CdS and SnO₂ ²⁵. According to this literature, a “spike”-like CBO at around 0.1 eV between CdS and SnO₂ with relatively low doping concentration is measured by photoelectron spectroscopy. Therefore, the conduction band position of the SnO₂ layer lies between that of CZTS and CdS, acting as a mediator of the conduction band alignment to enable the alleviation of the SRH recombination at the heterointerface. Additionally, the enlarged valence band offset (VBO), which stemmed from the large E_g of SnO₂, can effectively shield holes generated within CZTS away from the junction, enhancing the charge separation. Holes generated at the CdS side can tunnel through this thin SnO₂ layer. However, thicker SnO₂ could interfere with the hole tunnelling through SnO₂ from CdS to CZTS difficult and give rise to the larger series resistance. Additionally, as discussed, the application of a thinner CdS buffer layer may further optimize the conduction band alignment of CdS and SnO₂ (reduces the “cliff”-like CBO between SnO₂ and CdS).

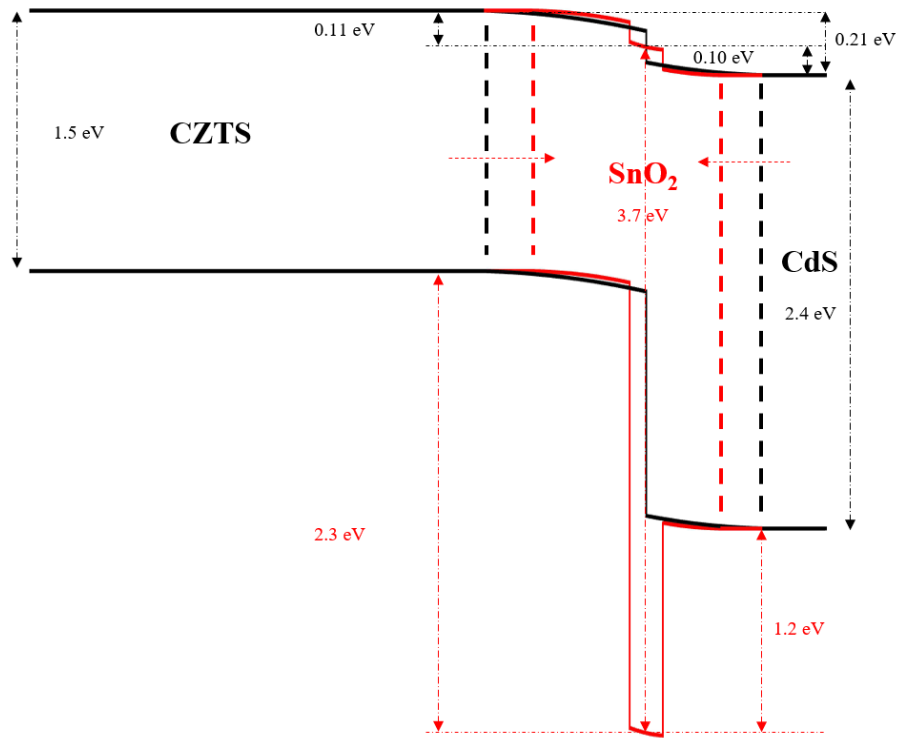


Figure 3.11 Schematic band diagrams of the CZTS/SnO₂/CdS heterojunctions, which has been constructed by combining the XPS core-level measurement for CZTS/CdS heterointerface²⁸ with the band alignment for CdS/SnO₂ junction from the literature²⁵.

3.4 Summary

This section has demonstrated an effective passivation route for the heterojunction by introducing an intermediate ultrathin stannic oxide layer between the CdS buffer and the CZTS absorber layers through the SILAR method. Applying this layer yields an improved minority carrier lifetime, which results in an increased V_{OC} and FF, and hence the efficiency of the CZTS solar cells. The thickness of the SnO₂ layer is critical for the device performance improvement: inadequate thickness limits the passivation effect while too thick SnO₂ could yield higher series resistance and poorer carrier collection. Furthermore, parasitic absorption by CdS layer decreased due to the reduced CdS thickness because of a slower growth rate of

the CdS layer on the SnO₂-coated CZTS. The thickness reduction does not sacrifice V_{OC} and FF. A further investigation has done to investigate the optimized CdS thickness for the device with the SnO₂ passivation layer. The deterioration of V_{OC} and FF was significantly mitigated with the aid of this SnO₂ shunt-blocking layer. However, the insertion of this dielectric layer induces the reduction of depletion region width in the CZTS layer, showing a poorer spectral response at the relatively long wavelength and partially inhibit the substantial V_{OC} improvement. The passivation mechanisms are proposed that this ultrathin SnO₂ layer not only provides a chemical passivation route, but it also modifies the band alignment at the heterojunction through optimizing the charge separation and buffering the CBO between CZTS and CdS. Overall, this work provides an insight into passivation of the CZTS/CdS heterointerface, modification of band alignment, as well as shunt blocking which enables the application of thinner CdS for increasing the current gain. Last but not least, this NH₄OH-resistant layer can be applied to conventional kesterite solar cells with the CBD-CdS buffer or other solution-processed buffer materials, such as Zn(O,S) ²⁹.

3.5 Reference

- 1 Crovetto, A. *et al.* Lattice-matched Cu₂ZnSnS₄/CeO₂ solar cell with open circuit voltage boost. *Applied Physics Letters* **109**, 233904 (2016).
- 2 Hoex, B., Gielis, J., Van de Sanden, M. & Kessels, W. J. J. o. A. P. On the c-Si surface passivation mechanism by the negative-charge-dielectric Al₂O₃. *Journal of Applied Physics* **104**, 113703 (2008).
- 3 Hsu, W.-W. *et al.* Surface passivation of Cu (In, Ga) Se₂ using atomic layer deposited Al₂O₃. *Applied Physics Letters* **100**, 023508 (2012).
- 4 Lee, Y. S. *et al.* Atomic Layer Deposited Aluminum Oxide for Interface Passivation of Cu₂ZnSn (S, Se) ₄ Thin-Film Solar Cells. *Advanced Energy Materials* **6**, 1600198 (2016).
- 5 Cui, X. *et al.* Cd-Free Cu₂ZnSnS₄ solar cell with an efficiency greater than 10% enabled by Al₂O₃ passivation layers. *Energy & Environmental Science* **12**, 2751-2764 (2019).
- 6 Park, J. *et al.* The Role of Hydrogen from ALD-Al₂O₃ in Kesterite Cu₂ZnSnS₄ Solar Cells: Grain Surface Passivation. *Advanced Energy Materials* **8**, 1701940 (2018).
- 7 Sardashti, K. *et al.* Impact of nanoscale elemental distribution in high-performance kesterite solar cells. *Advanced Energy Materials* **5**, 1402180 (2015).
- 8 Sinsermsuksakul, P. *et al.* Overcoming efficiency limitations of SnS-based solar cells. *Advanced Energy Materials* **4**, 1400496 (2014).
- 9 Tajima, S. *et al.* Sodium distribution in solar-grade Cu₂ZnSnS₄ layers using atom-probe tomographic technique. *Japanese Journal of Applied Physics* **54**, 112302 (2015).
- 10 Schwarz, T. *et al.* Variable chemical decoration of extended defects in Cu-poor Cu₂ZnSnS₄ thin films. *Physical Review Materials* **3**, 035402 (2019).

- 11 Deshpande, N. G., Vyas, J. C. & Sharma, R. J. T. S. F. Preparation and characterization of nanocrystalline tin oxide thin films deposited at room temperature. *Thin Solid Films* **516**, 8587-8593 (2008).
- 12 Yıldırım, M. A., Akaltun, Y. & Ateş, A. J. S. s. Characteristics of SnO₂ thin films prepared by SILAR. *Solid State Sciences* **14**, 1282-1288 (2012).
- 13 Sun, H. *et al.* Efficiency Enhancement of Kesterite Cu₂ZnSnS₄ Solar Cells via Solution-Processed Ultrathin Tin Oxide Intermediate Layer at Absorber/Buffer Interface. *ACS Applied Energy Materials* **1**, 154-160 (2017).
- 14 Hurtado, M. *et al.* in *2014 IEEE 40th Photovoltaic Specialist Conference (PVSC)*. 0368-0372 (IEEE).
- 15 Dang, W. *et al.* Composition controlled preparation of Cu–Zn–Sn precursor films for Cu₂ZnSnS₄ solar cells using pulsed electrodeposition. *Journal of Alloys and Compounds* **650**, 1-7 (2015).
- 16 Di Giulio, M. *et al.* SnO₂ thin films for gas sensor prepared by rf reactive sputtering. *Sensors and Actuators B: Chemical* **25**, 465-468 (1995).
- 17 Ohnesorge, B. *et al.* Minority-carrier lifetime and efficiency of Cu (In, Ga) Se₂ solar cells. *Applied Physics Letters* **73**, 1224-1226 (1998).
- 18 Sun, K. *et al.* Influence of sodium incorporation on kesterite Cu₂ZnSnS₄ solar cells fabricated on stainless steel substrates. *Solar Energy Materials and Solar Cells* **157**, 565-571 (2016).
- 19 Tao, J. *et al.* A sputtered CdS buffer layer for co-electrodeposited Cu₂ZnSnS₄ solar cells with 6.6% efficiency. *Chemical Communications* **51**, 10337-10340 (2015).
- 20 Sun, H. *et al.* Solution-processed ultrathin SnO₂ passivation of Absorber/Buffer Heterointerface and Grain Boundaries for High Efficiency Kesterite Cu₂ZnSnS₄

- Solar Cells. *2019 IEEE 46th Photovoltaic Specialists Conference (PVSC)*. IEEE, (2019).
- 21 Canestraro, C. D., Roman, L. S. & Persson, C. J. T. S. F. Polarization dependence of the optical response in SnO₂ and the effects from heavily F doping. *Thin Solid Films* **517**, 6301-6304 (2009).
 - 22 Liu, F. *et al.* Nanoscale microstructure and chemistry of Cu₂ZnSnS₄/CdS interface in kesterite Cu₂ZnSnS₄ solar cells. *Advanced Energy Materials* **6**, 1600706 (2016).
 - 23 Contreras, M. A. *et al.* Optimization of CBD CdS process in high-efficiency Cu (In, Ga) Se₂-based solar cells. *Thin Solid Films* **403**, 204-211 (2002).
 - 24 Hong, C. W. *et al.* Chemically Deposited CdS Buffer/Kesterite Cu₂ZnSnS₄ Solar Cells: Relationship between CdS Thickness and Device Performance. *ACS applied materials & interfaces* **9**, 36733-36744 (2017).
 - 25 Fritsche, J. *et al.* Band energy diagram of CdTe thin film solar cells. *Thin Solid Films* **403**, 252-257 (2002).
 - 26 Cahen, D. & Noufi, R. J. S. C. Surface passivation of polycrystalline, chalcogenide based photovoltaic cells. *Solar Cells* **30**, 53-59 (1991).
 - 27 Kim, J. H. *et al.* Atomic-Scale Observation of Oxygen Substitution and Its Correlation with Hole-Transport Barriers in Cu₂ZnSnSe₄ Thin-Film Solar Cells. *Advanced Energy Materials* **6** (2016).
 - 28 Yan, C. *et al.* Cu₂ZnSnS₄ solar cells with over 10% power conversion efficiency enabled by heterojunction heat treatment. *Nature Energy* **3**, 764-772 (2018).
 - 29 Li, J. *et al.* Restraining the Band Fluctuation of CBD-Zn (O, S) Layer: Modifying the Hetero-Junction Interface for High Performance Cu₂ZnSnSe₄ Solar Cells With Cd-Free Buffer Layer. *Solar RRL* **1** (2017).

Chapter 4

Elemental Redistribution Induced Heterojunction Modification by Moisture-assisted Post-deposition Annealing

4.1 Introduction

As discussed in Chapter 2, the non-radiative recombination at the heterojunction region is one of the main loss mechanisms in CZTS devices. In Chapter 3, we employed an ultrathin dielectric layer to passivate the heterointerface. In this chapter, a new strategy is developed for heterojunction modification by manipulating the distributions of critical trace elements.

The beneficial effect of Cd incorporation has been intensively investigated in kesterite semiconductors either through directly alloying Cd during CZTS formation, or alternatively through post-deposition diffusion ¹⁻⁷. Cd alloying at the former stage was beneficial in reducing the band tailing ⁴, increasing minority carrier lifetime, and promoting grain growth ¹. Cd incorporation within the CZTS/CdS heterojunction is considered as an effective method to modify the heterojunction through alleviating the local non-radiative recombination and optimizing the band alignment ^{3,5,6,8-11}. In previous studies, we have investigated Cd ion soaking ⁶ and heterojunction annealing, which realized the incorporation of Cd ions into CZTS absorbers ³, revealing the improvement of heterojunctions. However, no remarkable Cd diffusion was observed through Cd ion soaking treatment ⁶, and the latter approach at relatively high annealing temperature may yield unfavourable ZnS secondary phases at the heterointerface ^{3,12}. Apart from Cd, Na diffused from the soda-lime glass (SLG) substrates during the sulfurization process is a generally recognized critical dopant in kesterite semiconductors, which is beneficial for improving the grain growth ¹³, hole concentration and

conductivity¹³⁻¹⁶, and passivation of grain surfaces and grain boundaries (GBs)¹⁶⁻¹⁸. However, the presence of Na was reported to inhibit the diffusion of favourable Li through post-deposition treatment (PDT)². For a similar reason, we speculate that the presence of excessive Na could be the origin of the diffusion barrier of some other beneficial elements incorporating into CZTS films through post-treatments. Relative to Na passivation at grain surface and boundaries for the as-formed kesterite materials, it seems that Cd has more beneficial roles in the modification of heterojunction when incorporates into the CZTS lattice.

Herein, we break the routine by reducing the Na concentration within the CZTS film to facilitate more Cd diffusion into this layer. This has been accomplished by a novel moisture-assisted post-deposition annealing (MAPDA) treatment upon bare CZTS films, which in turn enables spontaneous Cd diffusion and activation during the follow-up CdS chemical bath deposition (CBD) process. The mechanism of alkali removal is then excavated. Comprehensive characterizations were employed to investigate the outcomes from the elemental redistribution, including defect modifications and thereby the device performance.

4.2 Experimental

Before performing the MAPDA treatment, the as-formed CZTS samples were preserved in a N₂ atmosphere to prevent oxidation at the surface¹⁷. The MAPDA treatment was conducted by annealing the CZTS samples in a moistened N₂ atmosphere with relative humidity at 100 %. The experimental apparatus was designed in-house specifically for this process, as shown in Figure 4.1, which was composed of three parts: Gas Flow Control, a Moisture Generator, and an annealing section (Humid Box and Hot Plate). Gas Flow Control regulated the dry N₂ flow rate passing through the bubbler which merged into a flask filled with de-

ionized water, as displayed in the Moisture Generator. The water molecules carried by N_2 flow exhausted from the exhaust nozzle of the Humid Box. Dry N_2 was moistened to 100 % relative humidity (RH) at room temperature by controlling the gas flow rate, and the RH was continuously monitored using a humidity sensor. For understanding the role of moisture in the annealing process, dry N_2 with a RH close to 0% was also used in the post-annealing process. The MAPDA process commenced once CZTS samples started annealing on a hot plate in the saturated N_2 atmosphere. The treatment was performed at a temperature between 200 °C and 350 °C for 5 min, aiming to investigate the impacts of annealing temperature. The detail of fabrication methods for other layers is presented in Chapter 2 (Section 2.4).

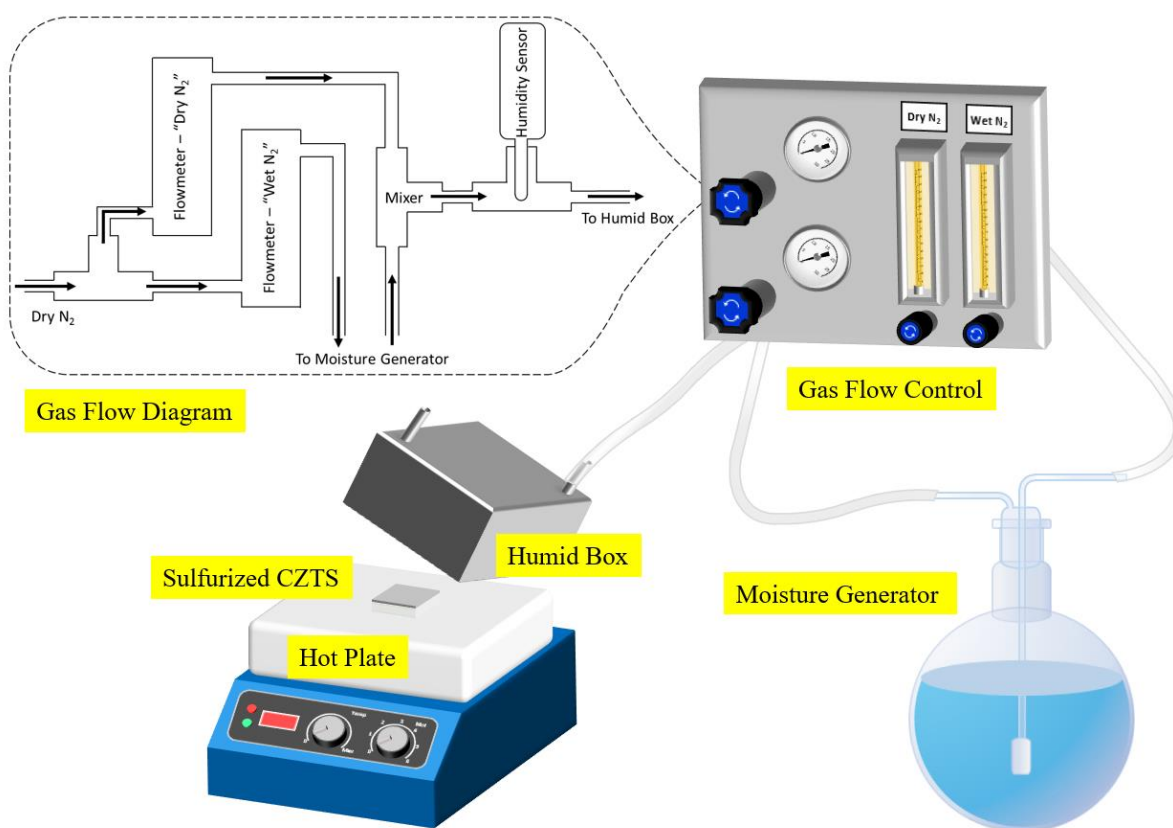


Figure 4.1 Schema of the experiment apparatus explicitly designed for MAPDA treatment. The inset shows the gas flow diagram for the system.

J-V characteristics were measured at 1000 W/m^2 (AM 1.5G) from a solar simulator (ABET IV Tester). EQE measurement was performed through a QEX10 spectral response system (PV Measurements, Inc.). Suns-Voc measurements were performed under decaying pulsed light from a xenon flash lamp with a full-width at half maximum (FWHM) of about 2 ms. The TEM specimens were prepared using a focused ion beam (FIB) micro-sampling system (FEI xT Nova NanoLab 200). The microstructure and compositional profiles were measured by a JEOL F200 (200 kV) cold field emission gun (FEG) Scanning Transmission Electron Microscope (STEM) equipped with a windowless silicon drift energy dispersive x-ray (EDX) detector. For the capacitance-voltage (*C-V*) measurement, an impedance analyzer was used with a frequency at 10k Hz and a DC bias voltage sweeping from -1.6 to 1.2 V and stepping of 0.2 V. While the drive-level capacitance profiling (DLCP) measurement was conducted with the AC amplitude varied from 20 to 140 mV and the same DC range. The admittance spectroscopy was performed using an LCR meter (E4980A, Agilent) in an electromagnetic shielding box from 120 to 300 K, with scanning frequency from 25 Hz to 1 MHz, and 50 mV AC amplitude. Raman spectra were obtained with the Renishaw in via Raman Microscope using a 785 nm laser.

Time-of-flight secondary ion mass spectrometry (ToF-SIMS) was used to analyze the distributions of trace alkali metal elements in CZTS devices with atomic fraction much less than 1 %^{19,20}, which took advantage of the low trace element detection limits (from ppm to ppb²¹ range for most species). CZTS device surfaces were bombarded by a pulsed, energetic Cs⁺ ion beam²² under high vacuum condition (7×10^{-10} mbar), in conjunction with the detection of MCs⁺ molecular ions²³, where M represents the element interested. In this MCs⁺ mode, information of both cations and anions can be directly obtained (e.g., the depth profiles

of F can be collected from Cs_2F^+ , which formed by coupling one F^- with two Cs^+). Compared to atomic probe tomography (APT), ToF-SIMS neither gives quantitative analysis nor distinguish grains and GBs, whereas it analyses in a large area showing typical and statistical information of elemental distributions. Figure 4.2 demonstrates a schematic ToF-SIMS system. The measurements were conducted on a TOF-SIMS5 instrument manufactured by ION-TOF GmbH Münster Germany, using a Cs^+ sputter beam at 1 kV and 75 nA operating over a $300\text{ }\mu\text{m} \times 300\text{ }\mu\text{m}$ raster of the surface and a primary Bi^{3+} beam at 30 keV and 0.34 pA within the analyzed area of $100\text{ }\mu\text{m} \times 100\text{ }\mu\text{m}$.

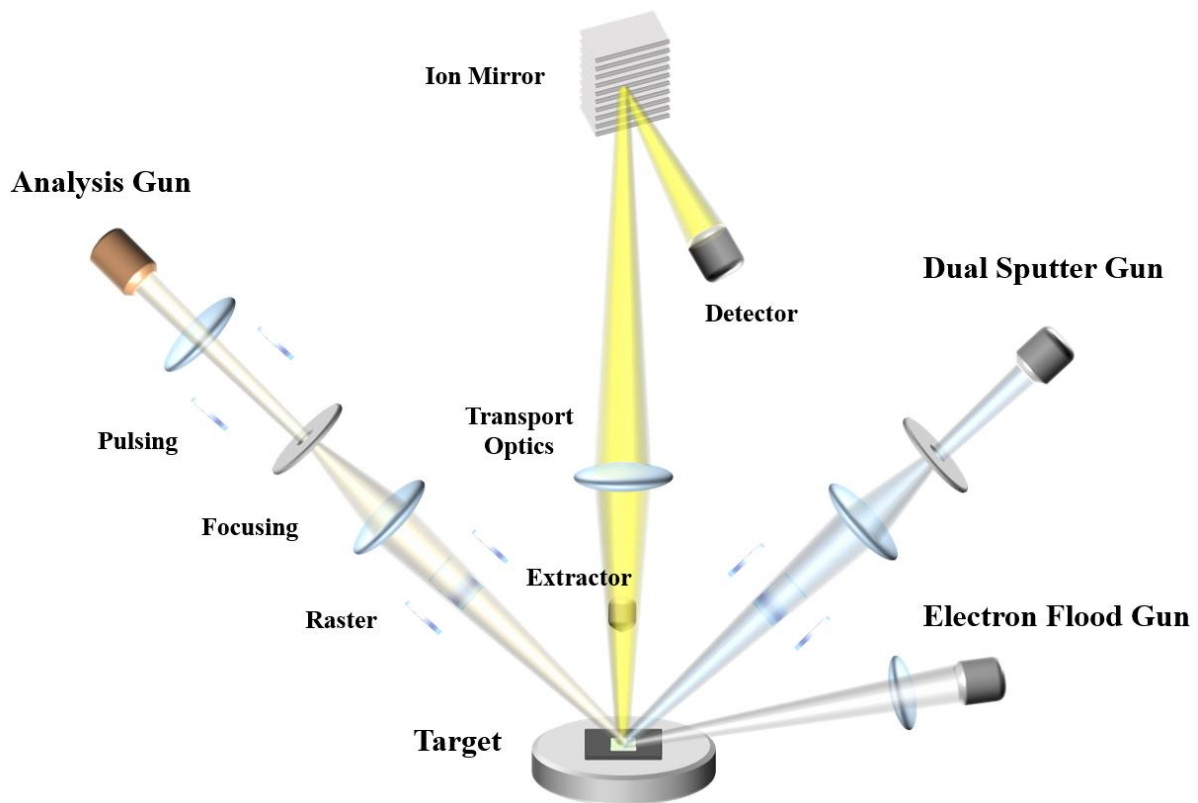


Figure 4.2 Schematic diagram of a time-of-flight secondary ion mass spectrometry system.

4.3 Results and Discussion

4.3.1 Manipulation of Critical Trace Elements

As one of the critical trace elements in CZTS, Na can be easily altered in distribution through post-deposition annealing (PDA) ²⁴⁻²⁶. A higher concentration of Na diffused into the heterojunction after the post-heat treatment has been observed ³. However, herein, performing the PDA with the presence of water eventually yielded Na-depleted CZTS films, particularly at the heterojunction region, which was supported by the ToF-SIMS measurements on the completed CZTS devices. Figure 4.3a shows the structure of the devices and the depth range for the ToF-SIMS analysis. We denote the control device as REF and devices with MAPDA treatment at the different annealing temperatures as MA-200C, MA-260C and MA-350C, respectively. Without MAPDA treatment, the peaks of Na concentration can be seen at the CZTS/Al₂O₃/MoS₂ heterointerfaces, the CdS/ZnO heterointerface extending to the CZTS surface with high concentration, as well as a hump at the middle-bottom region of CZTS film (where more small grains present). The trend of Na distribution measured by ToF-SIMS results is coincident with the atom probe tomography (APT) results reported elsewhere ^{3,19,20} that most Na ions are generally observed at the rear heterointerface, the CdS layer and the CZTS grain boundaries. Regarding the CdS/CZTS heterointerface, in general, a high concentration of Na at the CZTS surface-most regions was washed off in the CdS precursor solution during the CdS-CBD process ²⁷. The residuals, to some extent, migrated into the CdS layer until blocked by the compact intrinsic ZnO layer. Although Na and K can be partially removed by the CBD process, the MAPDA-treated samples still show significantly lower Na and K concentrations, not only at the heterojunction, but also throughout the entire CdS and the CZTS layers. The decrement of both alkali metals is dependent on the MAPDA temperature. On the other hand, annealing at 350 °C diffused more Na and K from the SLG substrate to the rear interfaces, but the considerably lower diffusion rate of these

supplementary alkali metals into the CZTS layer could not compensate the loss of these elements from the CZTS surface, resulting in the net loss within the CZTS bulk. The clear contrast can be seen in Figure 4.3f through merging the Na and K profiles in a single graph by normalizing the counts according to the bulk S concentration and in Figure 4.4 through displaying the 3D render images of both alkali metal distributions.

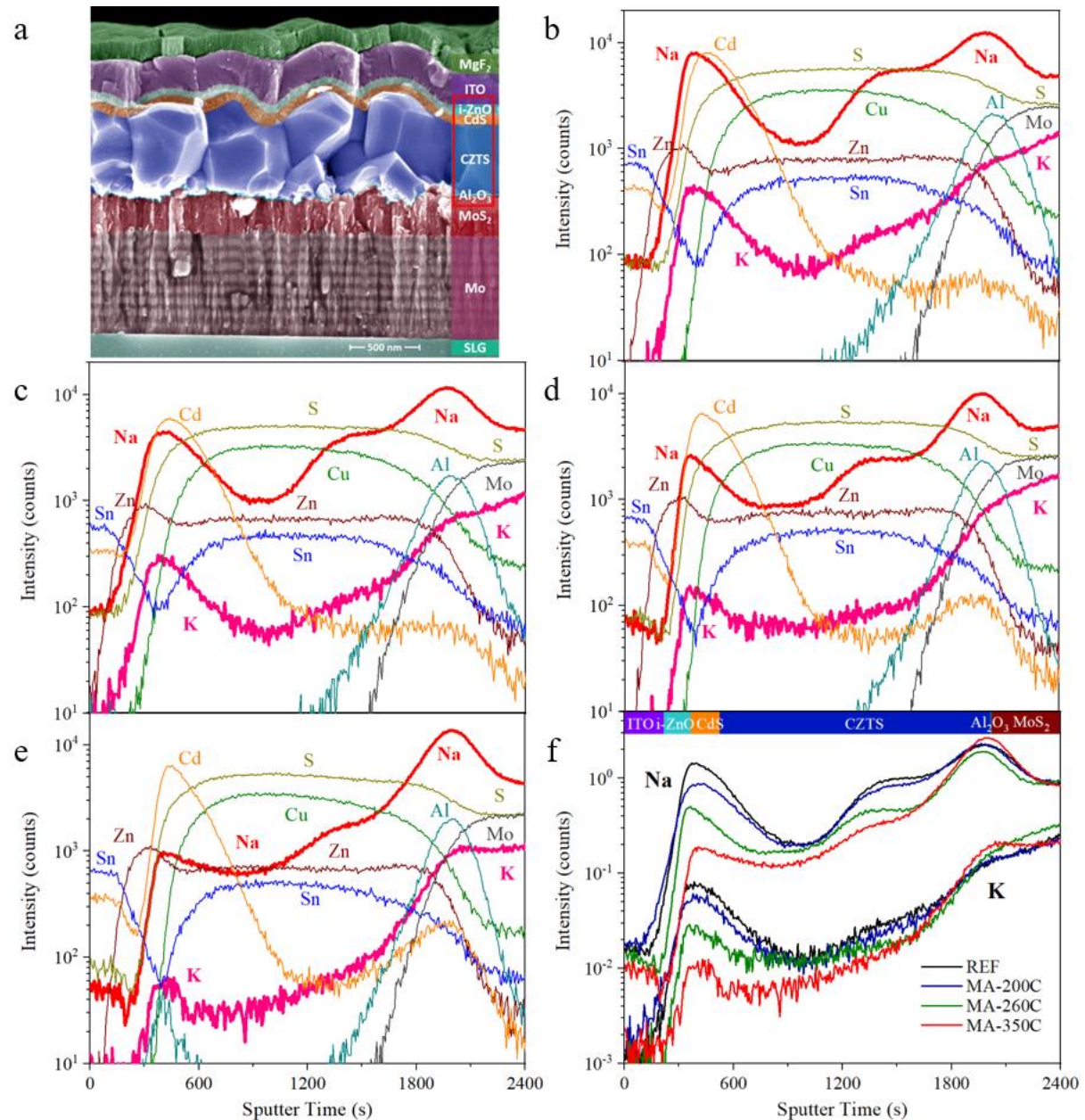


Figure 4.3 a. cross-section SEM image of a finished CZTS device. The area marked by a red rectangle represents the depth range selected in the ToF-SIMS profiles of b. REF. c. MA-

200C. d. MA-260C. e. MA-350C. Na and K distributions are highlighted in red and pink, respectively. f. the combined profiles of Na and K among these four specimens.

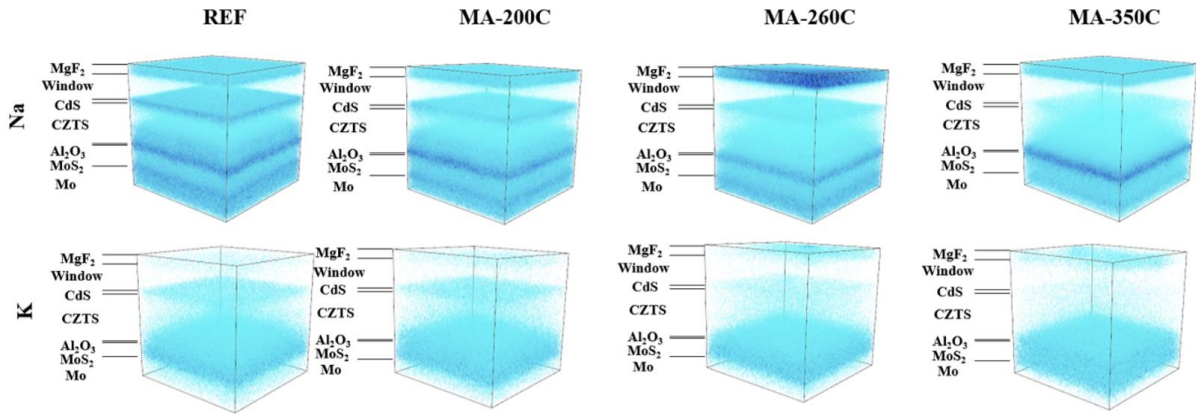


Figure 4.4 Three dimensional distributions of Na and K in a x-y dimension of $100\ \mu\text{m} \times 100\ \mu\text{m}$ from the surface of Mo to MgF_2 layers.

To find out the reasons of alkali loss, we conducted further investigations via ToF-SIMS measurements on the as-MAPDA CZTS samples and the finished CZTS devices undergone dry N_2 post-annealing prior to the CdS deposition. Both MAPDA and N_2 annealing were conducted at $350\ ^\circ\text{C}$ for 5 min. The former is denoted as MA5 and the latter as N_2 -5. As shown in Figure 4.5a, both Na and K were diffused from the CZTS bulk to the near-surface region of MA5 compared to REF. The diffusion of these alkali metals was associated with the presence of higher O and OH concentrations, as shown in the top panel of Figure 4.5a. By contrast, although post-annealing in the dry N_2 atmosphere can also promote Na and K diffusion at the front region, it has been reported²⁵ that the increase of their concentrations was observed throughout the entire absorber layer, and the net concentrations of Na and K are even higher than the control sample after the wet-etching stage during the CdS CBD process. Similarly, higher Na and K concentrations were witnessed by our ToF-SIMS measurement

for N₂-5, as shown in Figure 4.5b. The dry-N₂ annealing treatment was conducted using the same apparatus, temperature, duration and N₂ flow rate. Therefore, water moisture in the MAPDA treatment gives rise to the different Na and K diffusion dynamics. Water moisture penetrated the upper section of the CZTS bulk (possibly along the CZTS GBs²⁸), and reacted with the Na/K in this region to form OH- and O-phases which are highly soluble in aqueous solutions. Based on these observations, the removal of alkali elements could possibly involve two stages: 1. During the MAPDA treatment, Na and K diffuse from the bulk of CZTS to the surface and the near-surface regions, and reacted with water molecules to form highly water-soluble phases, such as NaOH, Na₂O, or as other Na-S(-O) phases²⁹, as well as Na₂CO₃ and NaHCO₃ during cooling at the ambient air atmosphere. 2. During the CBD process, these highly soluble phases are immediately removed in the hot ammonia solution in the chemical bath. Because a high concentration of Na has been driven from the deep bulk to the surface and the near-surface region, the removal of Na phases at these regions during the second stage results in the significant loss of Na within the CZTS layer.

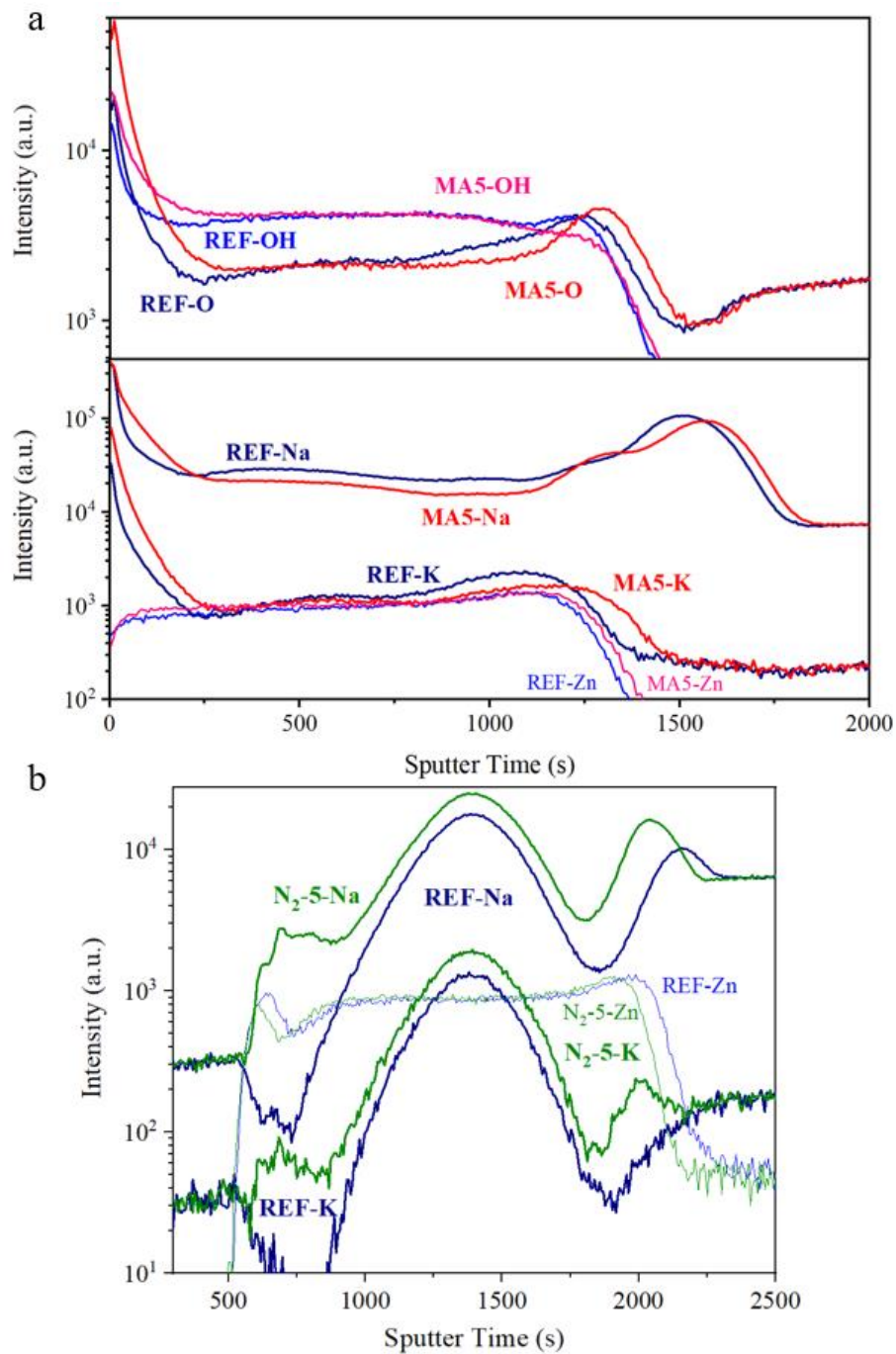


Figure 4.5 ToF-SIMS profiles for a. bare CZTS films w/ (MA5) and w/o (REF) MAPDA treatment at 350 °C for 5 min. The locations of OH, O, Na and K refers to Zn profiles of both samples. b. Finished CZTS cells w/ (N₂-5) and w/o (REF) dry N₂ annealing at 350 °C for 5 min from the different fabrication batch with those in Figure 4.5a, showing the Na and K distributions with reference to Zn profiles.

Accompanied by the reduction of Na concentration within the CZTS layer, it is also observed by TEM EDS measurement that a higher density of Cd accommodates within the CZTS grain interiors (GIs) and particularly at the GBs of the same cells which undergone the ToF-SIMS measurements. As shown in Figure 4.6a-d, elemental distribution profiles were obtained from the line scans across the sharp GBs of REF and MA-350C. In contrast to the ambiguous difference of Cd distributions at the GB and the neighbouring GIs of REF, a distinct peak of Cd concentration at the GB with an atomic fraction at around 1.5 % can be seen in MA-350C, as shown in Figure 4.6e. Besides, the Cd concentration within the adjacent GIs is also considerably higher.

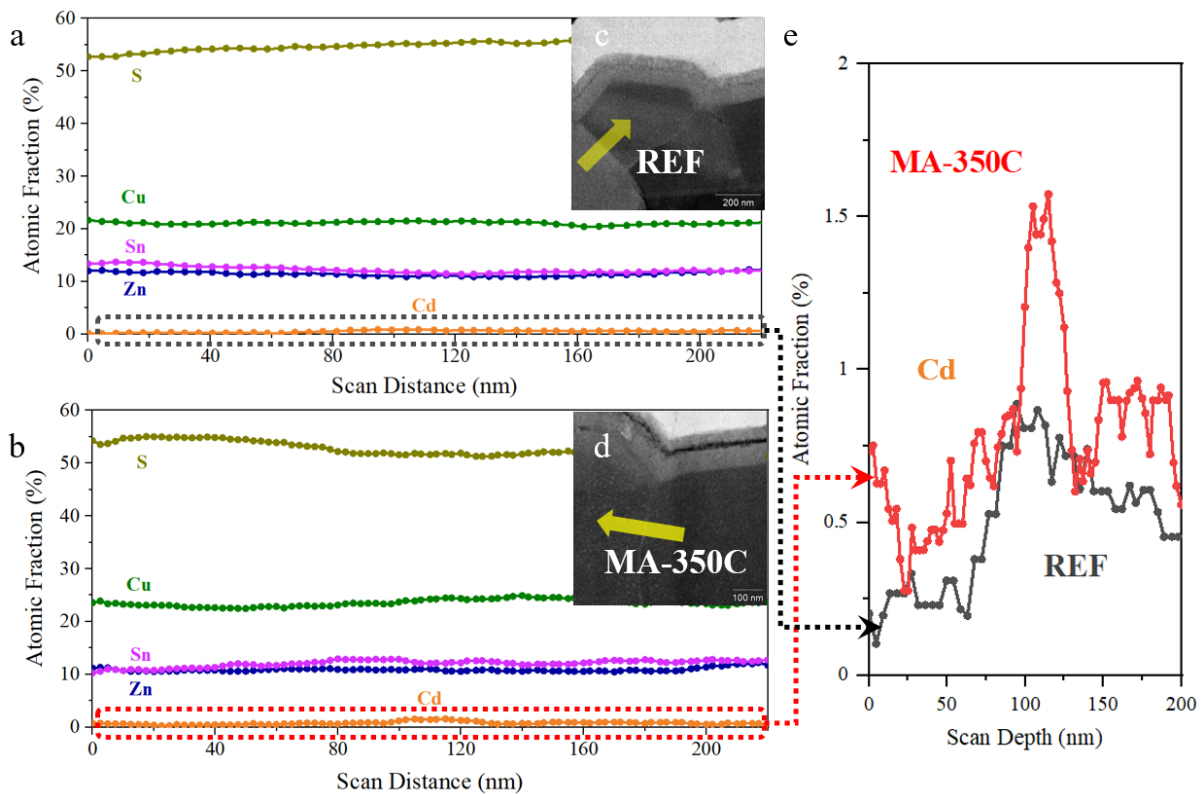


Figure 4.6 TEM-EDS line scans across CZTS grain boundaries of a. REF and b. MA-350C. TEM images showing the directions of line scans are included as the insets. c&d. TEM

images showing the line scan directions. e. zoom-in Cd distributions at the heterojunctions denoted in the dotted squares.

Figure 4.7 a-e demonstrate the line scan EDS results from the CdS top region until the CZTS bulk, across the entire CdS/CZTS heterojunction. As compared in Figure 4.6e, MAPDA treatment promotes Cd diffusion into the CZTS grain interior. Such considerable enhancement of Cd diffusion was achieved spontaneously during the 70 °C CdS-CBD process, without any additional heat treatment. Furthermore, for the MAPDA-treated cells, CdS shows Cd-deficit and S-enriched compositions with Cu concentration above 5 % in atomic fraction.

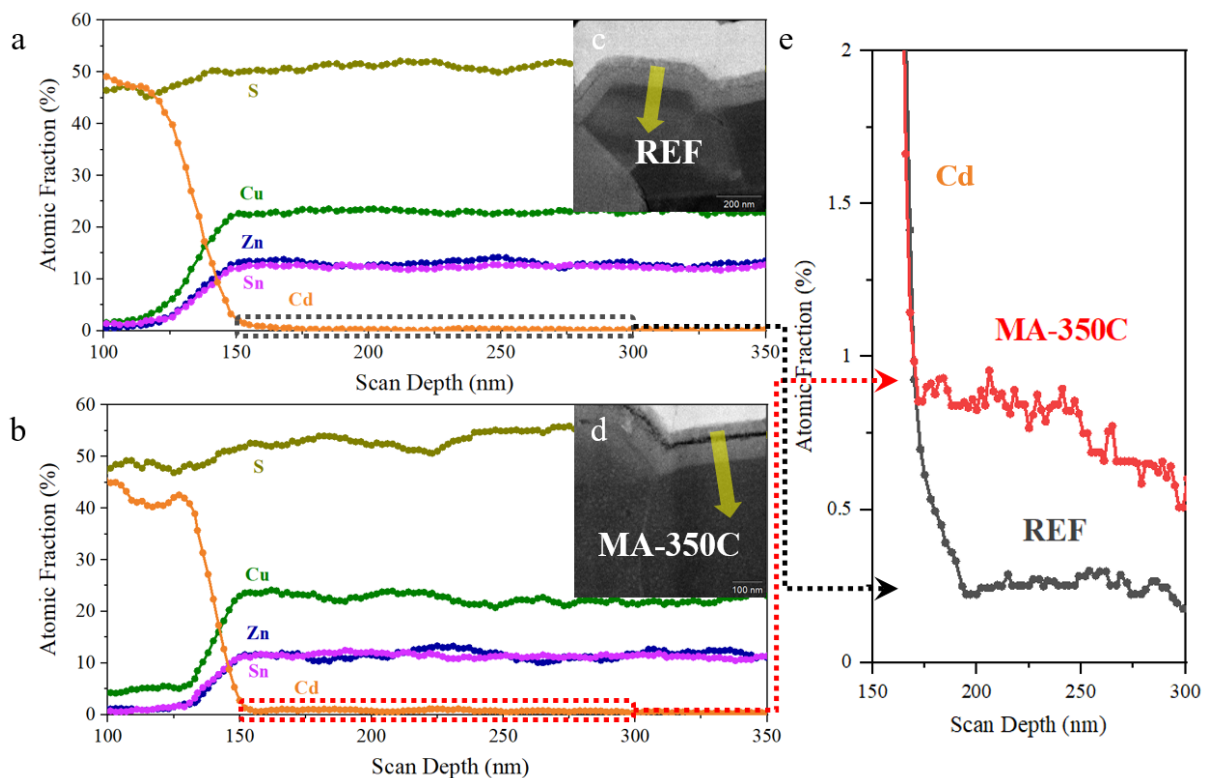


Figure 4.7 TEM-EDS line scans across heterojunctions of a. REF and b. MA-350C. c&d. TEM images showing the line scan directions. e. zoom-in Cd distributions at the heterojunctions denoted in the dotted squares.

Cd and Cu counter-diffusion is believed to be the result of the significant reduction of Na concentration within CZTS before the CdS deposition. As discussed previously, the loss of Na predominantly occurred at the grain surface, boundaries, and within the CZTS grains in lower content. Therefore, vacancies at these defects and within the CZTS structure left by the absence of Na could enhance the spontaneous diffusion of Cd into these positions during the CBD process. In the CdS layer, the density of Cd vacancies (V_{Cd}) would increase due to the significantly reduced alkali metal accumulation within CdS and the promoted Cd out-diffusion from CdS to CZTS. Higher V_{Cd} concentration within the CdS layer, in turn, drives more Cu from the CZTS layer into the CdS layer.

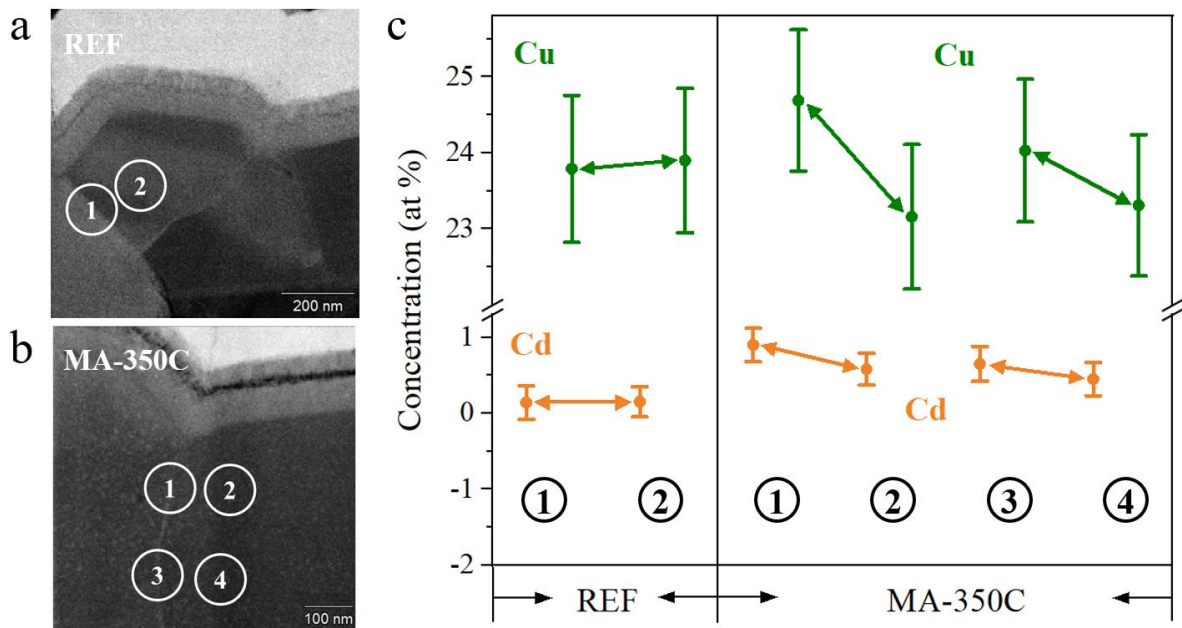


Figure 4.8 Selected area quantitative EDS analysis of GBs and GIs for Cd and Cu concentrations. a. TEM image for sample REF with mark 1 and 2 denoted GBs and GIs, respectively. b. TEM image for sample MA-350 with mark 1 and 2 for GBs and GIs at

shallower depth and 3 and 4 for those at deeper depth, respectively. c. Atomic concentrations of Cd and Cu for the selected areas in a&b.

Figure 4.8a-c show the selected area quantitative EDS analysis of GBs and GIs for Cd and Cu concentrations. As the selected area of the GBs also includes the adjacent GIs, the average values of local atomic concentration are underestimated. Nevertheless, we still can see higher Cd concentration at GBs of MA-350C and decrease along with the depth. Cd concentration in atomic fraction drops from $0.90 \pm 0.21 \%$ to $0.65 \pm 0.23 \%$ at the GB and from $0.58 \pm 0.21 \%$ to $0.45 \pm 0.22 \%$ within the GIs along approximately 200 nm depth. While in the REF device, rather limited Cd concentration ($\sim 0.15 \pm 0.22 \%$) presented at both the CZTS GB and the GI. In terms of the change in Cu concentration, MAPDA treatment facilitates the diffusion of Cu from the GIs to the GBs, while no big contrast in Cu concentration at both positions can be notably seen in REF. According to the first-principles calculation, dangling bonds can also be saturated through introducing Cu at the GBs¹⁸, which could facilitate the GB passivation. Furthermore, the precipitation of ZnS secondary phases within the CZTS layer can also be observed in MA-350C (Figure 4.9d&e), which may lead to the increase of Cu/Zn ratio within CZTS grains, as can be seen in Figure 4.9a-c.

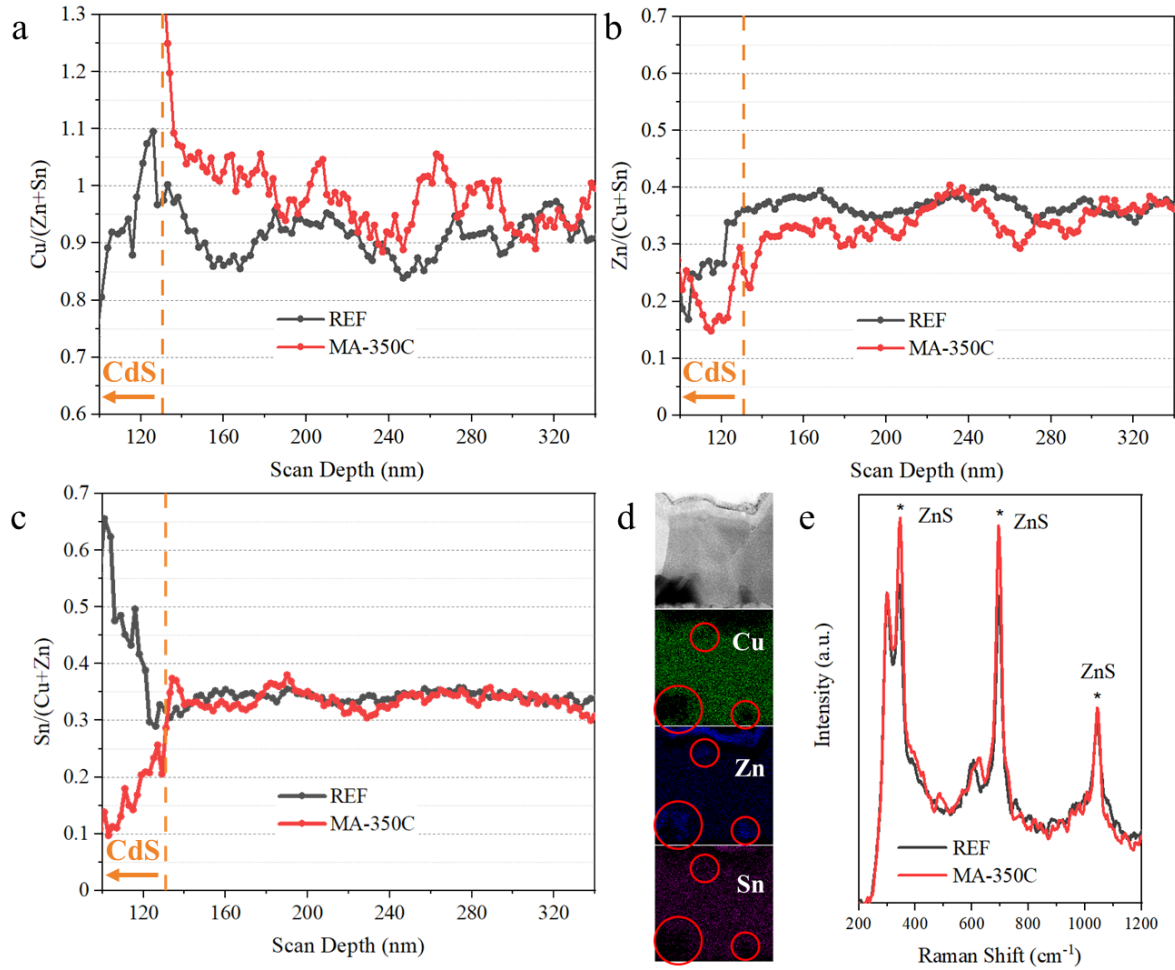


Figure 4.9 Cation ratios in REF and MA-350C derived from TEM EDS line scans shown in Figure 4.7a-b, respectively. a. Cu/(Zn+Sn). b. Zn/(Cu+Sn). c. Sn/(Cu+Zn). d. TEM-EDS maps showing the distributions of key CZTS constituent cations of MA-350C. e. Raman spectra with 325 nm excitation wavelength of REF and MA-350C. ZnS 1st, 2nd and 3rd order peaks are marked as “*”.

4.3.2 The Increased Disorder

The MAPDA treatment can yield more disordered CZTS because of the rapid cooling from 350 °C annealing temperature, which is higher than 260 °C – the critical temperature of post-annealing for order-disorder transitions³⁰. To verify this, near-resonant Raman scattering was performed with an excitation wavelength of 785 nm, on the as-grown CZTS films (REF), the

MAPDA-treated CZTS films w/o (MA-350C) and w/ CdS buffer layers (MA-350C-CdS). Four samples from each type were measured to ensure the result repeatability. The results were shown in Figure 4.10a. The ratio of peak intensity at 288 cm^{-1} to that at 304 cm^{-1} can be used as an indicator of ordering for ordered samples obtained from the controlled cooling at the end of the sulfurization process, while the dominance of peaks at 368 and 376 cm^{-1} compared with the main A mode peak at 339 cm^{-1} can be used for comparing the order-disorder for disordered samples^{30,31}. In general, CZTS is a disordered semiconductor without intentional control of cooling after the sulfurization process³⁰ or substitution of isovalent elements^{4,32}. REF demonstrates the typical Raman spectra of a CZTS film. The higher intensity ratios of peaks at 368 and 376 cm^{-1} to the main A mode peak for MAPDA-treated samples implies more significant disorder presents in these samples. A redshift (REF \rightarrow MA-350C) of the A mode peak, as shown in Figure 4.10b, can be regarded as another indicator for the increased disorder³³. Furthermore, as illustrated in Figure 4.10c, photoreflectance measurement shows lower E_g of MA-350C (1.53 eV, compared with 1.63 eV of REF). The reduction of E_g was (at least partially) induced by the increased disorder^{31,33-36}.

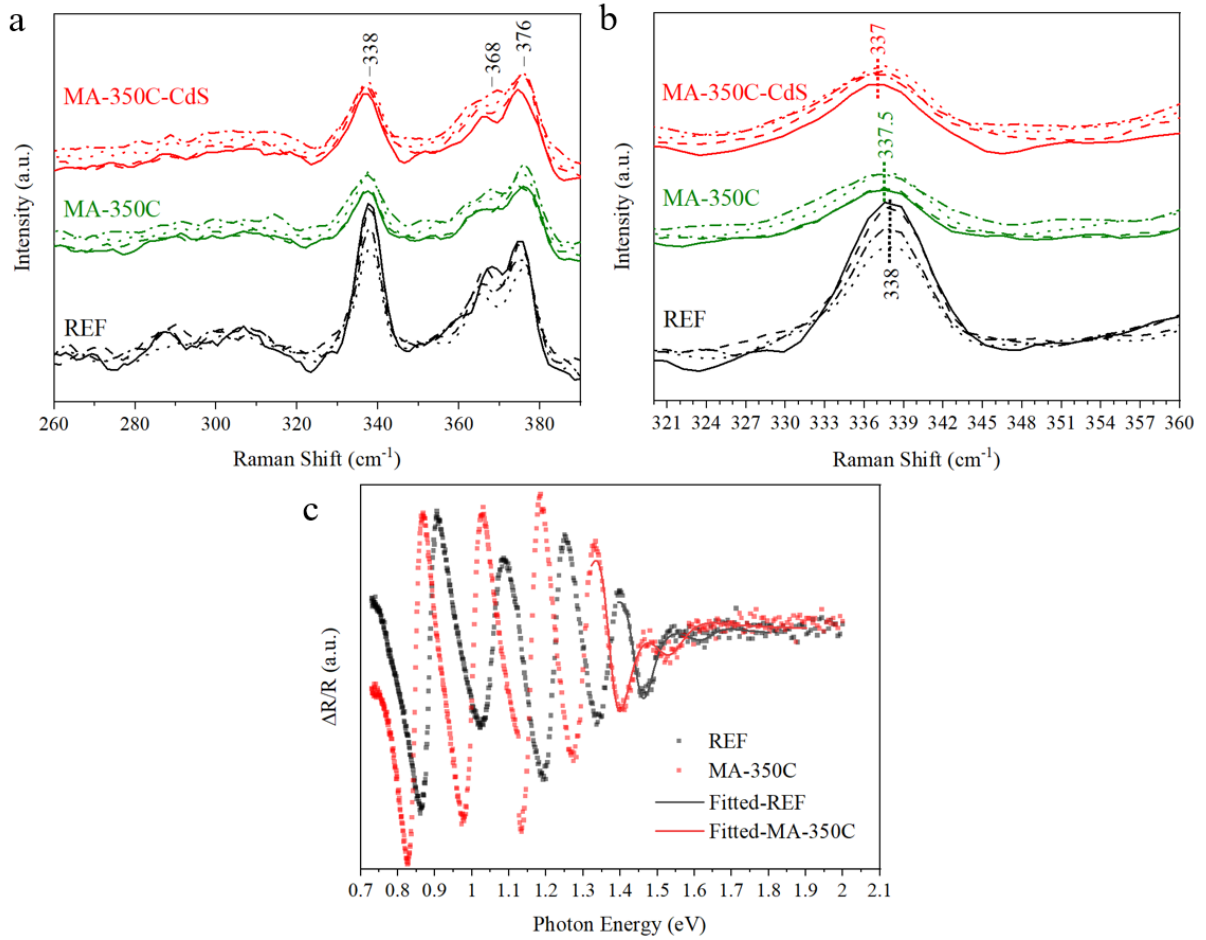


Figure 4.10 a. Raman spectra of the control bare CZTS (REF), MAPDA-treated CZTS samples without (MA-350C) and with (MA-350C-CdS) CdS buffer layer. B. Featured A mode peaks emphasizing the red shift. Four samples for each type were measured for ensuring the data repeatability. C. Photoreflectance measurements for the CdS-coated CZTS films.

4.3.3 Diffusion and Activation of Cd at Low Temperature

A further redshift of the A mode peak presented at the MAPDA-treated sample after the CdS deposition (MA-350C-CdS), as shown in Figure 4.10b, which is highly likely associated with the Cd incorporation into the CZTS lattice^{1,3,4}. Thermodynamically favoured Cd activation during the CBD process could be related to the loss of Na within CZTS. Based on the first-

principles calculations, the formation energy of Na_{Cu} neutral antisite through the substitution of Cu by Na is small and that through the migration of Na into Cu vacancies (V_{Cu}) is even smaller³⁷. Therefore, the removal of Na leaves V_{Cu} acceptors vacancy by vacancy throughout the entire CZTS films, especially near the GBs. The as-formed V_{Cu} is partially compensated by the occupancy of Cd at these defects to form Cd_{Cu} donors. The low formation energy of this antisite can be supported by the first-principles calculations³⁸ and negative formation energy was calculated for the formation of $[\text{Cd}_{\text{Cu}} + \text{V}_{\text{Cu}}]$ neutral cluster. The presence of Cd_{Cu} in the MAPDA-treated CZTS film can be seen from the filtered high-resolution high-angle annular dark field (HAADF) image, as shown in Figure 4.11a-c. Thus, the precondition of increased V_{Cu} concentration achieved by the MAPDA treatment is the prerequisite to facilitate much easier Cd diffusion and activation into the CZTS lattice.

High-resolution TEM was performed to investigate the role of Cd diffusion in the CZTS. Figure 4.11a shows the bright field TEM image of MA-350C. The top CZTS region adjacent to the CZTS/CdS heterointerface was scrutinized using a filtered high-resolution high-angle annular dark field (HAADF) image (Figure 4.11b). The contrast of the atomic matrix in this HAADF image depends on the mean square atomic number (Z^2) of the constituent elements along with the depth of this specimen (~ 100 nm)^{39,40}. The inset enlarged image shows a clear contrast from the different cation columns. Discussion about this approach in detail can be found in our previous publication³. Figure 4.11d shows the intensity profile of a row of cations along the [100] zone axis as enclosed by the red rectangle. The distinctively strong peak represents Sn which has a much larger atomic number than the other CZTS constituent elements. Three cation elements between two Sn ions are in the order of Zn, Cu and Cu considering the kesterite structure. The neighbouring Zn and Cu elements in the periodic table have adjacent atomic numbers, and thus the peak intensities of these ions are supposed

to be very similar. However, Z^2 along the atomic column could vary from column to column due to the presence of antisites and vacancies. It is obvious that two columns within the selected four unit-cells are much stronger than the other Cu/Zn sites. Although we cannot directly rule out the substitution of Cu by Sn, based on the first-principles calculations^{36,41}, the formation of Sn_{Cu} antisites is thermodynamically unfavourable. Considering the Cd alloying in the kesterite matrix as evidenced by the EDS and Raman characterizations, these large intensity spikes are highly likely ascribed to the formation of Cd_{Cu} which has relatively low formation energy³⁷. This result further supports that the Cd activation at the CZTS lattice can occur during the CBD process at such a low temperature at 70 °C.

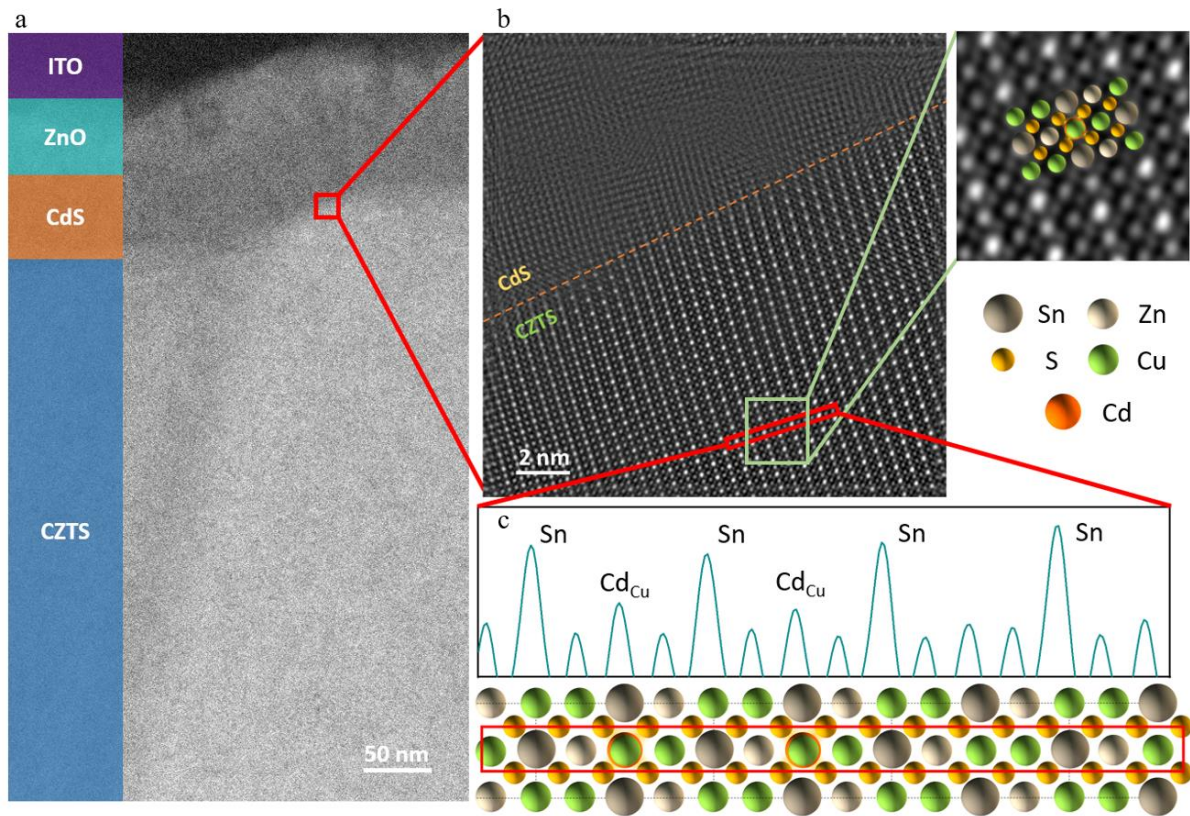


Figure 4.11 a. bright-field TEM image of cross-sectional CZTS device with MAPDA treatment, with the layer identification schema shown left. b. Filtered atomic resolution HAADF image taken at the region near the CdS/CZTS heterointerface. c. The intensity

profile in a row of cations marked by the red rectangle shows the cation exchange (Cd occupying Cu sites), referring to the kesterite structure which depicted in the bottom schema.

4.3.4 Defect Investigations

Na loss and ion exchange may result in the variation of defect type and energy level, which was investigated via admittance spectroscopy (AS). Figure 4.12a&b show the temperature-dependent admittance spectra of REF and MA-350C, and Figure 4.12 c presents the Arrhenius plots, from which the defect activation energy (E_a) and the attempt-to-escape frequency ν_0 of the defects can be obtained, according to the relation ⁴²:

$$\omega_0 = 2\nu_0 \exp\left(-\frac{E_a}{kT}\right) \quad 1$$

where k is the Boltzmann constant, and ω_0 is the inflection angular frequency of the electronic transition, determined by the maxima of fdC/df . At a certain temperature, specific defects can be charged or discharged only at a modulation frequency $\omega < \omega_0$. Otherwise, the carriers originated from the corresponding defects cannot follow the AC excitation, i.e. being dielectrically frozen out, and thereby reducing the junction capacity ^{42,43}. From the Arrhenius plots $-\ln(\omega_0/T^2)$ as a function of $1000/T$, E_a and ν_0 are derived from the slope of the linear fit (broken line) and the vertical-axis interception. After the acquirement of the built-in voltage V_{bi} and the depletion region width of the heterojunction W_d from capacitance-voltage ($C-V$) measurements, the defect energy distributions residing within the band gap were plotted in Figure 4.10d&e, based on the following equations ⁴²:

$$E(\omega) = kT \ln\left(\frac{2\nu_0}{\omega}\right) \quad 2$$

$$N_t(E(\omega)) = -\frac{V_{bi}}{qW_d} \cdot \frac{dC}{d\omega} \cdot \frac{\omega}{kT} \quad 3$$

where E is the defect energy with respect to the VBM.

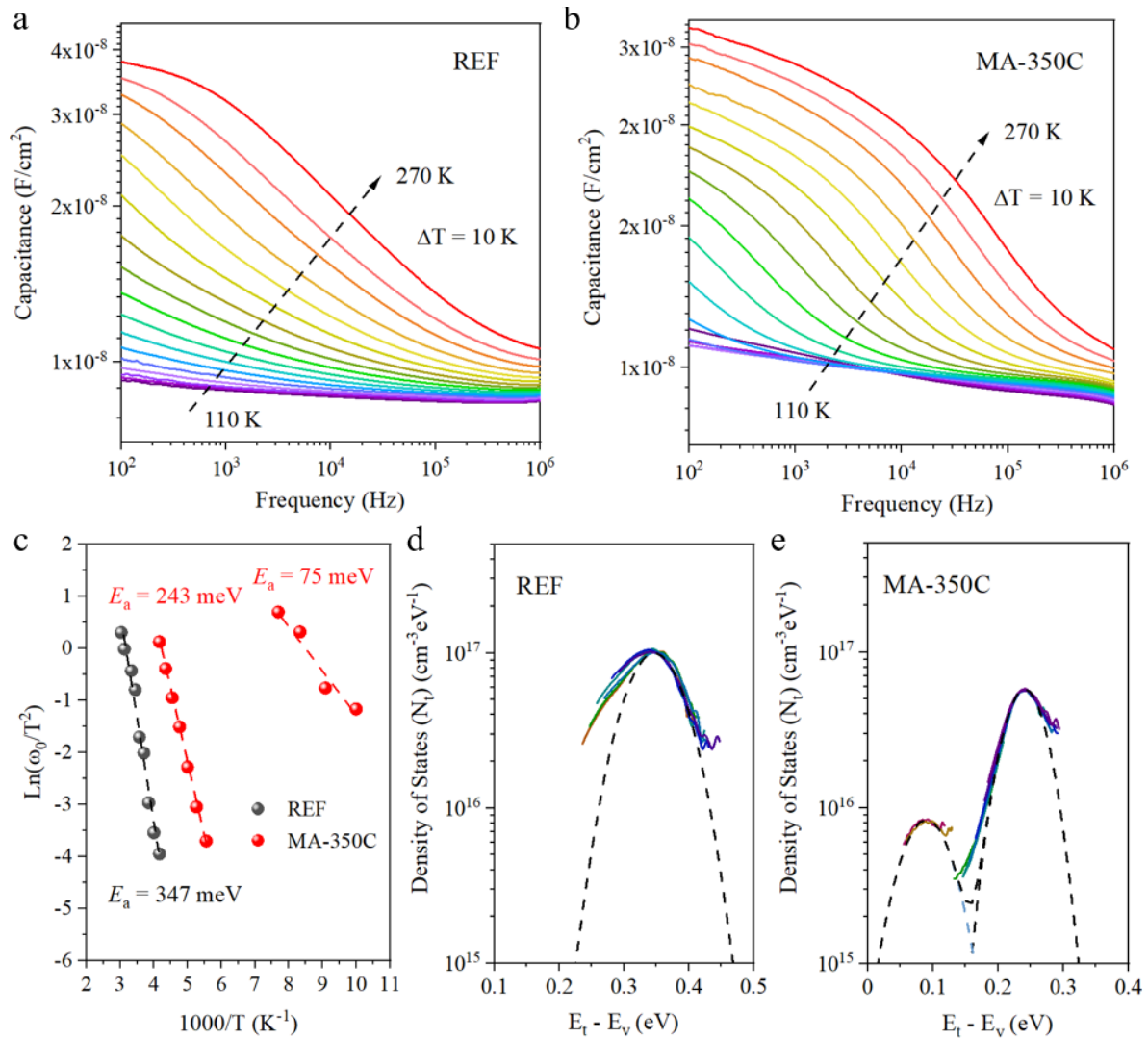


Figure 4.12 Defect study through admittance spectroscopy for REF and MA-350C. Admittance (C - f - T) spectra of a. REF & b. MA-350C. c. Arrhenius plots obtained from admittance spectra. Energy-resolved defect profiles of d. REF & e. MA-350C.

As shown in Figure 4.12 c, the defects residing REF with E_a of 347 meV and MA-350C with E_a of 243 meV are considered as different defects, possibly assigned to Zn_{Sn} and Cu_{Zn} , respectively^{36,41,44}. These antisites have relatively low formation energies^{36,41} and both are

considered as the major doping sources respectively for each sample. The shallower defects presented in MA-350C at 75 meV are considered as V_{Cu} ^{36,41}.

The actual mechanisms of Zn_{Sn} suppression and shallower Cu_{Zn} activation are still veiled, which require further in-depth investigations. Based on our experimental results and theoretical calculations reported elsewhere⁴⁵, the dominance of Cu_{Zn} may possibly stem from the removal of interstitial Na from $[Cu_{Zn} + Na_i]$ clusters, as well as the change of intrinsic element ratio due to the segregation of ZnS secondary phases as discussed in our TEM-EDS and Raman results (Figure 4.9). The latter may also determine deactivation of Zn_{Sn} antisites. In addition, high temperature post-deposition annealing cannot provide sufficient relaxation process for defect clusters with high formation energies, such as $[Zn_{Sn} + Sn_{Zn}]$ and $[Zn_{Sn} + 2Sn_{Cu}]$ ^{36,41}, which, in turn, compensates deep Zn_{Sn} acceptors and decreases E_g .

The activation of V_{Cu} is very likely ascribed to the Na loss because Na is thermodynamically favoured to accommodate Cu sites as charge-neutral Na_{Cu} antisites^{3,19,20}. According to the first-principles calculations, the formation energy of charge-neutral Na_{Cu} is much lower than that of V_{Cu} , Zn_{Cu} and Sn_{Cu} antisites⁴⁵ for Cu poor compositions used in this work, which normally yield the best device performance^{3,46-49}. However, the formation energy of a large population of V_{Cu} is high³⁶ and V_{Cu} is prone to be compensated by donor-like defects, such as Zn_{Cu} and Cd_{Cu} with relatively low formation energy, to form electrically benign neutral clusters ($[V_{Cu} + Zn_{Cu}]$ and $[V_{Cu} + Cd_{Cu}]$)^{36,38}. Compensation between V_{Cu} and these donor-like defects, in turn, gives rise to the low V_{Cu} density observed from Figure 12e. In addition, the emerging V_{Cu} may, in turn, explain the spontaneous low-temperature (70 °C) Cd diffusion and activation during the CdS deposition process, much lower than 200 °C which reported

insufficient for Cd diffusion ¹². As discussed hereinbefore, the presence of Cd in CZTS lattice was found as Cd_{Cu} antisites from the HAADF results. The formation energy significantly decreases when Cd_{Cu} couples with V_{Cu} (i.e., [V_{Cu} + Cd_{Cu}]) by theoretical calculations ³⁸. The incorporation of Cd into CZTS could be another benefit to alleviate the SRH recombination through optimizing the heterojunction band alignment and to suppress the band tailing issue ^{3,8,10,50}.

4.3.5 Modification in the CZTS/CdS Heterointerface

The defect modification via the MAPDA and the sequent CdS deposition was proved in the CZTS bulk in Section 4.3.4. But the elemental redistributions occurred more remarkably at the CZTS heterojunction and the CZTS GBs. The heterointerface improvement was investigated using *C-V* and drive-level capacitance profiling (DLCP) techniques. Compared to *C-V* measurement, DLCP characterization is primarily sensitive to the bulk states, which can give defect density with little interference by the presence of interface states ⁵². Therefore, the combined *C-V* and DLCP characterizations provide an estimation of the heterointerface defect states ⁵³. As shown in Figure 4.13 and Table 4.1, the significant reduction of the defect concentration (N_T) within the space charge region (SCR) after the MAPDA treatment is proved by the carrier concentration difference measured by *C-V* (N_{CV}) and DLCP (N_{DL}) under zero bias. The decrement of the heterointerface deep-level acceptor defects is over one order for MA-350C compared to REF. According to the AS results, these inhibited defects are suspected as Zn_{Sn} antisites.

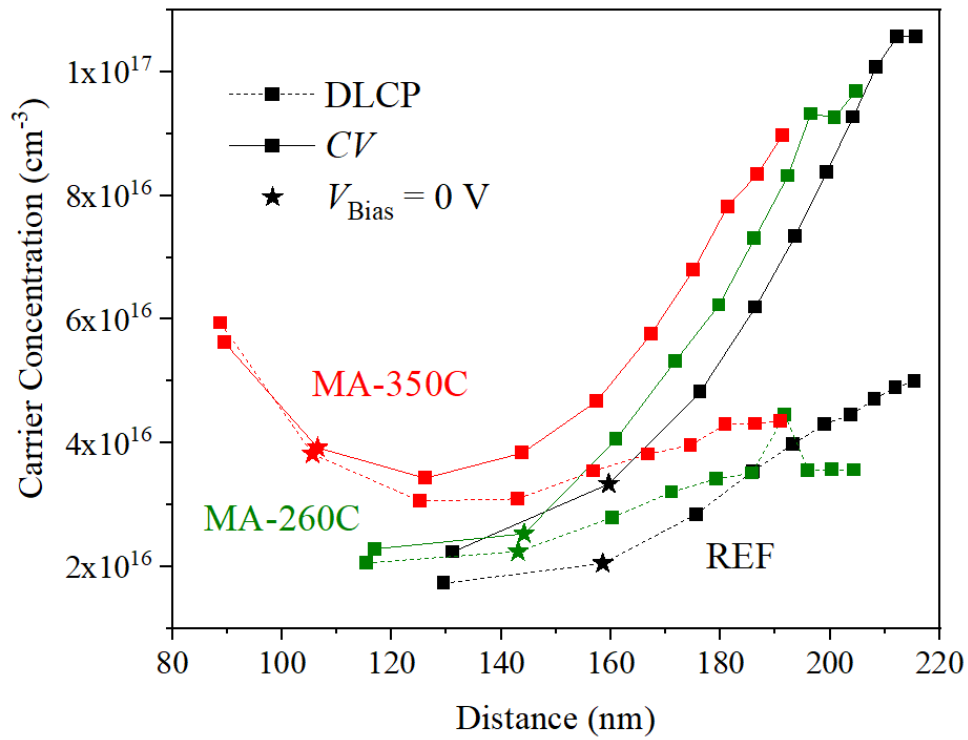


Figure 4.13 Carrier concentration profiles obtained by *C-V* (solid lines) and DLCP (broken lines) results of the same cells in Figure 4.3-4.7. The measurement was performed at 10 kHz from +0.2 to -1.6 V DC bias.

Table 4.1 Parameters of electrical properties obtained from *C-V* and DLCP measurements.

CZTS	W_d	N_{DL}	N_{CV}	N_T
Device	(nm)	(cm ⁻³)	(cm ⁻³)	(cm ⁻²)
REF	159	2.05×10^{16}	3.34×10^{16}	2.05×10^{11}
MA-260C	143	2.24×10^{16}	2.53×10^{16}	4.12×10^{10}
MA-350C	106	3.82×10^{16}	3.92×10^{16}	1.06×10^{10}

4.3.6 Improvement in Device Performance

Through the modification of the heterojunction by MAPDA, a significant improvement in device performance has been demonstrated. Figure 4.14a and Table 4.2 summarize the J - V characteristics of the CZTS solar cells w/ and w/o MAPDA at different temperature. With the aid of the MAPDA treatment at 350 °C, the Na-depleted and Cd-incorporated CZTS solar cell presented a significant improvement in efficiency from 7.50 % (REF) to 8.67 % (MA-350C). MA-260C shares a similar trend in performance improvement, but the extent is not as remarkable as that of MA-350C, which is reasonable due to relatively weaker reduction in heterointerface defect density. The boost of efficiency is mainly contributed by the improvement of J_{SC} and FF, albeit a slight drop in V_{OC} results from the decreased E_g in the treated devices. Apart from the photoreflectance results discussed hereinbefore, the reduction in the CZTS E_g can also be noticed from the redshift of EQE curve tails. This section of EQE data was used for fitting the plot of $[E_{ph}\ln(1-EQE)]^2$ vs E_{ph} (photon energy) to determine the E_g of the CZTS films⁵⁴, as shown in the inset of Figure 4.14b. The E_g values were displayed in Table 4.2. The overall effect of a slight drop of V_{OC} and more remarkable decrease in E_g give a result in the reduction of V_{OC} deficit with the increased MAPDA temperature, as shown in Table 4.2.

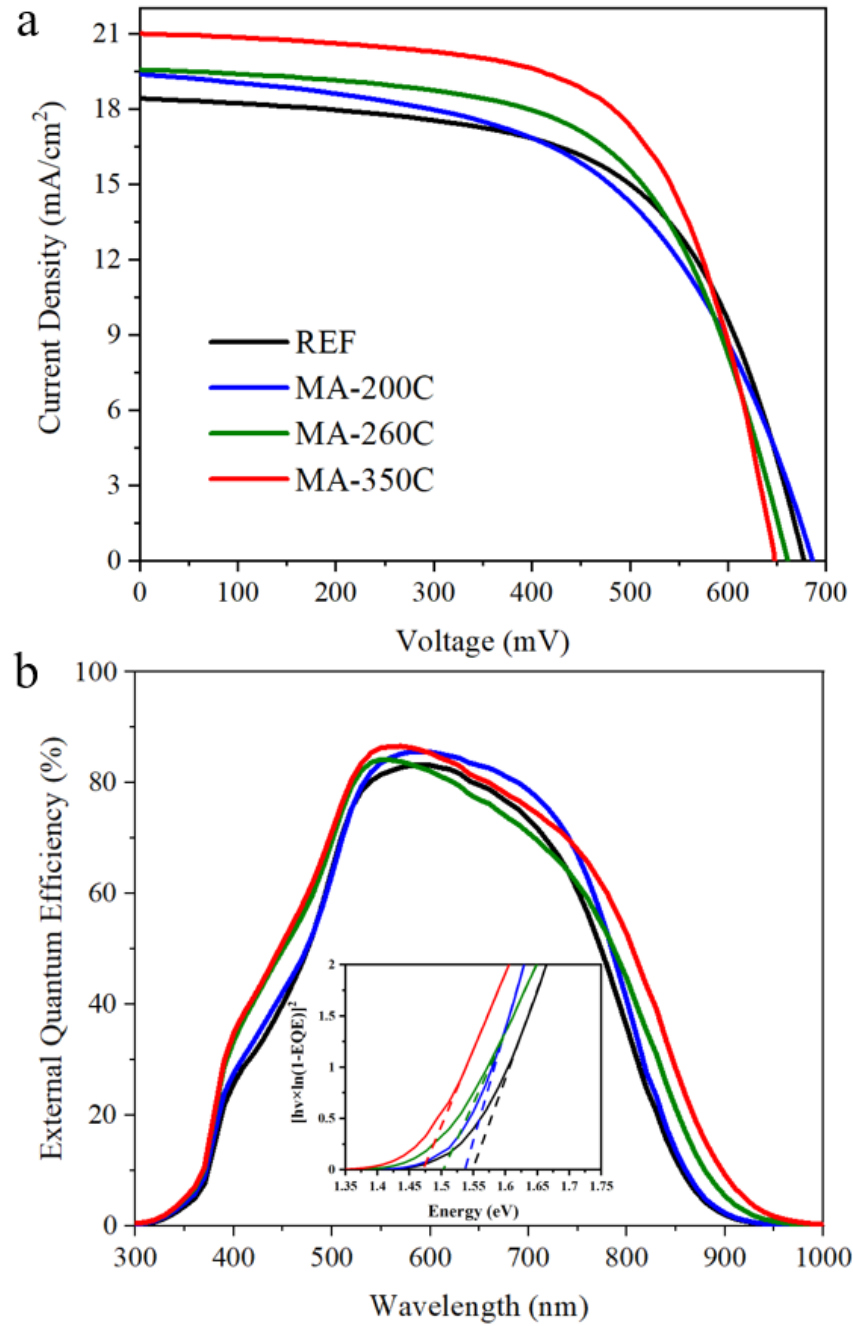


Figure 4.14 a. *J-V* characteristics of CZTS solar cells w/ and w/o MAPDA treatment at different temperature. b. EQE spectra of these same cells. The inset image shows the $[h\nu \times \ln(1-EQE)]^2$ plots to determine the band gaps of CZTS absorbers.

As the EQE spectra demonstrated, the enhancement of collection efficiency contributes to the improvement in short-wavelength response, CZTS-absorption spectra response at the surface

and long-wavelength response. The mechanisms of the improvement in short-wavelength response will be discussed in Chapter 5 and 6. The increase of photocarriers collection efficiency at the CZTS surface is induced by the mitigation of non-radiative recombination within the SCR and particularly at the heterointerface with significantly reduced defect density. However, the shrink of depletion width has a negative impact on charge collection at relatively deeper bulk of CZTS, showing weaker improvement of optical response from 620 to 710 nm.

Table 4.2 Detailed device performance parameters and band gaps of CZTS absorbers w/ and w/o MAPDA treatment at different temperature.

CZTS	Eff	V_{OC}	J_{SC}	FF	E_g	V_{OC} Deficit
Device	(%)	(mV)	(mA/cm ²)	(%)	(eV)	(mV)
REF	7.50	677	18.4	60.2	1.55	872
MA-200C	7.20	686	19.4	54.1	1.54	850
MA-260C	7.87	662	19.6	60.8	1.50	841
MA-350C	8.67	646	21.0	63.9	1.47	825

By fitting the curves using a single diode model, as displayed in Table 4.3, the drop of ideality factor (A , from 3.02 to 2.23) and dark saturation current density (J_0 , from 2.92×10^{-6} A·cm⁻² to 2.63×10^{-7} A·cm⁻², respectively for REF and MA-350C), suggests that the decrease of V_{OC} deficit is attributed to the mitigation of non-radiative recombination within the SCR, which correlates with the reduction of the defect density at the CZTS/CdS heterointerface.

Table 4.3 Detailed device performance parameters estimated using a one-diode model.

CZTS	V_{OC} Deficit	R_s	R_{SH}	A	J_0
Device	(mV)	($\Omega \cdot \text{cm}^2$)	($\Omega \cdot \text{cm}^2$)		(mA/cm^2)
REF	872	1.52	462	3.02	2.92×10^{-6}
MA-200C	850	2.65	319	3.65	1.21×10^{-5}
MA-260C	841	2.73	472	2.53	7.50×10^{-7}
MA-350C	825	1.76	477	2.23	2.63×10^{-7}

In terms of the disordering impacts on device performance, Stéphane Bourdais et al. reported the more disordered sample with smaller E_g improves J_{SC} by $\sim 1.8 \text{ mA}/\text{cm}^2$ while reducing V_{OC} by $\sim 38 \text{ mV}$ on average of one batch samples of CZTSSe solar cells (as well as a slight increase of FF), achieved by controlling the cooling rate⁵⁵. However, the improvement of J_{SC} is limited, and the V_{OC} deficit is unchanged. Therefore, in this work, the device performance results via MAPDA are not merely stemmed from the change of the order-disorder. Instead, heterojunction modification is one of the main reasons contributing to the improvements.

4.4 Summary

In this chapter, we developed moisture-assisted post-deposition annealing (MAPDA) as a novel post-deposition treatment to achieve defect control through the element interdiffusion. The loss of Na facilitates the spontaneous Cd diffusion and activation during the CdS CBD process at 70°C and stimulates the out-diffusion of Cu towards the CZTS GBs, surface and the CdS layer. Meanwhile, the precipitation of ZnS secondary phases at the bottom of the

CZTS layer leads to the increase of Cu/Zn ratio especially at the CZTS surface and GBs where Cu is richer. The overall element redistribution induces the generation of V_{Cu} , activation of Cd, suppression of deep acceptor Zn_{Sn} and the increase of the density of shallower acceptor, contributing to the improvement of device performance, especially at the heterojunction region. This work is of significance in giving a new viewpoint to fabricate efficient kesterite solar cells through a novel defect engineering model, and in facilitating the diffusion of more desirable extrinsic elements through removing excessive Na, which may also be beneficial for a wider range of Na-containing thin film semiconductors. The detrimental role of excessive Na will be unveiled in Chapter 6 using nanoscale optoelectronic characterizations.

4.5 Reference

- 1 Su, Z. *et al.* Cation substitution of solution-processed Cu_2ZnSnS_4 thin film solar cell with over 9% efficiency. *Advanced Energy Materials* **5**, 1500682 (2015).
- 2 Romanyuk, Y. E. *et al.* Doping and alloying of kesterites. *Journal of Physics: Energy* **1**, 044004 (2019).
- 3 Yan, C. *et al.* Cu_2ZnSnS_4 solar cells with over 10% power conversion efficiency enabled by heterojunction heat treatment. *Nature Energy* **3**, 764-772 (2018).
- 4 Yan, C. *et al.* Beyond 11% Efficient Sulfide Kesterite $Cu_2Zn_xCd_{1-x}SnS_4$ Solar Cell: Effects of Cadmium Alloying. *ACS Energy Letters* **2**, 930-936 (2017).
- 5 Ben Messaoud, K. *et al.* Impact of the Cd^{2+} treatment on the electrical properties of $Cu_2ZnSnSe_4$ and $Cu(In, Ga)Se_2$ solar cells. *Progress in Photovoltaics: Research and Applications* **23**, 1608-1620 (2015).

- 6 Sun, K. *et al.* Minority lifetime and efficiency improvement for CZTS solar cells via Cd ion soaking and post treatment. *Journal of Alloys and Compounds* **750**, 328-332 (2018).
- 7 Liu, F. *et al.* Nanoscale microstructure and chemistry of Cu₂ZnSnS₄/CdS interface in kesterite Cu₂ZnSnS₄ solar cells. *Advanced Energy Materials* **6**, 1600706 (2016).
- 8 Tajima, S., Umehara, M. & Mise, T. Photovoltaic properties of Cu₂ZnSnS₄ cells fabricated using ZnSnO and ZnSnO/CdS buffer layers. *Japanese Journal of Applied Physics* **55**, 112302 (2016).
- 9 Hwang, S. K. *et al.* Improved interfacial properties of electrodeposited Cu₂ZnSn (S, Se) 4 thin-film solar cells by a facile post-heat treatment process. *Progress in Photovoltaics: Research and Applications* **28** (2020).
- 10 Li, J., Wang, D., Li, X., Zeng, Y. & Zhang, Y. Cation Substitution in Earth-Abundant Kesterite Photovoltaic Materials. *Advanced Science* **5**, 1700744 (2018).
- 11 Chen, S., Gong, X., Walsh, A. & Wei, S.-H. J. P. R. B. Electronic structure and stability of quaternary chalcogenide semiconductors derived from cation cross-substitution of II-VI and I-III-VI₂ compounds. **79**, 165211 (2009).
- 12 Tajima, S. *et al.* Atom-probe tomographic study of interfaces of Cu₂ZnSnS₄ photovoltaic cells. *Applied Physics Letters* **105**, 093901 (2014).
- 13 Prabhakar, T. & Jampana, N. Effect of sodium diffusion on the structural and electrical properties of Cu₂ZnSnS₄ thin films. *Solar Energy Materials and Solar Cells* **95**, 1001-1004 (2011).
- 14 Yuan, Z. K. *et al.* Na-diffusion enhanced p-type conductivity in Cu (In, Ga) Se₂: A new mechanism for efficient doping in semiconductors. *Advanced Energy Materials* **6**, 1601191 (2016).

- 15 Nagaoka, A. *et al.* Effects of sodium on electrical properties in Cu₂ZnSnS₄ single crystal. *Applied Physics Letters* **104**, 152101 (2014).
- 16 Huang, W.-C., Wei, S.-Y., Cai, C.-H., Ho, W.-H. & Lai, C.-H. The role of Ag in aqueous solution processed (Ag, Cu) ₂ ZnSn (S, Se) ₄ kesterite solar cells: antisite defect elimination and importance of Na passivation. *Journal of Materials Chemistry A* **6**, 15170-15181 (2018).
- 17 Gershon, T. *et al.* The role of sodium as a surfactant and suppressor of non-radiative recombination at internal surfaces in Cu₂ZnSnS₄. *Advanced Energy Materials* **5**, 1400849 (2015).
- 18 Liu, C. Y. *et al.* Sodium Passivation of the Grain Boundaries in CuInSe₂ and Cu₂ZnSnS₄ for High-Efficiency Solar Cells. *Advanced Energy Materials* **7**, 1601457 (2017).
- 19 Schwarz, T. *et al.* Atom probe tomography study of internal interfaces in Cu₂ZnSnSe₄ thin-films. *Journal of Applied Physics* **118**, 095302 (2015).
- 20 Tajima, S. *et al.* Sodium distribution in solar-grade Cu₂ZnSnS₄ layers using atom-probe tomographic technique. *Japanese Journal of Applied Physics* **54**, 112302 (2015).
- 21 Wilson, R. G., Stevie, F. A. & Magee, C. W. Secondary ion mass spectrometry: a practical handbook for depth profiling and bulk impurity analysis. *Wiley-Interscience* (1989).
- 22 Aberth, W., Straub, K. M. & Burlingame, A. Secondary ion mass spectrometry with cesium ion primary beam and liquid target matrix for analysis of bioorganic compounds. *Analytical Chemistry* **54**, 2029-2034 (1982).
- 23 Gnaser, H. & Oechsner, H. SIMS depth profile analysis using MCs⁺ molecular ions. *Fresenius' journal of analytical chemistry* **341**, 54-56 (1991).

- 24 Grini, S. *et al.* Dynamic Impurity Redistributions in Kesterite Absorbers. *Physica Status Solidi (b)* **257**, 2000062 (2020).
- 25 Xie, H. *et al.* Impact of Na dynamics at the Cu₂ZnSn (S, Se) 4/CdS interface during post low temperature treatment of absorbers. *ACS applied materials & interfaces* **8**, 5017-5024 (2016).
- 26 Cui, X. *et al.* Enhanced Heterojunction Interface Quality To Achieve 9.3% Efficient Cd-Free Cu₂ZnSnS₄ Solar Cells Using Atomic Layer Deposition ZnSnO Buffer Layer. *Chemistry of Materials* **30**, 7860-7871 (2018).
- 27 Haight, R., Shao, X., Wang, W. & Mitzi, D. B. Electronic and elemental properties of the Cu₂ZnSn (S, Se) 4 surface and grain boundaries. *Applied Physics Letters* **104**, 033902 (2014).
- 28 Kohl, T. *et al.* About the Inclusion of Water in Cu (In, Ga) Se₂ Absorber Material During Accelerated Lifetime Testing. *ACS Applied Energy Materials* **3**, 5120-5125 (2020).
- 29 Ren, Y., Scragg, J. J., Edoff, M., Larsen, J. K. & Platzer-Björkman, C. Evolution of Na–S (–O) Compounds on the Cu₂ZnSnS₄ Absorber Surface and Their Effects on CdS Thin Film Growth. *ACS applied materials & interfaces* **8**, 18600-18607 (2016).
- 30 Scragg, J. J., Choubrac, L., Lafond, A., Ericson, T. & Platzer-Björkman, C. A low-temperature order-disorder transition in Cu₂ZnSnS₄ thin films. *Applied Physics Letters* **104**, 041911 (2014).
- 31 Scragg, J. J. *et al.* Cu–Zn disorder and band gap fluctuations in Cu₂ZnSn (S, Se) 4: Theoretical and experimental investigations. *physica status solidi (b)* **253**, 247-254 (2016).
- 32 Gershon, T. *et al.* Photovoltaic device with over 5% efficiency based on an n-type Ag₂ZnSnSe₄ absorber. *Advanced Energy Materials* **6**, 1601182 (2016).

- 33 Rey, G. *et al.* The band gap of Cu₂ZnSnSe₄: Effect of order-disorder. *Applied Physics Letters* **105**, 112106 (2014).
- 34 Malerba, C., Valentini, M. & Mittiga, A. Cation Disorder In Cu₂ZnSnS₄ Thin Films: Effect On Solar Cell Performances. *Solar RRL* **1**, 1700101 (2017).
- 35 Krämmer, C. *et al.* Reversible order-disorder related band gap changes in Cu₂ZnSn (S, Se) ₄ via post-annealing of solar cells measured by electroreflectance. *Applied Physics Letters* **105**, 262104 (2014).
- 36 Chen, S., Walsh, A., Gong, X. G. & Wei, S. H. Classification of lattice defects in the kesterite Cu₂ZnSnS₄ and Cu₂ZnSnSe₄ earth-abundant solar cell absorbers. *Advanced Materials* **25**, 1522-1539 (2013).
- 37 Maeda, T., Kawabata, A. & Wada, T. First-principles study on alkali-metal effect of Li, Na, and K in Cu₂ZnSnS₄ and Cu₂ZnSnSe₄. *physica status solidi (c)* **12**, 631-637 (2015).
- 38 Maeda, T., Nakamura, S. & Wada, T. First-principles study on Cd doping in Cu₂ZnSnS₄ and Cu₂ZnSnSe₄. *Japanese Journal of Applied Physics* **51**, 10NC11 (2012).
- 39 Nellist, P. & Pennycook, S. Incoherent imaging using dynamically scattered coherent electrons. *Ultramicroscopy* **78**, 111-124 (1999).
- 40 Rafferty, B., Nellist, D. & Pennycook, J. On the origin of transverse incoherence in Z-contrast STEM. *Microscopy* **50**, 227-233 (2001).
- 41 Chen, S., Yang, J.-H., Gong, X.-G., Walsh, A. & Wei, S.-H. Intrinsic point defects and complexes in the quaternary kesterite semiconductor Cu₂ZnSnS₄. *Physical Review B* **81**, 245204 (2010).

- 42 Walter, T., Herberholz, R., Müller, C. & Schock, H. Determination of defect distributions from admittance measurements and application to Cu (In, Ga) Se₂ based heterojunctions. *Journal of Applied Physics* **80**, 4411-4420 (1996).
- 43 Gunawan, O. *et al.* Electronic properties of the Cu₂ZnSn (Se, S) 4 absorber layer in solar cells as revealed by admittance spectroscopy and related methods. *Applied Physics Letters* **100**, 253905 (2012).
- 44 Chen, S., Gong, X., Walsh, A. & Wei, S.-H. Defect physics of the kesterite thin-film solar cell absorber Cu₂ZnSnS₄. *Applied Physics Letters* **96**, 021902 (2010).
- 45 Tse, K. *et al.* Defect properties of Na and K in Cu₂ZnSnS₄ from hybrid functional calculation. *Journal of Applied Physics* **124**, 165701 (2018).
- 46 Wang, W. *et al.* Device characteristics of CZTSSe thin-film solar cells with 12.6% efficiency. *Advanced Energy Materials* **4**, 1301465 (2014).
- 47 Son, D.-H. *et al.* Effect of solid-H₂S gas reactions on CZTSSe thin film growth and photovoltaic properties of a 12.62% efficiency device. *Journal of Materials Chemistry A* **7**, 25279-25289 (2019).
- 48 Li, J. *et al.* Tailoring the defects and carrier density for beyond 10% efficient CZTSe thin film solar cells. **159**, 447-455 (2017).
- 49 Cui, X. *et al.* Cd-Free Cu₂ZnSnS₄ solar cell with an efficiency greater than 10% enabled by Al₂O₃ passivation layers. *Energy & Environmental Science* **12**, 2751-2764 (2019).
- 50 Chen, S., Gong, X., Walsh, A. & Wei, S.-H. J. P. R. B. Electronic structure and stability of quaternary chalcogenide semiconductors derived from cation cross-substitution of II-VI and I-III-VI₂ compounds. *Physical Review B* **79**, 165211 (2009).

- 51 Neuschitzer, M. *et al.* Complex surface chemistry of kesterites: Cu/Zn reordering after low temperature postdeposition annealing and its role in high performance devices. *Chemistry of Materials* **27**, 5279-5287 (2015).
- 52 Heath, J. T., Cohen, J. D. & Shafarman, W. N. Bulk and metastable defects in CuIn_{1-x}Ga_xSe₂ thin films using drive-level capacitance profiling. *Journal of Applied Physics* **95**, 1000-1010 (2004).
- 53 Yin, L. *et al.* Limitation factors for the performance of kesterite Cu₂ZnSnS₄ thin film solar cells studied by defect characterization. *Rsc Advances* **5**, 40369-40374 (2015).
- 54 Scragg, J. J., Dale, P. J. & Peter, L. M. Towards sustainable materials for solar energy conversion: Preparation and photoelectrochemical characterization of Cu₂ZnSnS₄. *Electrochemistry Communications* **10**, 639-642 (2008).
- 55 Bourdais, S. *et al.* Is the Cu/Zn disorder the main culprit for the voltage deficit in kesterite solar cells? *Advanced Energy Materials* **6**, 1502276 (2016).

Chapter 5

Efficient CZTS Solar Cells with Significant Optimization of Heterojunction by Combined Post Annealing: Moisture-Assisted Post-Deposition Annealing and Heterojunction Annealing

5.1 Introduction

In Chapter 4, moisture-assisted post-deposition annealing (MAPDA) was introduced as a novel post-annealing treatment for improving the properties of CZTS and the heterojunction. The overall device performance is improved through manipulating the distribution of Na and Cd via MAPDA treatment. In this chapter, a follow-up heterojunction annealing (HJA) was adopted combined with the MAPDA process to further boost the device performance.

HJA is recognized as a compelling method for modifying the CdS/CZTS heterojunction through various optimization mechanisms. Elemental interdiffusion¹ at the heterojunction contributes to the mitigation of SRH recombination through optimization in local band alignment^{2,3}. As discussed in Chapter 2, sulfide CZTS has a cliff-like conduction band offset at the heterointerface with the CdS buffer, which aggravates the SRH recombination at the defective heterointerface⁴⁻⁶. Upon HJA, Zn diffusion from CZTS into the CdS layer as $\text{Zn}_{1-x}\text{Cd}_x\text{S}$ can elevate CdS conduction band minimum with higher Zn incorporation⁷. Meanwhile, the diffusion of Cd into the CZTS surface can result in a compensation of hole carrier concentration and enhance the downward band bending at the CZTS near-surface region², further optimizing the conduction band alignment at the heterojunction. Furthermore, the expansion of the Cu-poor/Zn-rich phase was observed^{8,9} through HJA which can suppress

the Fermi level pinning by reducing deep acceptor-like defects at the CZTS surface ^{10,11}. This could be important for the MAPDA-treated sample which has a high Cu/(Zn + Sn) ratio at the CZTS surface. Recrystallization of CdS ^{9,12} would be another benefit of HJA ⁹, however, CdS layers are generally regarded as a dead layer where low- τ photocarriers generated in this layer cannot be effectively collected due to the high defect density ^{13,14}. Moreover, it can be very important for the Na-depleted samples by MAPDA that HJA can accumulate favourable Na within the heterojunction region ³. CdS annealing at high temperature (beyond 300 °C) in the air would be advantageous in forming high conductivity CdSO₄ phases at the CdS surface for charge transport ¹⁵⁻¹⁹, but a problem would have arisen from the precipitation of ZnS phases at the heterointerface region at a lower temperature (~300 °C) ¹.

Herein, HJA was conducted in the ambient air with the optimal MAPDA treatment recipe (350 °C at saturated N₂ atmosphere) which yields the best device performance and the lowest Na concentration. This chapter displays manipulation of the critical trace elements, Na and Cd, and demonstrates significant improvement of device performance using the combined post-annealing treatments. Suns-V_{OC} measurement determines the significant mitigation of SRH recombination at the heterojunction. Furthermore, the change of CdS due to the elemental interdiffusion was also investigated.

5.2 Experiment

The HJA treatment was added after the CdS deposition process with or without the MAPDA process, as shown in Figure 5.1a-c. The optimal recipes (350 °C for 5 min) of the MAPDA process were used in this chapter producing the least alkali metal density and the best device performance. 8-min MAPDA process was also employed which could suggest an increased

alkali metal depletion. Here, we denote the control, 5-min and 8-min MAPDA treatments as MA0, MA5 and MA8. The HJA treatment was performed on a hot plate in the ambient air atmosphere with a substrate annealing temperature at 150 °C or 260 °C for 10 min (marked as MA0/5/8-150C or MA0/5/8-260C, respectively). The use of two HJA annealing temperatures aims to obtain different elemental distributions. The temperature of 260 °C was chosen in this work because it is considered as the critical temperature of the order-disorder transition ²⁰, and close the optimal HJA temperature in N₂ ¹ used in the record CZTS devices ³. The details of fabrication and characterization methods were presented in Chapter 2 (Section 2.4) and Chapter 4, respectively.

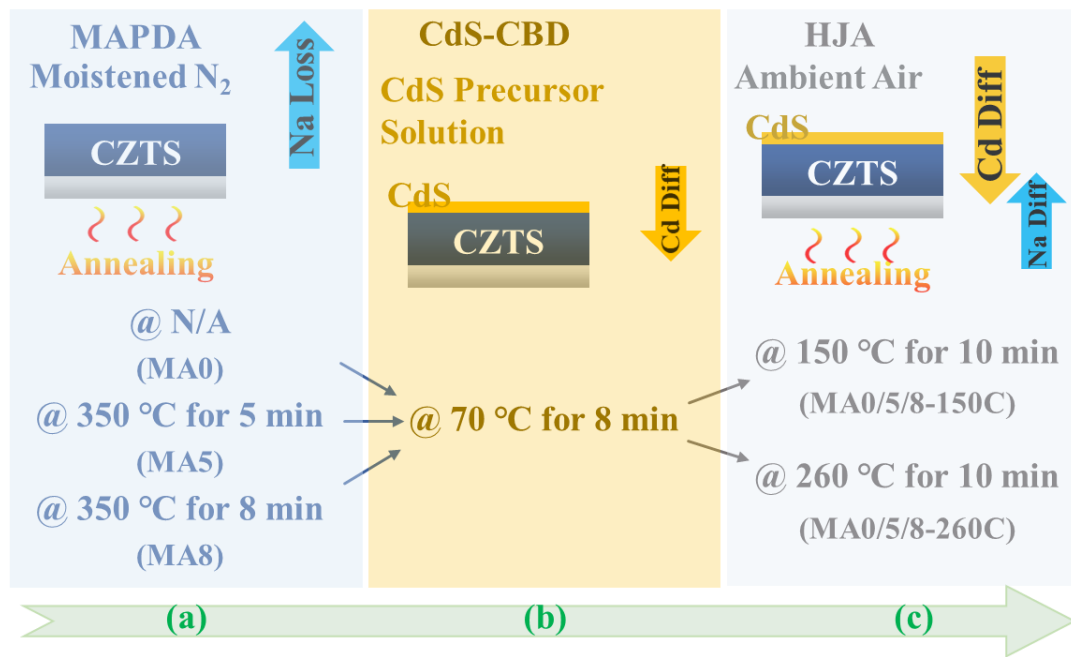


Figure 5.1 The flow of experiment processes of post-annealing before and after the CdS deposition with sample denotations a. moisture-assisted post-deposition annealing (MAPDA) process; b. CdS chemical bath deposition (CBD) process; c. heterojunction air annealing process. It is noted that Na loss actually happens in process b, however, it can occur by

dipping in just hot ammonia or deionized water. The main contribution of Na loss is the MAPDA process, as discussed in Chapter 4.

5.3 Results and Discussion

5.3.1 Further Modification of Elemental Distributions

The supplementary diffusion of alkali metals after HJA was observed from the ToF-SIMS results, as shown in Figure 5.2a-d. The distinct alkali metal peaks present within the CdS layers (Figure 5.2c&d) of MA5-150C and MA5-260C give big contrast to the absence of that in the MAPDA-only device in Figure 4.3e in Chapter 4. Although the Na concentration partially recovered, it is still much lower than those within the MAPDA-absent devices (MA0-150C and MA0-260C). Relative to the HJA-devices at 150 °C, those at 260 °C show higher Na concentrations at the front region of the CZTS layer and within the CdS layer. Furthermore, a considerably higher concentration of K accumulated within the CdS layer and the CZTS surface region of MA5-150C. It may occur through the occupancy of K over the vacancies that remained after the substantial Na loss and not yet completely occupied by Cd and Cu ions. Besides, such a low temperature is insufficient to drive more Na from the MoS₂ layers into the CZTS films. The improved K diffusion upon the Na-depleted heterojunction provides another example apart from Cd that extrinsic diffusion of some critical elements is inhibited by the dwelling of the excess Na ions. The MAPDA technology provides a solution to remove the excessive Na and thus promotes extrinsic diffusion.

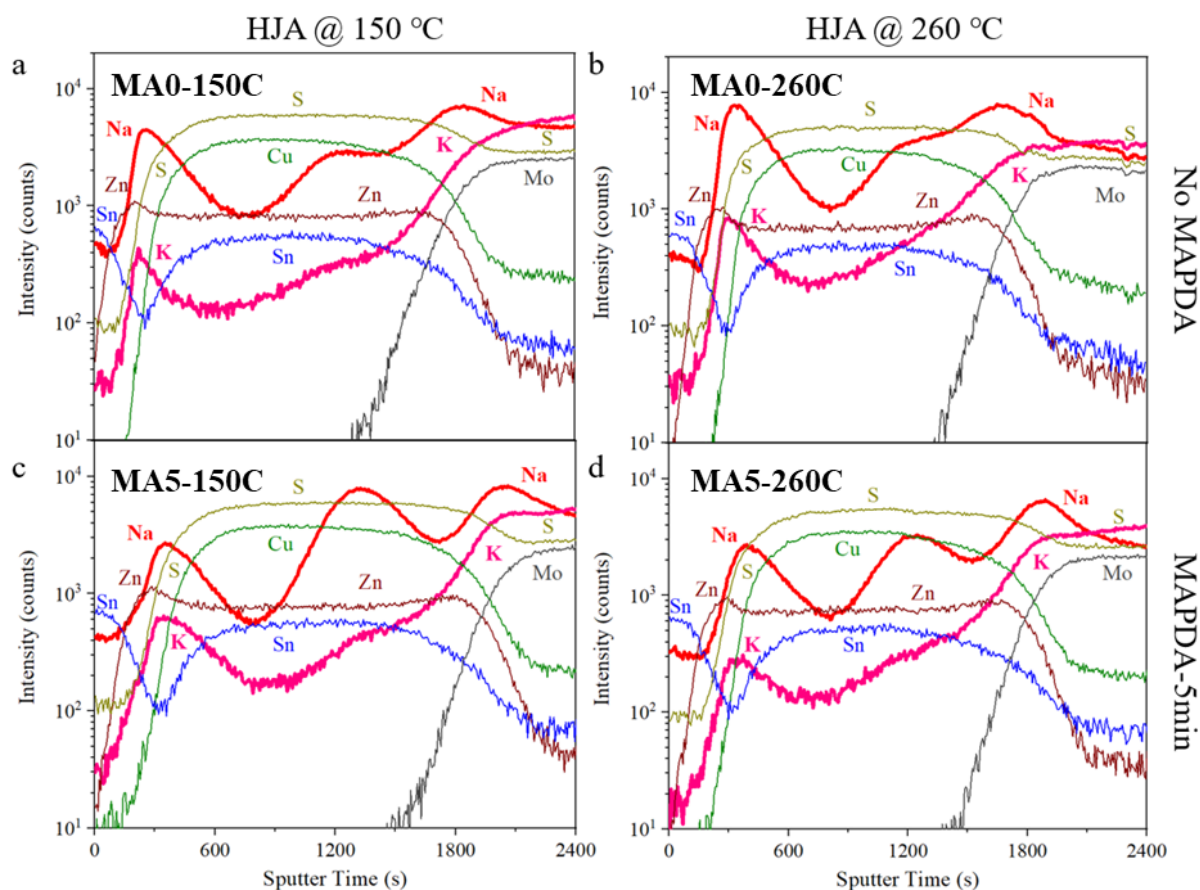


Figure 5.2 ToF-SIMS depth profiles scanned from the bottom of ITO layers until the surface of MoS₂ layers of the devices without MAPDA but with HJA at a. 150 °C (MA0-150C) and b. 260 °C (MA0-260C), as well as MAPDA-treated devices with HJA at c. 150 °C (MA5-150C) and d. 260 °C (MA5-260C).

This supplementary HJA also effectively strengthens Cd diffusion into the CZTS grain boundaries (GBs) and the grain interiors (GIs). A marked accumulation of Cd with the atomic fraction approximately 3 % was detected at the GB after the combined treatment with HJA at 260 °C, as shown in Figure 5.3c. However, the presence of strong Cd signals at the rear region gives us a concern that the aggregation of intensive Cd ions at the bottom, especially in the CdS phase, may yield a harmful reverse junction, hindering the local charge separation.

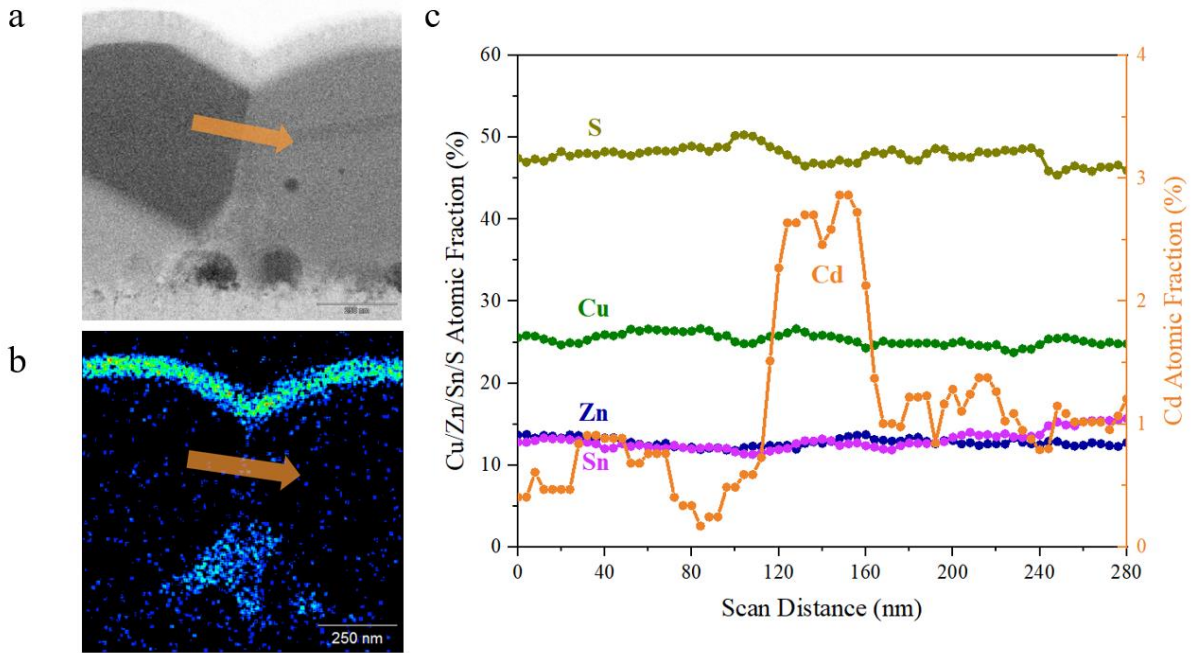


Figure 5.3 TEM image and EDS results for the device with combined 5-min MAPDA and HJA treatments. Arrows indicate the direction of a line scan across a grain boundary. a. TEM image; b. EDS map of Cd; c. line scan profiles across the grain boundary.

5.3.2 Further Improvement in Device Performance

The further optimization of elemental redistributions yielded a significant leap of PCE to 9.40 % by the combined treatments with the lower HJA temperature (MA8-150C), surpassing that using the same HJA conditions but without MAPDA treatment (MA0-150C, 7.88%), as displayed in Table 5.1 and Figure 5.4. Relative to MA8-150C, MA5-150C shows a similar trend but less improvement of device performance parameters. Being the optimal temperature¹ used in the record CZTS cell³ for HJA in the N₂ atmosphere, MA0-260C has a significantly higher efficiency (8.82%) than MA0-150C. However, the improvement is still no match with the MAPDA-treated devices with a lower HJA annealing temperature (i.e., MA8-150C). The combined treatments of MAPDA and HJA at 260 °C (MA5/8-260C) give rise to the

degradation in FF, especially for the device with a longer MAPDA duration (MA8-260C), albeit a champion V_{OC} was acquired. The trends in the best cells of these devices coincide with those in average of all fourteen cells on each device, statistically, as seen in Figure 5.5. MA5-150C and MA8-150C have average efficiencies of ~8.8% and ~9.0%, respectively.

Table 5.1 Device performance parameters for the same cells in Figure 5.4 with the treatment variable recipes (All MAPDA at 350 °C and HJA for 10 min).

CZTS Device	MAPDA (min)	HJA (°C)	V_{OC} (mV)	J_{SC} (mA·cm ⁻²)	FF (%)	η (%)
MA0-150C	0	150	623	21.9	57.7	7.88
MA5-150C	5	150	638	22.3	63.0	8.97
MA8-150C	8	150	649	22.8	63.5	9.40
MA0-260C	0	260	658	21.4	62.5	8.82
MA5-260C	5	260	656	21.4	61.3	8.62
MA8-260C	8	260	675	21.6	58.0	8.44

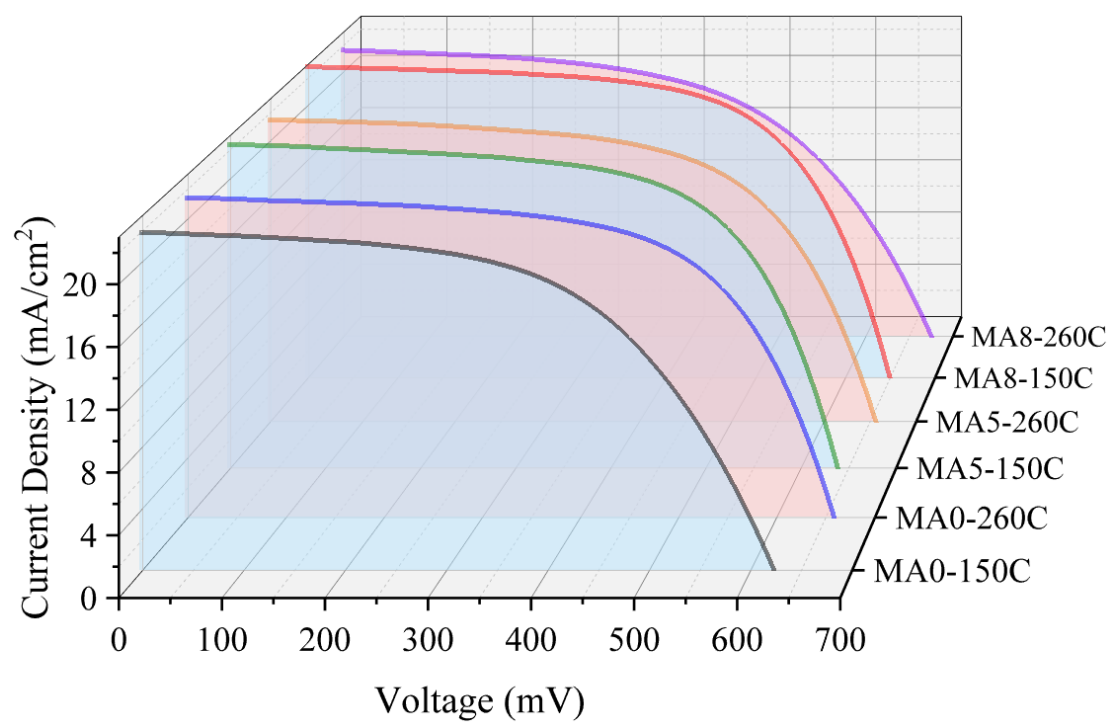


Figure 5.4 J - V characteristics of the best cells on the devices with HJA at 150 °C and 260 °C without and with MAPDA at 350 °C for 5 min and 8 min, respectively.

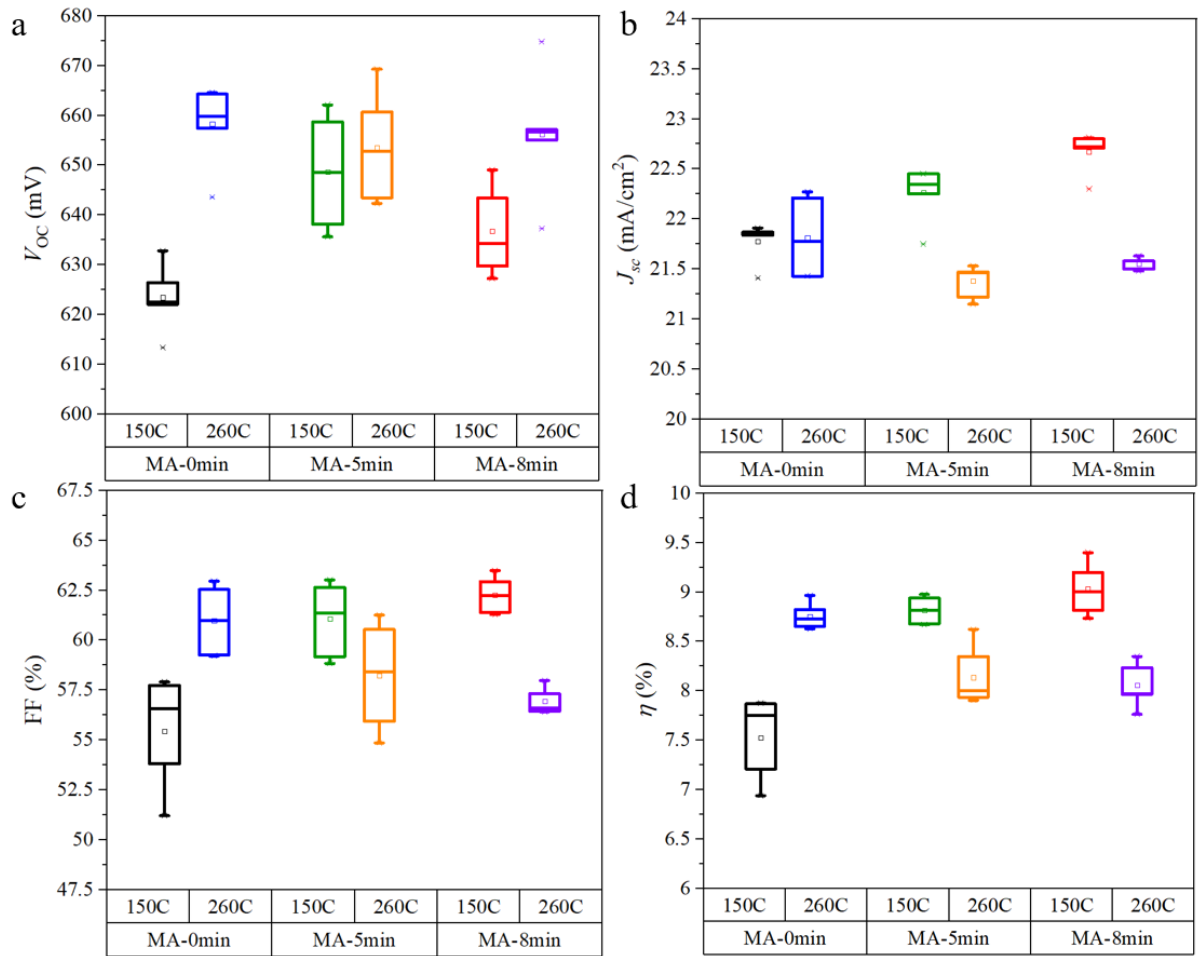


Figure 5.5 Statistical box plots of device performance parameters from fourteen cells on each device. a. V_{OC} , b. J_{SC} , c. FF and d. η .

Figure 5.6a-b show the EQE spectra of the champion cells of each device mentioned above. Regarding the best performing cells, both MA5-150C and MA8-150C involve the reduction in E_g , induced by the increased disorder during the MAPDA process, as discussed hereinbefore. This, in turn, demonstrates the smallest V_{OC} deficit among these devices – a drop by 64 mV compared to the HJA-only counterpart, as summarised in Table 5.2. Fully recovery of E_g occurred in the devices with higher HJA temperatures, while the underlying mechanisms have not yet unveiled. Moreover, a comparably small V_{OC} deficit is obtained in MA8-260C.

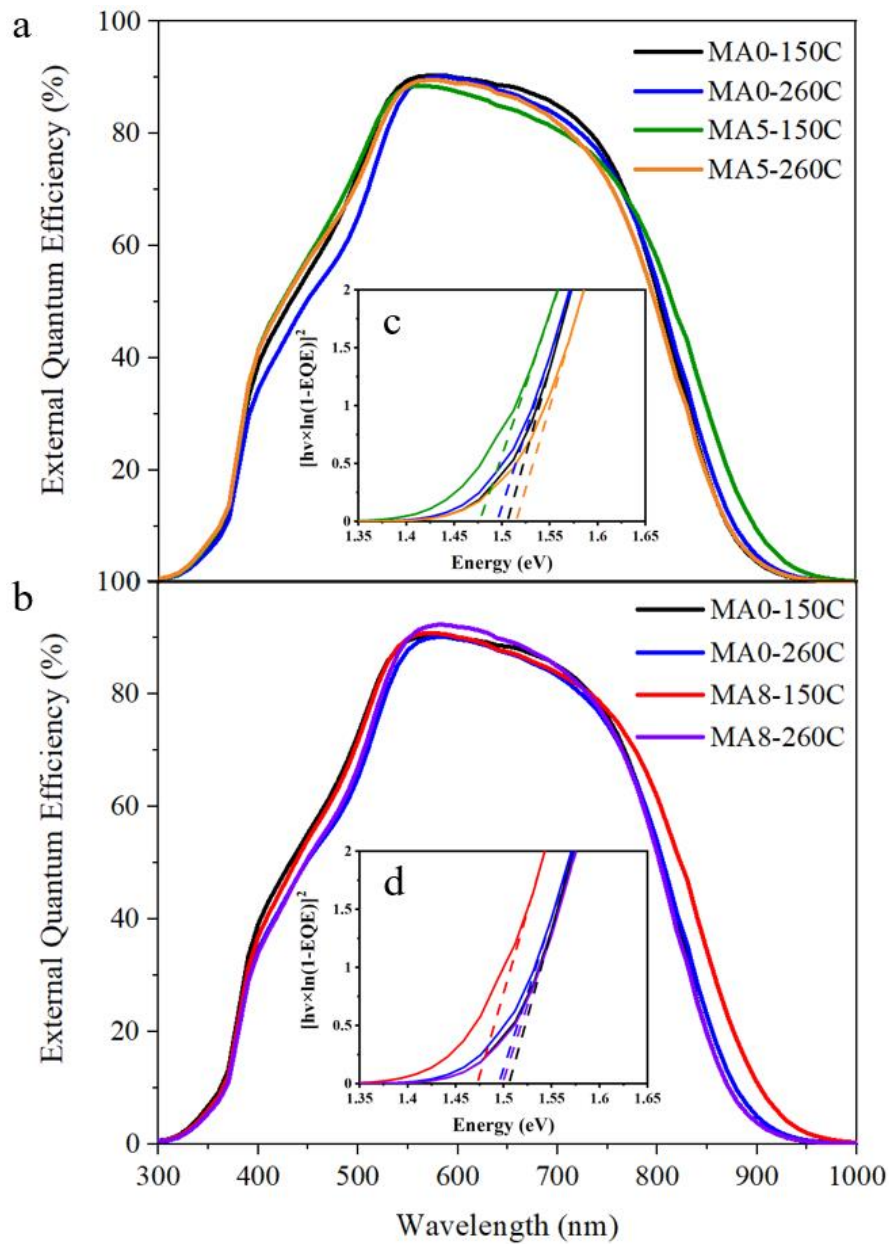


Figure 5.6 EQE spectra of the same cells in Figure 5.4. For comparison, the results were presented into two figures: a. HJA-treated samples without and with MAPDA treatment for 5 min; b. the same HJA-treated only samples but versus the counterparts with MAPDA treatment for 8 min. The inset images c. and d. show the $[h\nu \times \ln(1-EQE)]^2$ plots to determine band gaps of CZTS absorbers in Figure a and b, respectively.

Suns- V_{OC} characterization measures V_{OC} as a function of incident light intensity ²¹. Table 5.2 displays the device performance parameters of these cells obtained through fitting the Suns- V_{OC} curves by a two-diode model. MAPDA with 150-°C HJA improved pseudo FF (p.FF) and decreased saturation current density J_{02} (n=2), implying the effective alleviation of SRH recombination within the heterojunction. While by contrast, HJA at 260 °C plays a role in depressing the SRH recombination within the CZTS bulk and the heterojunction, because both J_{01} and J_{02} are reduced, but particularly J_{01} . Albeit the severe degradation in FF of MA8-260C, it shows the highest p.FF and the best bulk and heterojunction quality. Thus, the drop in FF could result from the increased series resistance, which can be clearly observed from the J - V characteristics in Figure 5.4. Overall, the combined MAPDA and HJA treatments are very effective to mitigate the SRH recombination, especially within the heterojunction. More evidence of SRH recombination alleviation will be given in Chapter 6 using advanced nanoscale optoelectronic characterizations.

Table 5.2 E_g extracted from EQE spectra, V_{OC} deficit and device performance parameters of the same cells in Figure 5.5 obtained by fitting their Suns- V_{OC} curves using a two-diode model.

CZTS	E_g	V_{OC} Deficit	p.FF	J_{01}	J_{02}
Device	(eV)	(mV)	(%)	(A·cm ⁻²)	(A·cm ⁻²)
MA0-150C	1.51	888	81.0	1.50E-11	6.77E-07
MA5-150C	1.48	847	82.9	7.03E-12	2.37E-07
MA8-150C	1.47	824	83.4	1.64E-11	7.30E-08

MA0-260C	1.50	847	81.4	3.36E-12	3.60E-07
MA5-260C	1.52	867	81.5	4.46E-12	4.33E-07
MA8-260C	1.50	825	83.9	5.20E-12	8.49E-08

5.3.3 Variations of the CdS Layer due to the Post-Annealing Treatments

As shown in Figure 5.6a-b, the change of short-wavelength response is negligible among devices with different annealing conditions. However, the MAPDA-only samples demonstrate a significantly higher blue response compared to the control samples in Chapter 4. The simplified EQE profiles (only the control in black and the optimal condition in red included) can also be found in Figure 5.7, with colour fillings for illustrating the contribution of J_{SC} improvement by different functional layers. Apart from the major improvement due to the optimization of CZTS layer, the refinement of optical response within the CdS absorption spectrum is also observed, indicating the variations of the CdS properties.

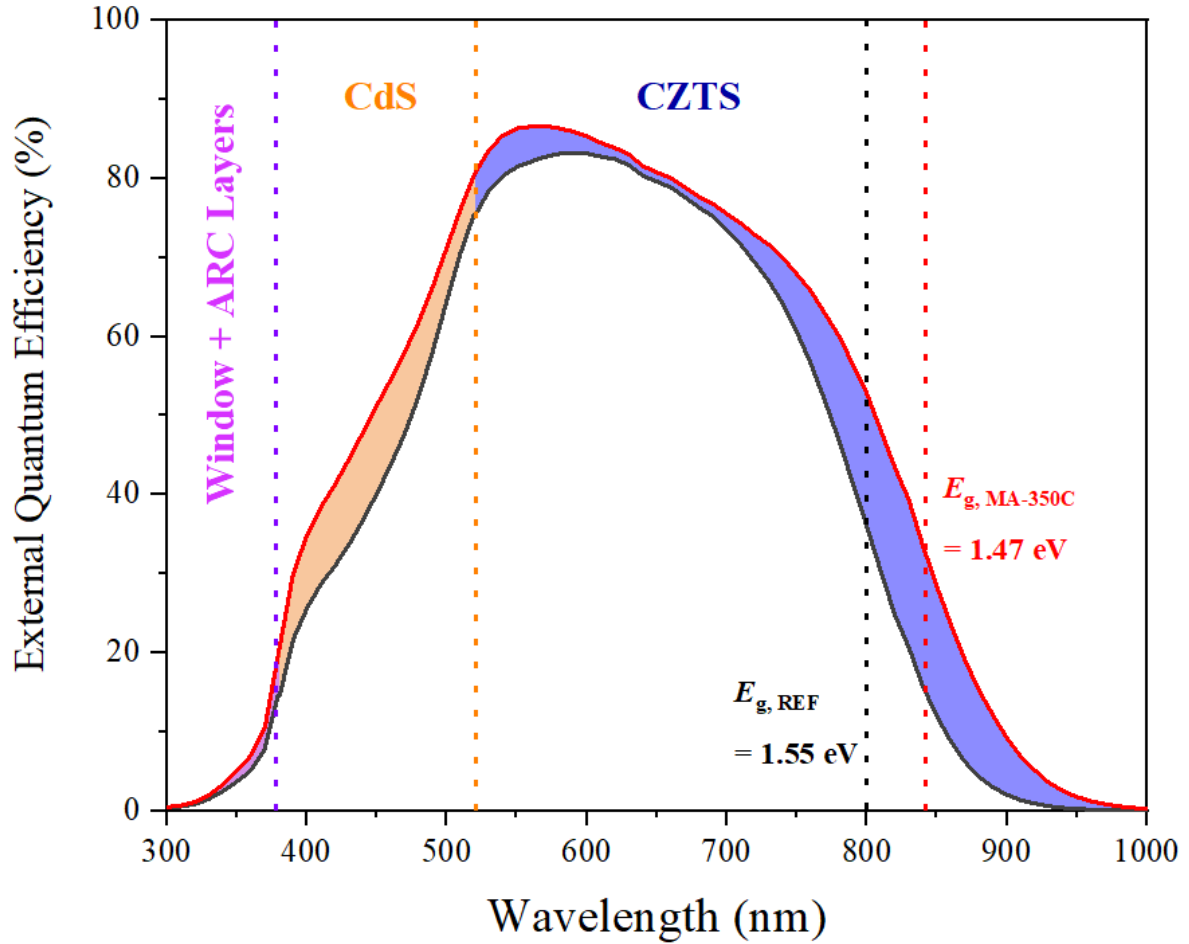


Figure 5.7 EQE spectra the control (MA0) and the modified (MAPDA @ 350 °C for 5 min, denoted as MA5) marked in black and red, respectively. The colour fillings indicate the contributions of the improvement of optical response at the different layers of the CZTS solar cells.

TEM images in Figure 5.8a reveal the unchanged thickness of the CdS layer albeit the surface chemistry of CZTS was altered by the MAPDA treatment before the CBD process. Furthermore, photoreflectance measurement performed on the CZTS samples with the CdS buffer layers (Figure 5.8b) shows a slight reduction in the CdS E_g from 2.39 eV to 2.36 eV. This observation agrees with the literature reports of the E_g decrease due to Cu doping in the CdS films^{22,23}, which was also observed here (~5 at% of Cu found in the CdS layer of the

samples with the MAPDA treatment). Therefore, the enhancement in the blue response is not related to reduced parasitic absorption by the CdS thickness reduction or the CdS E_g increase.

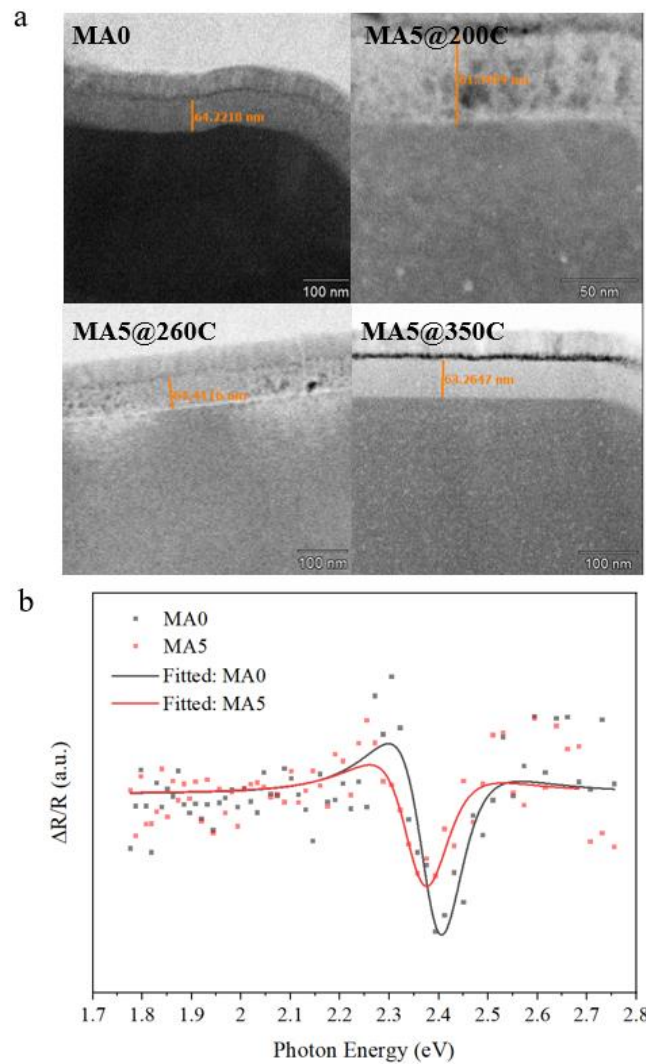


Figure 5.8 a. TEM images of MA0, MA5@200/260/350C, showing the thickness of CdS layer. b. Photoreflectance measurement for CdS films grown on the control CZTS layer (MA0) and the MAPDA-treated CZTS layer (MA5) to determine the band gaps of CdS layer: 2.39 and 2.36 eV, respectively.

X-ray diffraction (XRD) measurement was conducted for analyzing the CdS structural change after MAPDA and HJA treatments. As shown in Figure 5.9a, the orientation of the

cubic CdS is (220) in MA0, according to the JCPDS card 04-003-7133 for cubic CdS. However, MA5 reveals a smaller peak in (200) orientation but sprouting peaks at $2\theta = 42.6^\circ$ and 49.6° . These two peaks represent (110) and (200) orientations of hexagonal CdS with a shift of $\sim 1.4^\circ$ towards a smaller angle, according to the JCPDS card 04-002-3090 for hexagonal CdS. The variation of the CdS structure from cubic to hexagonal is highly likely related to the incorporation of Cu dopants where $\sim 5\%$ atomic fraction of Cu was seen in the CdS layer in Chapter 4. Cu doping can explain the slight decrease of the CdS E_g ²² as shown in our photoreflectance results (Chapter 4) and the change of its optoelectrical properties from the EQE measurement (Figure 5.7). Regarding the HJA treatment, the crystallinity of cubic CdS was improved and the orientation at (220) was strengthened, particularly for higher annealing temperatures. The increased crystallinity can reduce the defect density²⁴. MA5-150C displays a clear (220) peak demonstrating a cubic structure. Figure 5.12b shows small shifts in 2θ angles of MA5 and MA0-260C indicating the increase in the interplanar distance, which was also observed elsewhere after CdS annealing²⁵. Compared to MA0-260C, the low HJA temperature (MA5-150C) has relatively poorer crystallinity and a smaller lattice constant. The smaller CdS lattice constant could result in a smaller lattice mismatch with the CZTS surface^{5,26} which could benefit the heterointerface by reducing the dangling bonds. Furthermore, oxidation at the CdS surface, in the form of conductive CdO¹⁵ or CdSO₄¹⁶ was reported when annealing in air, particularly at a temperature beyond 300°C ¹⁷⁻¹⁹. However, our result excludes this possibility as no oxide phases were detected. It is still not clear how the change of the CdS phases affects its electrical properties and will be further investigated in future work. Possible mechanisms of spectral response improvement in the CdS absorption spectrum will be further unveiled in Chapter 6 with the aid of advanced nanoscale electrical characterization techniques.

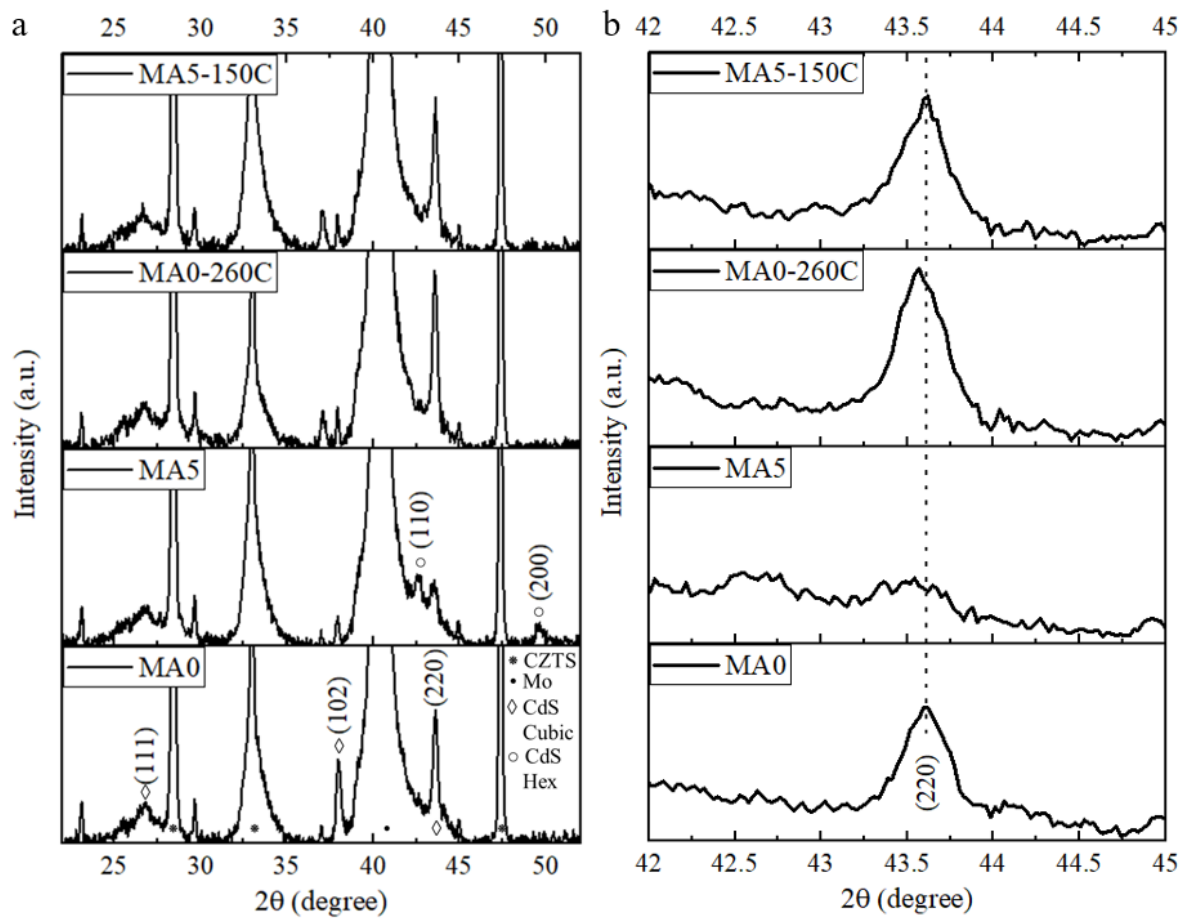


Figure 5.9 XRD patterns of CdS-coated CZTS films w/ and w/o MAPDA and/or HJA treatments. a. selected 2θ range from 22° to 52° . b. XRD of the (220) peaks of the CdS films.

5.4 Summary

In this chapter, we utilized heterojunction annealing (HJA) in air combined with the novel MAPDA treatment proposed in Chapter 4, facilitating strengthened Cd diffusion and replenishing favourable alkali metal elements. A champion efficiency at 9.40% with an average of $\sim 9\%$ was achieved using HJA at 150°C associated with the optimal MAPDA treatment. These combined treatments significantly modify the heterojunction quality. The device performance enhancement through the combined treatments surpasses that from the HJA-only treatment, which can be used to replace the latter for yielding high-efficiency

kesterite solar cells. Furthermore, variations of the CdS layer were also explored with regard to the optical and structural changes. An in-depth investigation of this layer and more evidence of heterojunction improvement will be presented in the next chapter using advanced nanoscale characterization techniques. This work not only proposes a new strategy to modify the heterojunction through optimizing the local distributions of Cd and Na, but also provides a feasible approach to manipulating the critical trace elements for chalcogenide materials in general.

5.5 Reference

- 1 Tajima, S. *et al.* Atom-probe tomographic study of interfaces of Cu₂ZnSnS₄ photovoltaic cells. *Applied Physics Letters* **105**, 093901 (2014).
- 2 Tajima, S., Umehara, M. & Mise, T. Photovoltaic properties of Cu₂ZnSnS₄ cells fabricated using ZnSnO and ZnSnO/CdS buffer layers. *Japanese Journal of Applied Physics* **55**, 112302 (2016).
- 3 Yan, C. *et al.* Cu₂ZnSnS₄ solar cells with over 10% power conversion efficiency enabled by heterojunction heat treatment. *Nature Energy* **3**, 764-772 (2018).
- 4 Minemoto, T. *et al.* Theoretical analysis of the effect of conduction band offset of window/CIS layers on performance of CIS solar cells using device simulation. *Solar Energy Materials and Solar Cells* **67**, 83-88 (2001).
- 5 Bär, M. *et al.* Cliff-like conduction band offset and KCN-induced recombination barrier enhancement at the CdS/Cu₂ZnSnS₄ thin-film solar cell heterojunction. *Applied Physics Letters* **99**, 222105 (2011).
- 6 Yan, C. *et al.* Band alignments of different buffer layers (CdS, Zn (O, S), and In₂S₃) on Cu₂ZnSnS₄. *Applied Physics Letters* **104**, 173901 (2014).

- 7 Bao, W., Sachuronggui & Qiu, F.-Y. Band offsets engineering at $\text{Cd}_x\text{Zn}_{1-x}\text{S}/\text{Cu}_2\text{ZnSnS}_4$ heterointerface. *Chinese Physics B* **25**, 127102 (2016).
- 8 Hwang, S. K. *et al.* Improved interfacial properties of electrodeposited Cu_2ZnSn (S, Se) 4 thin-film solar cells by a facile post-heat treatment process. *Progress in Photovoltaics: Research and Applications* **28** (2020).
- 9 Lu, X. *et al.* Heterojunction post-heat treatment process driving high efficiency for $\text{Cu}_2\text{ZnSnS}_4$ solar cell. *Solar Energy Materials and Solar Cells* **230**, 111204 (2021).
- 10 Liu, C. Y. *et al.* Sodium Passivation of the Grain Boundaries in CuInSe_2 and $\text{Cu}_2\text{ZnSnS}_4$ for High-Efficiency Solar Cells. *Advanced Energy Materials* **7**, 1601457 (2017).
- 11 Yuan, Z. K. *et al.* Engineering solar cell absorbers by exploring the band alignment and defect disparity: the case of Cu-and Ag-based kesterite compounds. *Advanced Functional Materials* **25**, 6733-6743 (2015).
- 12 Metin, H. & Esen, R. Annealing effects on optical and crystallographic properties of CBD grown CdS films. *Semiconductor Science and Technology* **18**, 647 (2003).
- 13 Gloeckler, M. & Sites, J. Apparent quantum efficiency effects in CdTe solar cells. *Journal of Applied Physics* **95**, 4438-4445 (2004).
- 14 Liu, F. *et al.* Light-Bias-Dependent External Quantum Efficiency of Kesterite $\text{Cu}_2\text{ZnSnS}_4$ Solar Cells. *ACS Photonics* **4**, 1684-1690 (2017).
- 15 Metin, H. & Esen, R. Annealing studies on CBD grown CdS thin films. *Journal of Crystal Growth* **258**, 141-148 (2003).
- 16 El Maliki, H. *et al.* Study of the influence of annealing on the properties of CBD-CdS thin films. *Applied Surface Science* **205**, 65-79 (2003).

- 17 Narayanan, K., Vijayakumar, K. & Nair, K. Chemical bath deposition of CdS thin films and their partial conversion to CdO on annealing. *Bulletin of materials science* **20**, 287-295 (1997).
- 18 Tomas, S. *et al.* Influence of thermal annealings in different atmospheres on the band-gap shift and resistivity of CdS thin films. *Journal of applied physics* **78**, 2204-2207 (1995).
- 19 Nair, P., Daza, O. G., Readigos, A. A.-C., Campos, J. & Nair, M. Formation of conductive CdO layer on CdS thin films during air heating. *Semiconductor Science and Technology* **16**, 651 (2001).
- 20 Scragg, J. J., Choubrac, L., Lafond, A., Ericson, T. & Platzer-Björkman, C. A low-temperature order-disorder transition in Cu₂ZnSnS₄ thin films. *Applied Physics Letters* **104**, 041911 (2014).
- 21 Kunz, O., Varlamov, S. & Aberle, A. in *2009 34th IEEE Photovoltaic Specialists Conference (PVSC)*. 000158-000163 (IEEE).
- 22 Mariappan, R., Ponnuswamy, V., Ragavendar, M., Krishnamoorthi, D. & Sankar, C. The effect of annealing temperature on structural and optical properties of undoped and Cu doped CdS thin films. *Optik* **123**, 1098-1102 (2012).
- 23 Petre, D., Pintilie, I., Pentia, E. & Botila, T. The influence of Cu doping on opto-electronic properties of chemically deposited CdS. *Materials Science and Engineering: B* **58**, 238-243 (1999).
- 24 Goto, F., Shirai, K. & Ichimura, M. Defect reduction in electrochemically deposited CdS thin films by annealing in O₂. *Solar Energy Materials and Solar Cells* **50**, 147-153 (1998).

- 25 Vigil, O., Zelaya-Angel, O. & Rodriguez, Y. Changes of the structural and optical properties of cubic CdS films on annealing in H₂ and air atmospheres. *Semiconductor Science and Technology* **15**, 259 (2000).
- 26 Haight, R. *et al.* Band alignment at the Cu₂ZnSn(S_xSe_{1-x})₄/CdS interface. *Applied Physics Letters* **98**, 253502 (2011).

Chapter 6

In-depth Study of Moisture-assisted Post-deposition Annealing & Heterojunction Air Annealing by Nanoscale Optoelectronic Characterization Techniques

6.1 Introduction

The moisture-assisted post-deposition annealing (MAPDA) treatment introduced in Chapter 4 and the integration of MAPDA and heterojunction annealing (HJA) introduced in Chapter 5 are considered as promising post-treatment technologies for wide applications, such as extrinsic elemental incorporation, manipulation of alkali metals after the formation of the CZTS films, the heterojunction and bulk modification, etc. An in-depth understanding of this novel technology is essential for broader applications. In this chapter, scanning probe microscopies including Kelvin probe force microscopy (KPFM) and conductive atomic force microscopy (C-AFM) were applied to understand the nanoscale optoelectronic properties of the CZTS films with MAPDA and the CdS-coated CZTS films undergone the combined MAPDA and HJA treatments. The effect of excessive Na and K at the CZTS surface was unveiled by KPFM and C-AFM. Systematic surface photovoltage (SPV) investigation was performed on the CdS-coated CZTS samples using KPFM to demonstrate the overall improvement of the heterojunction, the CZTS bulk and the CZTS grain boundaries (GBs). SPV measurement under low photon injection reveals the substantial mitigation of SRH recombination. The variations of the CdS optoelectronic properties were discussed using SPV measurement with low-wavelength photoexcitation. As this chapter is mainly focused on the KPFM and its application, the principle of KPFM is first introduced in the next section,

followed by experiment result and discussion of its applications in kesterite solar cells received MAPDA and HJA treatment.

6.2 KPFM Operation Principle, Applications of Chalcopyrite/Kesterite Semiconductors & Methods

KPFM is an extended application of atomic force microscopy (AFM), with the integration of the Kelvin probe, enabling the simultaneous measurement of surface potential and morphology. The term “Kelvin probe” is named in memory of Lord Kelvin who conducted the parallel plate capacitor experiments in 1898¹. In 1932, the Kelvin probe was developed to measure contact potential differences between dissimilar metals by William Zisman, who incorporated the vibrating condenser with the reference metal with a known work function². The first integration of the Kelvin probe and AFM was achieved in 1991, facilitating the simultaneous imaging of topography and CPD of various metals in a lateral dimension smaller than 50 nm³. Since then, KPFM has been widely used in photovoltaics, photocatalysis, gas sensors, etc.

6.2.1 KPFM Operation Principle

As KPFM is a non-contact characterization technique, tip and sample can be regarded as two plates of one capacitor, as depicted in Figure 6.1a. The charge flow leads to the formation of an electric field between tip and sample due to the work function difference between these materials. When the tip touches the sample surface (Figure 6.1b), electrons move from the low work function material to the other, resulting in the alignment of the Fermi level. Therefore, the local vacuum levels separate and generate a potential difference between tip

and sample, known as the contact potential difference (CPD). The CPD value can be obtained by nullifying the potential difference through a biased DC voltage, as shown in Figure 6.1c.

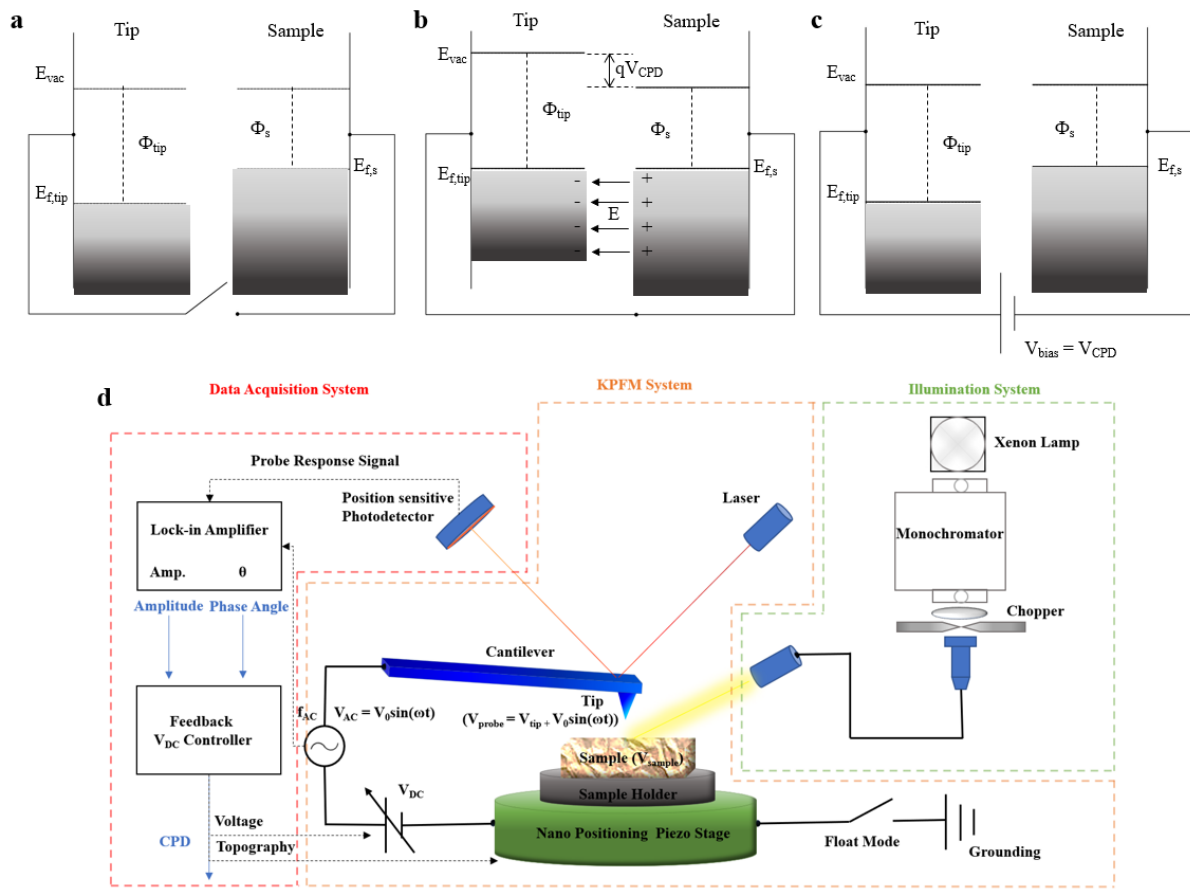


Figure 6.1 Energy diagram a. before contact, b. after contact, c. electrostatic force nullified by bias voltage, equivalent to V_{CPD} . d. Schematic diagram of KPFM apparatus with three major components: KPFM System, Data Acquisition System, and Illumination System.

Now, let us consider the case that dipoles exist between the sample surface and the tip. An electric field generated between these charged “plates” as

$$E = \frac{\sigma}{\epsilon_0} \quad (4)$$

where σ is the charge density per unit area ($\sigma = Q/A$). Therefore,

$$E = \frac{\sigma}{\epsilon_0} = \frac{Q}{\epsilon_0 A} \quad (5)$$

The potential between the plates,

$$V = E \cdot d = \frac{Qd}{\epsilon_0 A} \quad (6)$$

We can get,

$$Q = \epsilon_0 A \frac{V}{d} \quad (7)$$

Here we have the capacitance between two plates,

$$C = \frac{Q}{V} = \frac{\epsilon_0 A}{z} \quad (8)$$

where z is the distance between two plates (i.e., lift height of tip from the sample surface).

The electrostatic force,

$$F_{ES} = q_{\text{sample}} E_{\text{tip}} = (-Q) \cdot \frac{Q}{2 \cdot \epsilon_0 A} = \frac{1}{2} \left(\frac{\epsilon_0 A}{z^2} \right) V^2 \text{ (attractive)} \quad (9)$$

where the minus sign represents the opposite charge at the sample surface to the tip and results in the attractive force. The term $\epsilon_0 A/z^2 = dC/dz$, thus

$$F_{ES} = \frac{1}{2} \left(\frac{\epsilon_0 A}{z^2} \right) V^2 = \frac{1}{2} \frac{dC}{dz} V^2 \text{ (attractive)} \quad (10)$$

The operation of the KPFM apparatus has been briefly summarized in Figure 6.1d, which generally configured into three components: the KPFM system, the data acquisition system and the illumination system. The sample is electrically connected with the metal sample holder, which contacts with the nanopositioning piezo stage. The sample stack can be either connected in a float mode or grounding. The bias illumination source can be a Xenon lamp, LED or laser with the monochromator and neutral density filters for wavelength and intensity modulations, respectively. The cantilever deflection induced by the electrostatic force between a tip and a sample surface is detected by a photodetector with the aid of a tracking laser beam. The corresponding frequency f_{AC} is derived from the lock-in amplifier, which transfers the amplitude and phase angle signals to the feedback controller. A CPD value is

dependent on the adjustment of the biased DC voltage in the condition of nought f_{AC} through regulation. Here we have,

$$\Delta V_{\text{probe-sample}} = (V_{\text{tip}} + V_0 \sin(\omega t)) - V_{\text{sample}} \quad (11)$$

where V_{tip} is adjusted by V_{DC} . By substituting Equation (11) into Equation (10), the electrostatic force between the tip and the sample surface can be simply obtained,

$$F_{ES} = -\frac{1}{2} \frac{dC}{dz} [(V_{\text{tip}} - V_{\text{sample}}) - V_0 \sin(\omega t)]^2 \quad (12)$$

The angular frequency, $\omega = 2\pi f_{AC}$. Setting $f_{AC} = 0$,

$$F_{ES} = -\frac{1}{2} \frac{dC}{dz} (V_{\text{tip}} - V_{\text{sample}})^2 = -\frac{1}{2} \frac{dC}{dz} \left[\frac{\Phi_{\text{tip}} - \Phi_{\text{sample}}}{q} \right]^2 \quad (13)$$

where Φ_{tip} and Φ_{sample} represent work functions of the tip and the sample surface, respectively. The electrostatic force is nullified by setting the DC voltage equivalent to $(\Phi_{\text{tip}} - \Phi_{\text{sample}})/-q$, known as CPD.

6.2.2 Applications of KPFM in Chalcopyrite and Kesterite Semiconductors

The applications of KPFM in chalcopyrite semiconductors date back to the 1990s⁴, which have been used to derive the conduction band offset⁴, work function variations at the different crystal orientations (inhomogeneity of the chalcopyrite surface)⁵, observation of the buried homojunction⁶, built-in potentials at grain boundaries (GBs)⁷⁻⁹, etc. Researchers from International Iberian Nanotechnology Laboratory (INL) determined a correlation of the surface potential variations at the CIGSe GBs with the device performance upon different alkali-fluoride PDT, based on KPFM measurement of massive samples and numerical simulations¹⁰. Their findings associated the detrimental effect of downward banding at the GBs with losses in the device performance, particularly V_{OC} , which can be passivated by alkali-indium-selenide phases formed through heavy alkali-fluoride PDT¹⁰.

To the best of our knowledge, the first systematic KPFM study in kesterite semiconductors was reported until 2012¹¹, which demonstrates the similar GB roles with those in CIGS and CdTe semiconductors, showing downward band bending at the GBs as a channel of current flow¹¹. Different bending directions have been reported among kesterite semiconductors with/without different treatments¹². However, due to the presence of surface depletion, it is difficult to determine the real GB bending direction and magnitude underlying the surface⁷. Leite et al.¹³ correlated the surface photovoltage (SPV, obtained by dark and illuminated KPFM measurements) with the V_{OC} of photovoltaic devices, which can be applied to a wide range of semiconductors, not only applicable to the grain surface but also GBs in a nanoscale. This metrology is described in detail and utilized in Sections 6.4 & 6.5. Kim et al.¹⁴ used KPFM to study SPV at low light intensity to investigate indoor applications' potential. In this chapter, we also conducted similar research by light intensity-dependent SPV analysis.

6.2.3 Method of KPFM in This Thesis

The KPFM measurement was carried out in an AIST-NT SmartSPM 1000 AFM system. The tips used in the KPFM system in this work are made of monocrystalline silicon with a nitrogen-doped diamond coating (coating film resistivity at 0.5-1 $\Omega\cdot\text{cm}$ and resonant frequency 260-630 kHz, series number DCP20 by TipsNano). The cantilever has Au reflective side coating. The samples were grounded and measured using a two-pass scan in resonant frequency (one pass with a contact mode for topography measurement and the other with a non-contact mode for CPD mapping). The 450 nm and 750 nm pulsed lasers were used for the measurement under illumination with a frequency of ~80 MHz and an intensity of

~1000 W/m². Various light intensities were applied for the light intensity-dependent KPFM measurement. Repetitive measurements were performed to give the consistent results.

6.3 The Effect of Excessive Na and K at the CZTS Surface

As mentioned in Section 4.3.1 in Chapter 4, the removal of Na involves two steps: MAPDA and the post-washing/etching process (in hot ammonia during the CdS CBD process in this case). Therefore, the as-MAPDA CZTS surface contains excessive Na and K while the bulk is Na-depleted. Because the surface potential of kesterite films are highly sensitive to the local Na concentration ^{7,12}, the CPD obtained by the KPFM probe is significantly affected by the extensive Na and K phases at the CZTS surface. This chapter takes the previous chapter of the denotations of all samples. Figure 6.2a shows the topography and the CPD maps of the control (MA0) and the MAPDA-treated (MA5). Three batches in each group were obtained for ensuring the data repeatability. The CPD distributions were summarized in Figure 6.2b. The increase of the average CPD values for the as-MAPDA CZTS surface suggests an increased surface work function, implying smaller surface downward band bending and thus deteriorating V_{OC} . Regarding the change in the GBs, the increase of CPD is smaller than that at the grain surface (GS), resulting in a larger GB-GS potential difference, as shown in Figure 6.3. Considering the surface depletion ⁷, we would not conclude stronger band bending is present at the GBs underlying the CZTS surface. Assuming the similar buried GBs, the negative potential difference means smaller work functions at the GBs (i.e. weaker p-type doping), indicating a downward bending but rather small in magnitude, compared to those in CIGSe solar cells ^{7,8}. A slightly larger downward bending observed in the MAPDA-treated samples may indicate an increased loss in V_{OC} ^{10,15,16}.

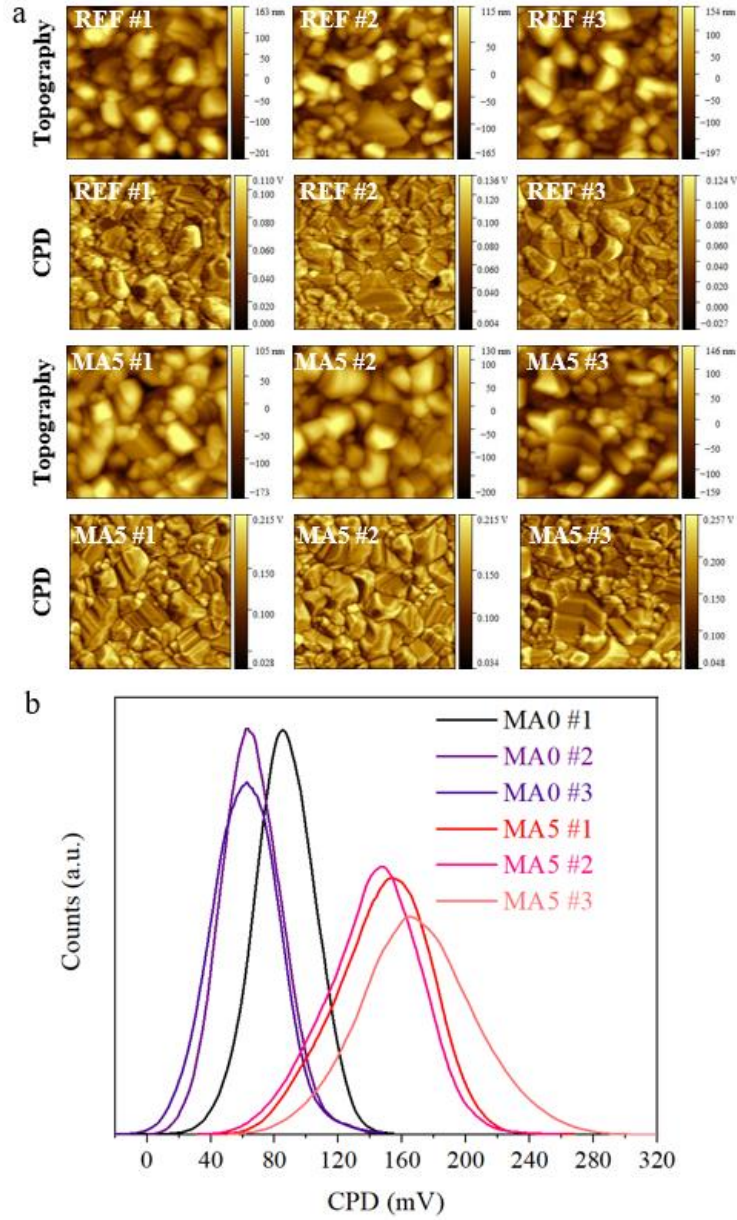


Figure 6.2 KPFM measurement for the control CZTS films (MA0) and CZTS films with MAPDA treatment at 350 °C for 5 min (MA5). Three samples for each type were measured to ensure the data reliability. a. topography and CPD mappings of these samples. b. CPD distributions.

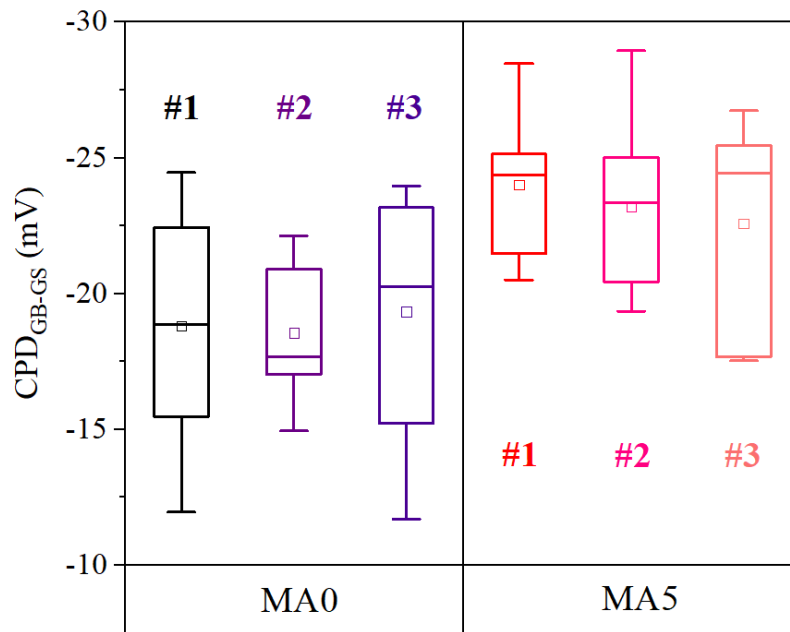


Figure 6.3 Difference of the CPD values between the grain boundary (GB) and the adjacent grain surfaces (GS). The data was extracted from the CPD maps in Figure 6.2.

Figure 6.4 shows the shunt current maps measured by conductive-AFM (C-AFM) on the bare CZTS films – MA0 and MA5 under a bias voltage of -1.5 V. A much larger shunt current can be seen at the surface of MA5 with high Na and K concentrations, suggesting the formation of shunt path at the Na/K-rich CZTS surface. Saucedo et al. also reported heavily shunting in CZTSSe devices induced by high Na concentration at the heterojunction region ¹⁷. Overall, based on the observations of KPFM and C-AFM results, we found that excessive Na and K accumulation is detrimental, weakening the surface depletion, deteriorating the GBs and generating shunting paths. The MAPDA treatment followed by a soaking process can be used to effectively control Na and K concentrations and to prevent excessive Na and K accumulation. The relevant KPFM and C-AFM results are not shown here because the rinsed alkali-depleted samples still cannot reflect the realistic conditions where Cd incorporation occurred after the CdS deposition.

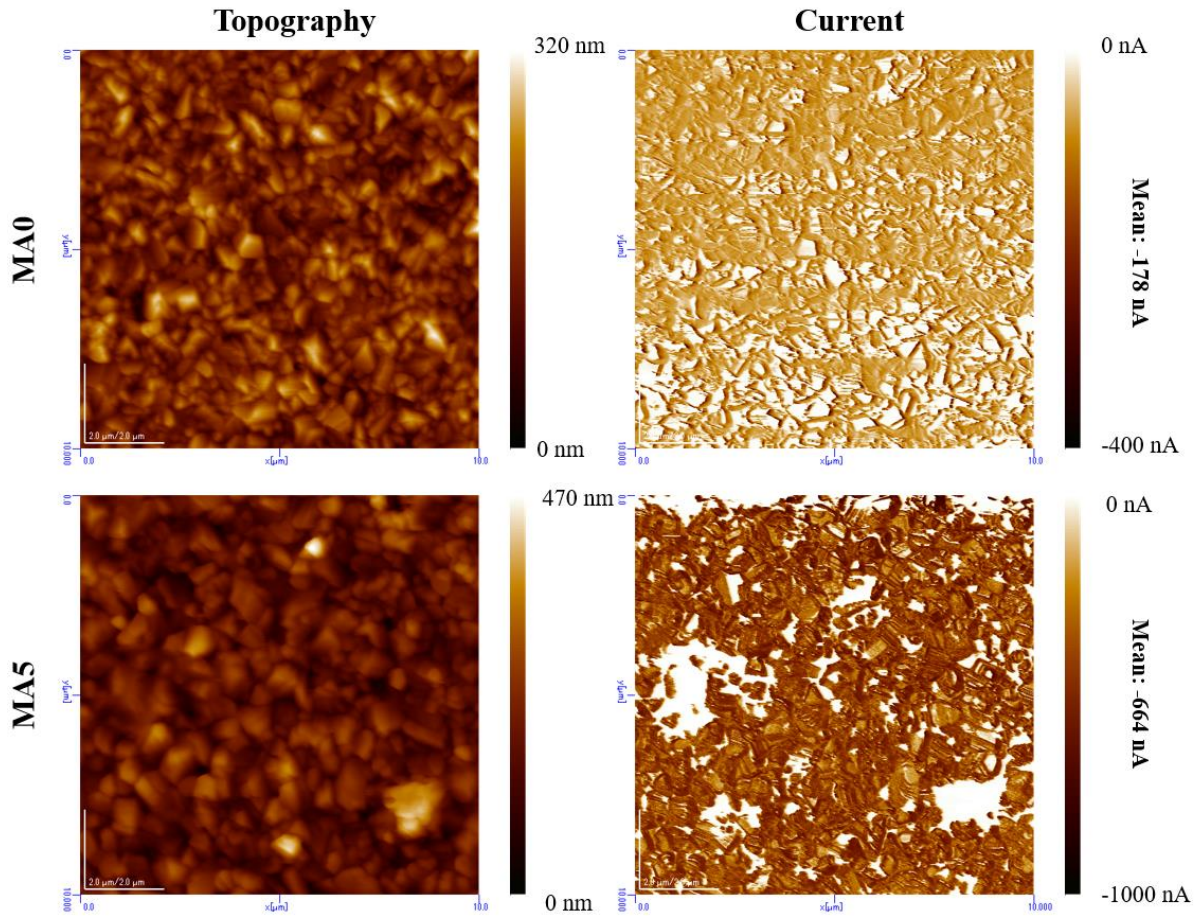


Figure 6.4 Topography and shunt current maps of MA0 and MA5, obtain from C-AFM, measured under -1.5 V bias voltage.

6.4 Direct Observations of the V_{OC} Improvement in a Nanoscale View

This section used SPV analysis derived from dark and illuminated KPFM measurements to investigate the V_{OC} improvement. Leite et al.¹³ correlated SPV with the V_{OC} through the measurement of quasi-Fermi level splitting (QFLS), following.

$$\begin{aligned}
 q \cdot V_{CPD@Light} &= \Phi_{tip} - \Phi_{sample@Light} \\
 &= q \cdot V_{CPD@Dark} + \Delta\mu \text{ (under illumination)}
 \end{aligned} \tag{14}$$

$$V_{OC} = \frac{\Delta\mu}{q} = V_{CPD@Light} - V_{CPD@Dark} = SPV \quad (15)$$

where $\Delta\mu$ is the quasi-Fermi level splitting (QFLS) when the tip measures the surface of p-type materials and the sample is bottom grounded. $\Delta\mu$ is negative for n-type materials, and thus large absolute value of SPV ($|SPV|$) represents large V_{OC} . It is worth noting that the V_{OC} obtained from this method is different from that derived from the JV simulators, because of the monochromatic illumination at a relatively small area of $\sim 6 \text{ mm}^2$, as well as the absence of the influence from the top functional layers (i-ZnO high-resistivity layer and heavily n-type doped ITO layer).

In this thesis, SPV analysis was performed on the CdS-coated CZTS samples where the bottom of CZTS was grounded. Under illumination, the QFLS contributes to the rise of quasi-Fermi level at the CdS surface where measured by KPFM probe, leading to the decrease of CdS work function and thus CPD value. SPV values were obtained from the difference between the mean CPD values measured under light and dark. 750 nm laser was used to excite the CZTS bulk, and the photogenerated electrons were collected at the surface of the CdS layer, transporting across the heterojunction region. Therefore, the SPV obtained under this condition was determined by the overall properties of the CZTS bulk, the heterojunction and the CdS layer. Figure 6.5a shows the raw topography and the CPD images measured at dark and under illumination. Figure 6.5b illustrates the CPD distributions, and the inset bar chart displays the SPV values. Compared to MA0, MA5 shows small $|SPV|$ improvement. By contrast, the HJA-treated samples show considerably larger SPV, including MA0-260C. Those with the combined MAPDA and HJA treatments (MA5-150C and MA5-260C) show the most dramatic improvement. The large contrast can be seen in the V_{OC} maps (Figure 6.6). Considering the relation between $|SPV|$ and QFLS, the gentle increase in $|SPV|$

demonstrates negligible improvement of QFLS in MA5, which could be arisen from the reduction in the E_g due to the more disordered CZTS films (mainly due to the lift of VBM¹⁸). Thus, MA5 has a better performance than MA0 if considering the larger E_g decrease in magnitude (~80 meV, as demonstrated in Chapter 4). The HJA treatment only (MA0-260C) significantly enhances the QFLS, which agrees with our previous findings through the heterojunction annealing in N₂¹⁹. By contrast, the combined MAPDA and HJA treatments (MA5-150C and MA5-260C) yield considerably stronger QFLS than the HJA-only treatment. Comparing these two samples, notwithstanding MA5-260C shows stronger QFLS, when considering the E_g difference of these two samples, MA5-150C has the best performance. Furthermore, assuming uniform electron affinity over the CZTS surface, the increased surface potential uniformity of MA5-150C indicates the reduction of local potential fluctuation of the CZTS conduction band edge⁹, because the underlying CZTS surface has strong impacts on the CPD collection at the CdS surface, particularly from the potential uniformity at the CZTS surface and the CZTS GBs²⁰.

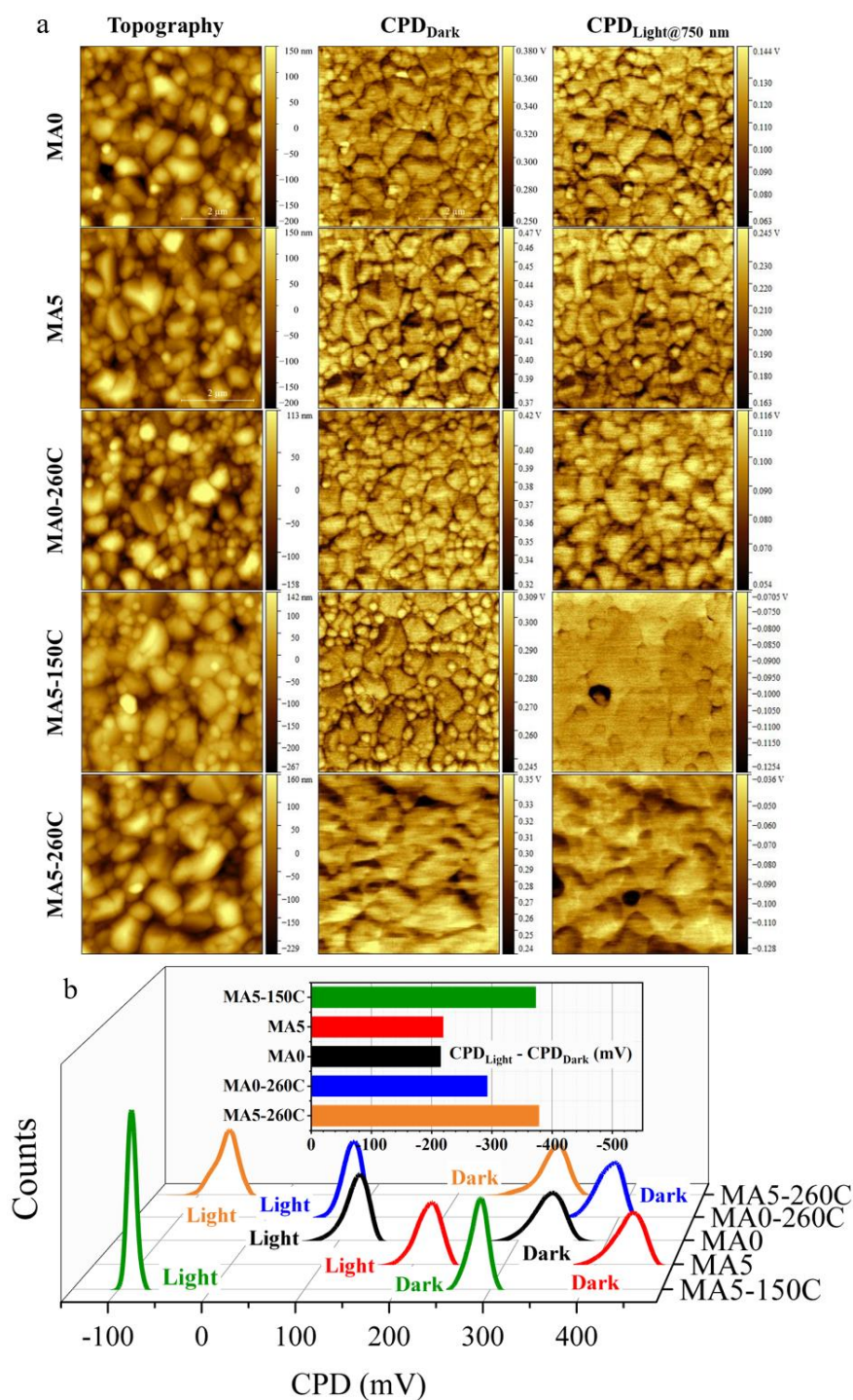


Figure 6.5 KPFM measurement for the CdS-coated CZTS samples w/ and w/o MAPDA and/or HJA treatments. a. Raw topography and CPD images. B. CPD distributions extracted from CPD maps measured at dark and light at 750 nm with intensity of $\sim 1000 \text{ W/m}^2$. The inset bar chart shows the SPV values of each sample.

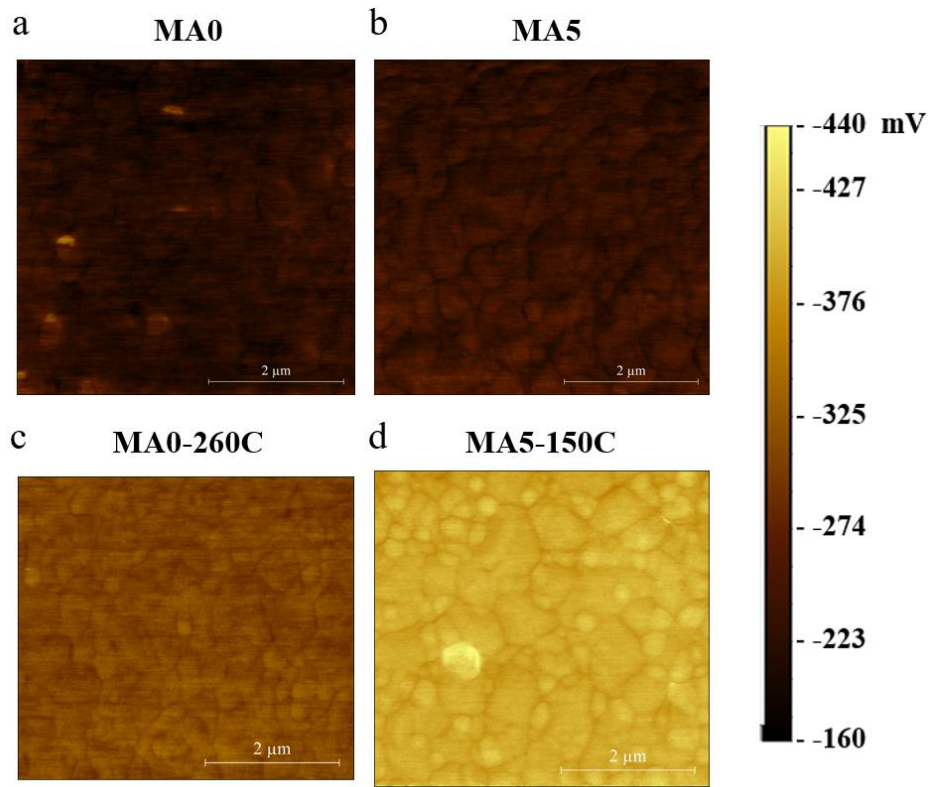


Figure 6.6 Open circuit voltage (V_{oc}) variation maps with nanoscale resolution, derived from the difference of $\text{CPD@Dark} - \text{CPD@Light}$. 750 nm laser with $\sim 1000\ \text{W/m}^2$ intensity was used.

The alleviation of SRH recombination was further noticed from light intensity-dependent KPFM measurement. Figure 6.7a shows the raw topography and the CPD maps under various light intensity with excitation wavelength at 750 nm. The values of light intensity can be found in the inset bar chart in Figure 6.7b. The CPD distributions of each sample at different light intensity were plotted in Figure 6.7b. SPV value can be estimated from the CPD decrement of those measured under illumination (marked in 2-5) by that at dark (marked in 1). Under very low photon injection ($\sim 1.6 \times 10^{-2}\ \text{W/m}^2$), SPV is close to zero in MA0 and MA5, while higher SPV can be seen in the HJA-treated samples, especially in those with the combined treatments. As the intensity increased to $\sim 65\ \text{W/m}^2$ (marked as 3), MA0, MA5 and MA0-260C present gradual increase in SPV, while a significant boost of SPV can be

observed in MA5-150C and MA5-260C. The remarkable increase in SPV value under low photon injection indicates the pronounced QFLS happened in both samples with the combined treatments, which is achieved by the mitigation of SRH recombination caused via deep-level defects ¹⁴. The alleviation of the trap-assisted recombination is very likely linked to the significant decrease of deep acceptor-like defects at the CdS/CZTS heterointerface and the CZTS bulk, as discussed in Section 4.3.4 and 4.3.5. The QFLS at such a weak light response may also imply that the Fermi-level pinning issue caused by the high concentration of deep acceptor states was mitigated. Such improvement of QFLS under low photon injection suggests that the combined MAPDA and HJA treatments can be used in indoor applications, such as the PV-integrated internet of things (IoT) electronic devices ^{14,21}.

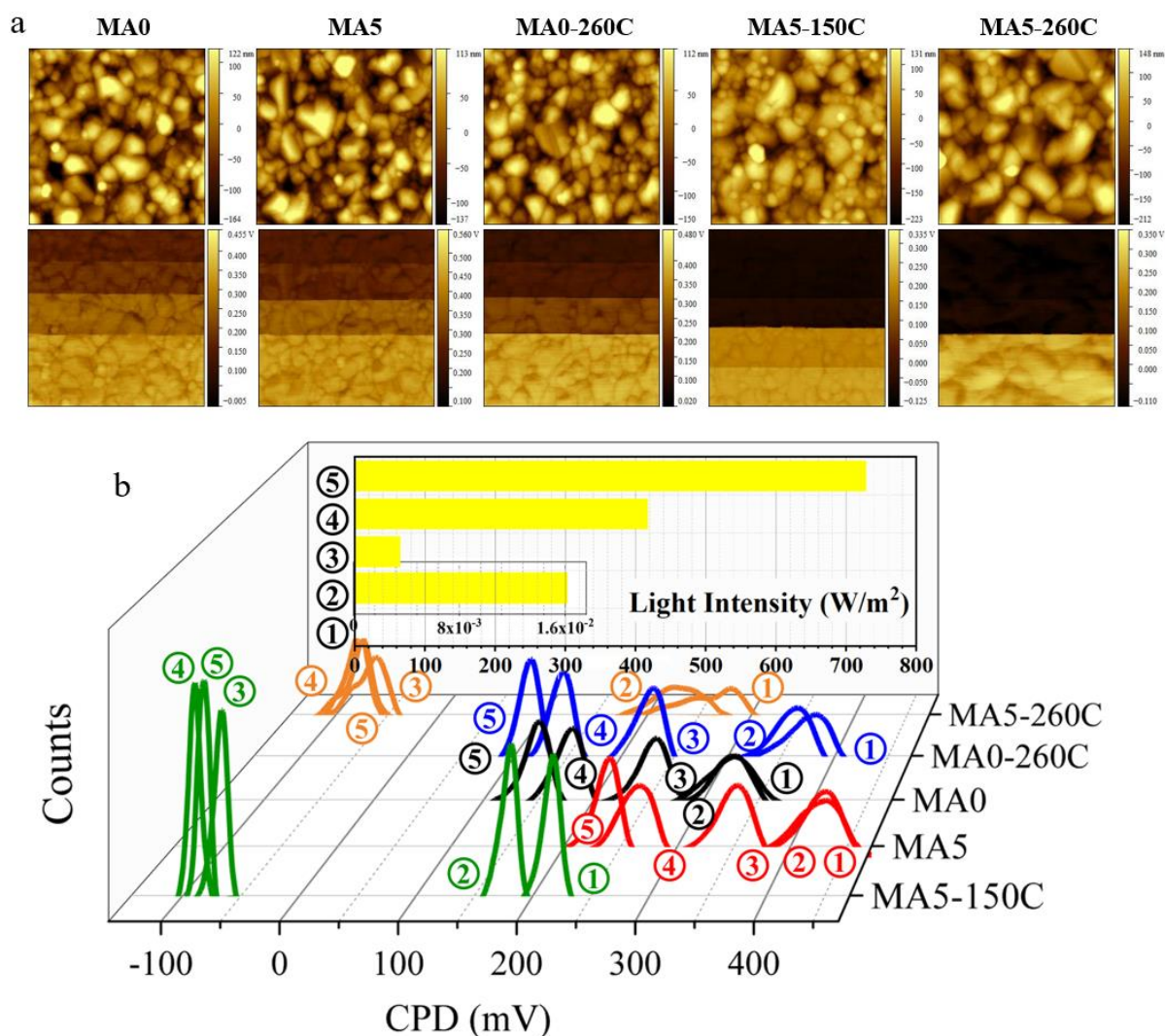


Figure 6.7 Light intensity-dependent KPFM measurement at 750 nm excitation wavelength for the CdS-coated CZTS samples w/ (MA5) and w/o (MA0) MAPDA and (MA5-150C & MA5-260C)/or (MA0-260C) HJA treatments. a. Raw topography and CPD images. The same scale range was used for CPD images, providing direct visual contrast of the CPD change. b. The CPD distributions at each light intensity. The numbers represent the corresponding light intensity shown in the inset bar chart.

The contributions of SPV increase by grain interiors (GIs) and GBs are investigated through line scans across eight random GBs and the adjacent GIs, as shown in Figure 6.8a. Figure

6.8b exhibits the statistical results of CPD measured at dark and under illumination (750 nm, $\sim 1000 \text{ W/m}^2$) at both GIs and GBs, and the SPV value was plotted in the bar chart. The bar chart in the top panel shows the SPV difference between the GBs and the GIs. Overall, the GBs have lower SPV than the GIs for all samples, indicating larger V_{oc} loss at the CZTS GBs relative to the GIs. MA5 shows negligible SPV improvement compared to MA0, especially at the GBs. The HJA treatment promotes the SPV increase at both GIs and GBs, especially for the combined treatments, indicating the overall refinements. Comparing MA5-260C with MA5-150C which has a similar SPV improvement at GIs, higher SPV at GBs in MA5-260C results in the smaller GB-GI difference, representing more benign GBs. Passivation of the GBs may be attributed to the accumulation of higher concentration of Cd and Na at these GBs, as discussed and displayed in Chapter 4.

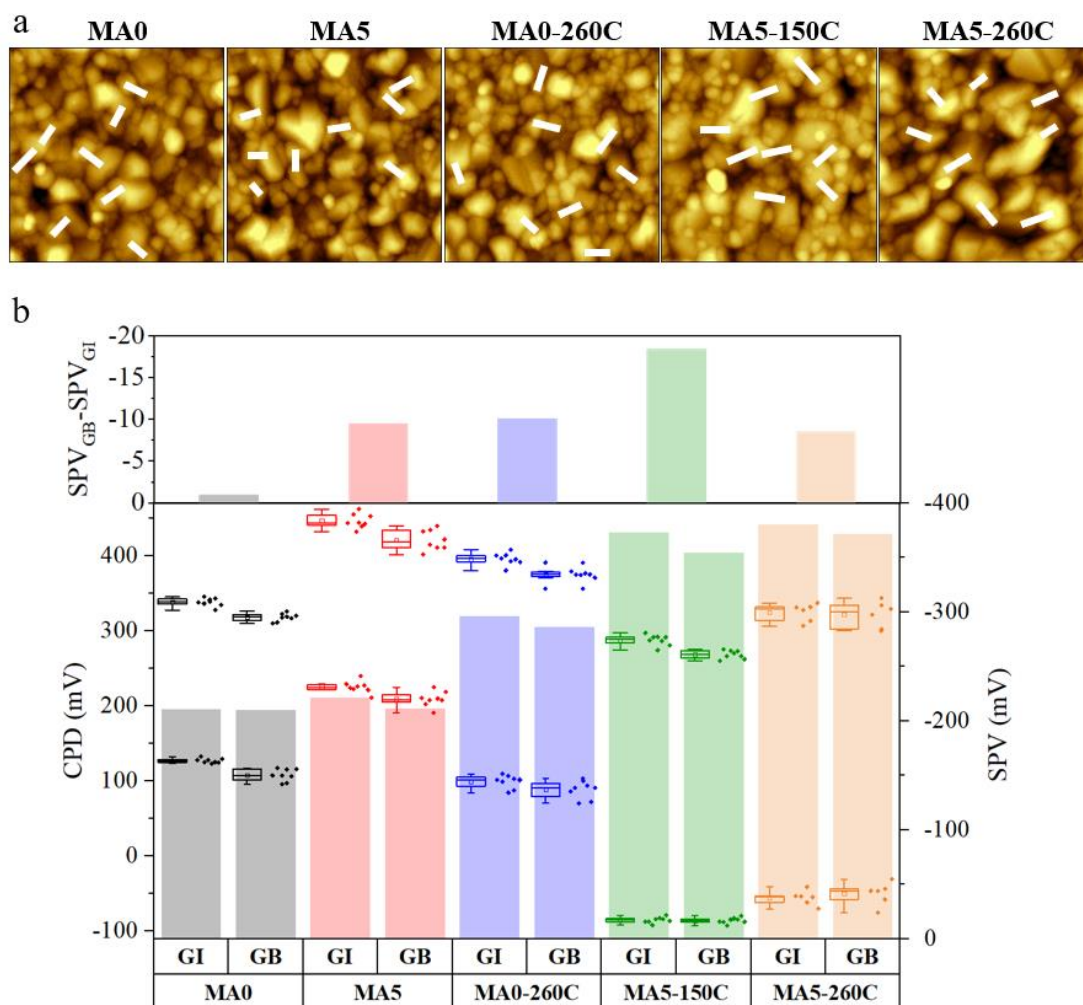


Figure 6.8 SPV analysis for GIs and GBs of CZTS/CdS samples w/ and/or w/o MAPDA and/or HJA treatments. a. Selection of random grain boundaries from the topography images. b. Statistical results of CPD (box chart) measured at dark (higher CPD values) and under illumination (lower CPD values) for GIs and GBs. The bar chart shows the surface photovoltage (SPV) of GIs and GB for each sample. The bar chart in the top panel displays the SPV difference from GBs to GIs.

6.5 Investigation of the CdS Variations due to MAPDA and HJA

In Chapter 5, we have studied the CdS change which is possibly induced by the elemental interdiffusion. The change of CdS structure was observed by XRD measurement. However, it

is difficult to obtain direct evidence of variations in its optoelectronic properties, because of the underlying CZTS layer and the Mo contact. To further explore the reasons for the CdS change, we conducted a similar SPV measurement using 450 nm excitation wavelength which can be absorbed by both the CdS layer and the CZTS surface region. It should be noted that two interfaces have to be considered: both the CZTS/CdS heterointerface and the CdS/air interface, as shown in Figure 6.9a. For the CZTS/CdS heterointerface, under illumination, QFLS would rise the quasi-Fermi level within CdS (i.e. decrease in work function and thus CPD). The trend is identical with the previous measurement under 750-nm excitation. However, the surface depletion of the CdS layer would increase the work function (i.e. CPD value) under illumination. By contrast, under high light intensity, the CPD drop due to QFLS at the heterojunction would be dominant.

Figure 6.9b shows the CPD distributions under different light intensities. The CPD increase for the HJA samples (MA0-260C and MA5-260C) is significantly higher than the HJA-absent samples under relatively low photon injection. The CPD increase may indicate better CdS qualities and/or more defective heterojunctions. However, according to a series of characterizations hereinbefore (including the Suns- V_{oc} and SPV (@ 750 nm excitation) measurements), the HJA demonstrates an improved heterojunction. Therefore, a higher CPD is more likely suggests an improved CdS layer (such as fewer defects or higher doping levels). On the other hand, compared to MA0, the MAPDA-only sample (MA5) shows a smaller CPD increase, suggesting improved heterojunction and/or worsen CdS qualities. Based on our experiment results, MA5 has a smaller E_g than MA0, implying a shallower absorption depth in the CZTS layer. Although we cannot exclude the effect of heterojunction modification, a deteriorated CdS layer (stronger SRH recombination or a lower doping level) would also be expected. Due to the fact that CdS fabricated by CBD is very defective^{22,23},

the smaller CPD increase more likely implies the decrease of CdS doping level, instead of stronger recombination). This hypothesis is reasonable because approximately 5 at% Cu has been found within the CdS layer by TEM EDS, as displayed in Chapter 4. According to the numerical simulations and experimental findings, Cu is considered as an acceptor dopant in CdS²⁴⁻²⁸. Furthermore, the considerable drop of CPD in the HJA-treated samples can be seen under high light injection as the heterojunction QFLS dominates the CPD change.

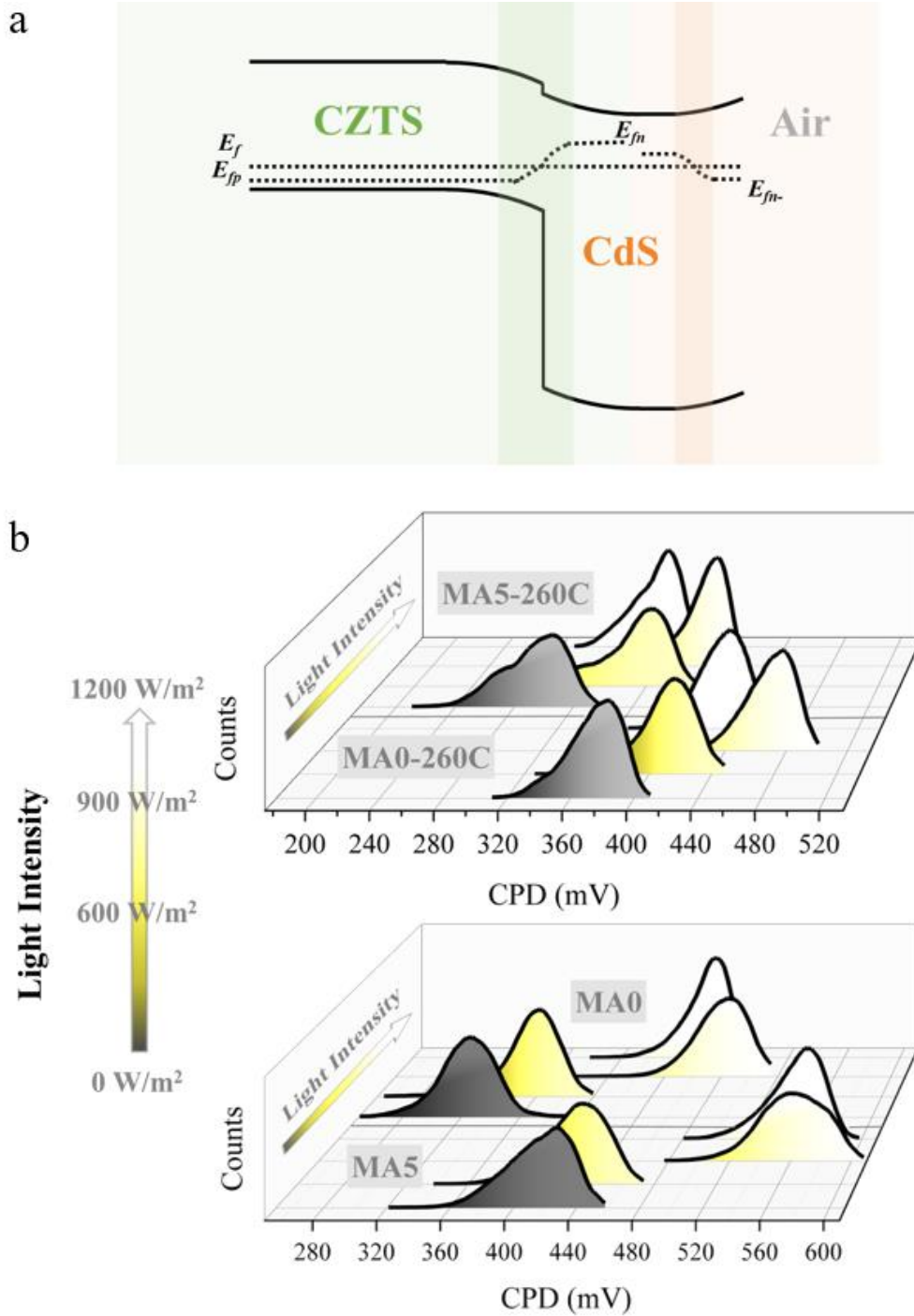


Figure 6.9 a. Schematic band alignment showing two interfaces to be considered: the CZTS/CdS heterointerface and the CdS/air interface. For brevity, these two interfaces are independently shown in this diagram. b. Light intensity-dependent KPFM measurement at 450 nm excitation wavelength. The corresponding light intensity values are displayed in different colours, shown in the scale arrow.

The decrease in the CdS doping level can lead to the shift of the space charge region (SCR) towards the CdS layer (i.e. wider SCR within the CdS layer). This could explain the enhanced blue response. The evidence of the increase in depletion region width can be witnessed from the EQE measurement by comparing the EQE value measured under -1.5 V bias voltage with the zero-bias condition, as shown in Figure 6.10. The depletion region width within n-type semiconductors is expressed as,

$$x_n = \sqrt{\frac{2\epsilon N_a}{q N_d} \frac{1}{N_a + N_d} (V_{bi} - V_a)} \quad (16)$$

where ϵ is the permittivity of this n-type material, and N_a and N_d respectively represent its acceptor and donor defect density, and V_{bi} and V_a indicate the built-in potential and the applied bias potential, respectively. The n-type CdS is known to be highly compensated by comparable densities of shallow donor and deep acceptor levels^{22,23,29}. Thus, the application of negative bias voltage has strong impacts on the value of x_n . Based on the expression, the increase of N_a and the reduction of N_d due to Cu incorporation result in larger depletion region width within the CdS layer. Given larger negative bias voltage, higher weight in $V_{bi} - V_a$ sector results in a noticeable increase in depletion region width. As the curve of EQE at -1.5V/0 V bias ratio ($EQE_{-1.5V}/EQE_{0V}$) displays, MA5 has slightly smaller improvement at the short-wavelength region, indicating a longer depletion region width in the CdS layer.

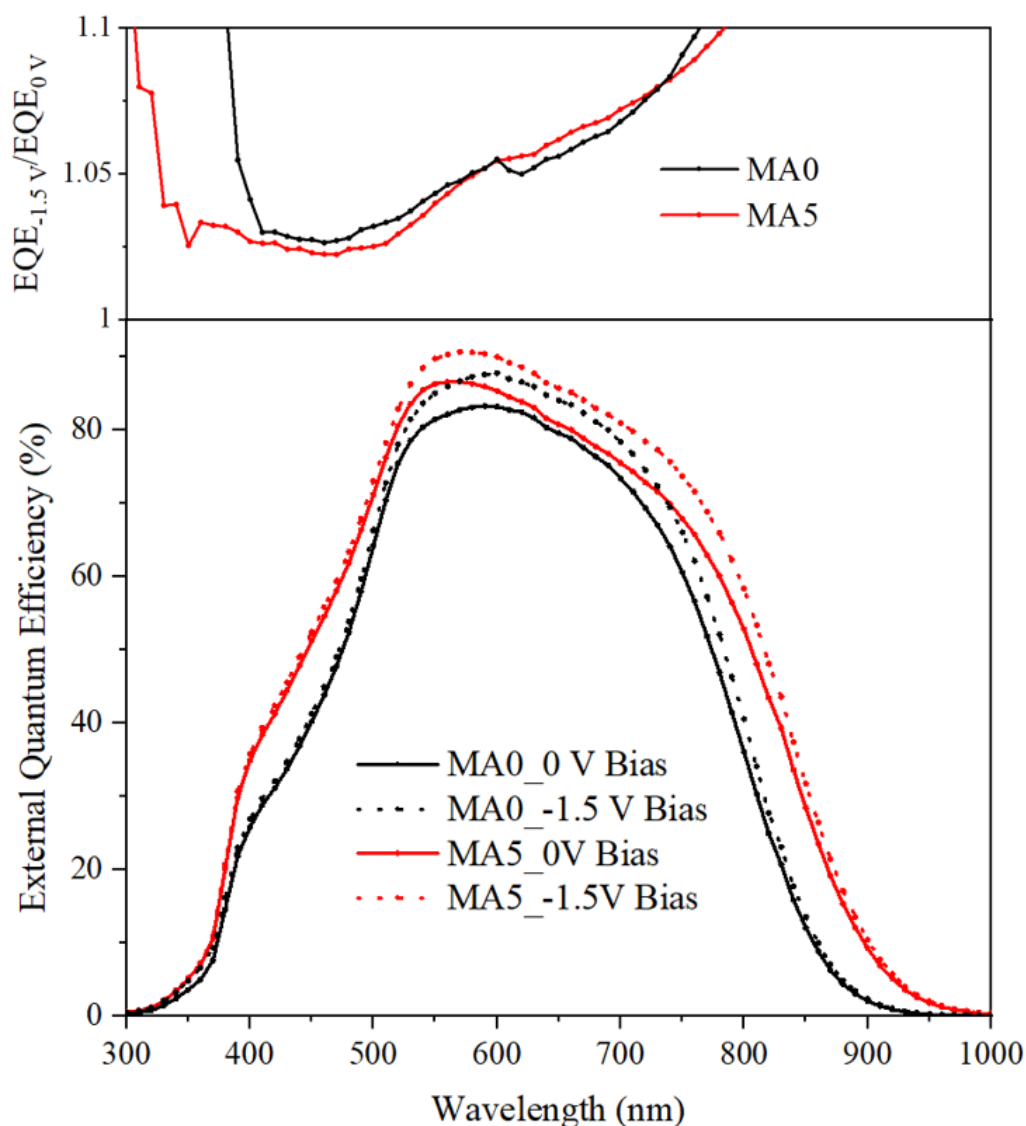


Figure 6.10 External quantum efficiency (EQE) spectra of MA0 and MA5 w/ and w/o -1.5 V bias voltage. The top panel is the ratio of EQE at -1.5 V bias to that without bias.

Although it is difficult to directly measure the doping concentration of the CdS layer grown on the CZTS films using the Mo back contact, based on our characterization results and literature reports about Cu-doped CdS, it is reasonable to deduct that the CdS doping level is reduced due to the elemental interdiffusion in MA5. The decreased CdS n-type doping is detrimental to the QFLS at the p-type CZTS, and therefore, restricting the V_{OC} improvement which was achieved by the MAPDA-induced heterojunction modification at the CZTS side.

The limitation could be addressed by preventing Cd out-diffusion from CdS via an additional Cd-soaking treatment³⁰⁻³² between the MAPDA and the CdS-CBD processes, or by performing a post-treatment after the CdS deposition aiming to improve CdS n-type doping.

6.6 Summary

In this chapter, we utilized nanoscale optoelectronic characterization methods to achieve an in-depth understanding of the MAPDA and HJA treatments. Nanoscale characterizations (KPFM and C-AFM) were firstly employed to prove that excessive Na at the CZTS surface is detrimental, leading to severe shunting paths. The surface photovoltage (SPV) analysis obtained from the KPFM measurement exhibits significant improvement in quasi-Fermi level splitting (QFLS) and grain boundary passivation by the combined MAPDA and HJA treatments. The QFLS driven under low light injection from the light intensity-dependent SPV measurement indicates the remarkable mitigation of SRH recombination. Eventually, we used the light intensity-dependent SPV measurement to unveil the possible mechanisms of the CdS layer change due to the elemental interdiffusion. A deeper understanding of this technique gives advantages to consider some strategies to further upgrade efficiency upon this technology and to apply it to other semiconductors.

6.7 Reference

- 1 Kelvin, L. J. T. L., Edinburgh,, Magazine, D. P. & Science, J. o. V. Contact electricity of metals. **46**, 82-120 (1898).
- 2 Zisman, W. J. R. o. S. I. A new method of measuring contact potential differences in metals. **3**, 367-370 (1932).

- 3 Nonnenmacher, M., o'Boyle, M. & Wickramasinghe, H. K. J. A. p. 1. Kelvin probe force microscopy. **58**, 2921-2923 (1991).
- 4 Kronik, L. *et al.* Band diagram of the polycrystalline CdS/Cu (In, Ga) Se₂ heterojunction. *Applied Physics Letters* **67**, 1405-1407 (1995).
- 5 Sadewasser, S., Glatzel, T., Rusu, M., Jäger-Waldau, A. & Lux-Steiner, M. C. J. A. P. L. High-resolution work function imaging of single grains of semiconductor surfaces. *Applied Physics Letters* **80**, 2979-2981 (2002).
- 6 Jiang, C.-S. *et al.* Direct evidence of a buried homojunction in Cu (In, Ga) Se₂ solar cells. *Applied Physics Letters* **82**, 127-129 (2003).
- 7 Jiang, C.-S. *et al.* Local built-in potential on grain boundary of Cu (In, Ga) Se₂ thin films. *Applied physics letters* **84**, 3477-3479 (2004).
- 8 Jiang, C.-S. *et al.* Does the local built-in potential on grain boundaries of Cu (In, Ga) Se₂ thin films benefit photovoltaic performance of the device? *Applied physics letters* **85**, 2625-2627 (2004).
- 9 Takihara, M., Minemoto, T., Wakisaka, Y. & Takahashi, T. An investigation of band profile around the grain boundary of Cu (InGa) Se₂ solar cell material by scanning probe microscopy. *Progress in Photovoltaics: Research and Applications* **21**, 595-599 (2013).
- 10 Nicoara, N. *et al.* Direct evidence for grain boundary passivation in Cu (In, Ga) Se₂ solar cells through alkali-fluoride post-deposition treatments. *Nature Communications* **10**, 1-8 (2019).
- 11 Li, J. B., Chawla, V. & Clemens, B. M. Investigating the role of grain boundaries in CZTS and CZTSSe thin film solar cells with scanning probe microscopy. *Advanced Materials* **24**, 720-723 (2012).

- 12 Redinger, A. & Unold, T. J. S. r. High surface recombination velocity limits Quasi-Fermi level splitting in kesterite absorbers. *Scientific Reports* **8**, 1874 (2018).
- 13 Tennyson, E. M. *et al.* Nanoimaging of Open-Circuit Voltage in Photovoltaic Devices. *Advanced Energy Materials* **5** (2015).
- 14 Park, J. *et al.* Investigation of low intensity light performances of kesterite CZTSe, CZTSSe, and CZTS thin film solar cells for indoor applications. *Journal of Materials Chemistry A* **8**, 14538-14544 (2020).
- 15 Gloeckler, M., Sites, J. R. & Metzger, W. K. J. J. o. a. p. Grain-boundary recombination in Cu (In, Ga) Se 2 solar cells. *Journal of Applied Physics* **98**, 113704 (2005).
- 16 Metzger, W. & Gloeckler, M. J. J. o. A. P. The impact of charged grain boundaries on thin-film solar cells and characterization. *Journal of Applied Physics* **98**, 063701 (2005).
- 17 Xie, H. *et al.* Impact of Na dynamics at the Cu₂ZnSn (S, Se) ₄/CdS interface during post low temperature treatment of absorbers. *ACS applied materials & interfaces* **8**, 5017-5024 (2016).
- 18 Chen, S., Walsh, A., Gong, X. G. & Wei, S. H. Classification of lattice defects in the kesterite Cu₂ZnSnS₄ and Cu₂ZnSnSe₄ earth-abundant solar cell absorbers. *Advanced Materials* **25**, 1522-1539 (2013).
- 19 Yan, C. *et al.* Cu ₂ ZnSnS ₄ solar cells with over 10% power conversion efficiency enabled by heterojunction heat treatment. *Nature Energy* **3**, 764-772 (2018).
- 20 Nicoara, N. *et al.* Effect of the KF post-deposition treatment on grain boundary properties in Cu (In, Ga) Se 2 thin films. *Scientific reports* **7**, 41361 (2017).
- 21 Atzori, L., Iera, A. & Morabito, G. The internet of things: A survey. *Computer Networks* **54**, 2787-2805 (2010).

- 22 Gloeckler, M. & Sites, J. Apparent quantum efficiency effects in CdTe solar cells. *Journal of Applied Physics* **95**, 4438-4445 (2004).
- 23 Liu, F. *et al.* Light-Bias-Dependent External Quantum Efficiency of Kesterite Cu₂ZnSnS₄ Solar Cells. *ACS Photonics* **4**, 1684-1690 (2017).
- 24 Sullivan, G. A. J. P. R. Diffusion and solubility of Cu in CdS single crystals. *Physical Review* **184**, 796 (1969).
- 25 Varley, J. & Lordi, V. Intermixing at the absorber-buffer layer interface in thin-film solar cells: The electronic effects of point defects in Cu (In, Ga)(Se, S) ₂ and Cu₂ZnSn (Se, S) ₄ devices. *Journal of Applied Physics* **116**, 063505 (2014).
- 26 Nishidate, K. *et al.* Density-functional electronic structure calculations for native defects and Cu impurities in CdS. *Physical Review B* **74**, 035210 (2006).
- 27 Varley, J. & Lordi, V. Electrical properties of point defects in CdS and ZnS. *Applied Physics Letters* **103**, 102103 (2013).
- 28 Kashiwaba, Y., Kanno, I. & Ikeda, T. p-Type characteristics of Cu-doped CdS thin films. *Japanese journal of applied physics* **31**, 1170 (1992).
- 29 Cowache, P. & Vedel, J. CdS solar cells with electrochemically formed Cu₂S: Improvement of the current collect. *Solar Cells* **15**, 359-364 (1985).
- 30 Lei, B. *et al.* Cadmium ion soaking treatment for solution processed CuInS_xSe_{2-x} solar cells and its effect on defect properties. *Solar Energy Materials and Solar Cells* **95**, 2384-2389 (2011).
- 31 Ben Messaoud, K. *et al.* Impact of the Cd²⁺ treatment on the electrical properties of Cu₂ZnSnSe₄ and Cu (In, Ga) Se₂ solar cells. *Progress in Photovoltaics: Research and Applications* **23**, 1608-1620 (2015).

- 32 Sun, K. *et al.* Minority lifetime and efficiency improvement for CZTS solar cells via Cd ion soaking and post treatment. *Journal of Alloys and Compounds* **750**, 328-332 (2018).

Chapter 7

Summary and Future Work

7.1 Overall Conclusions

This thesis aims to fabricate efficient high- E_g pure sulfide kesterite CZTS solar cells by developing novel technologies to modify the quality of heterojunction. Previous studies related to the optoelectrical properties of CZTS, the loss mechanisms and the relevant approaches have been reviewed. Severe trap-assisted recombination, especially at the heterojunction region, is recognized as one of the major limiting factors of efficiency development. Post treatments have advantages to engineering the defects targetedly at the as-formed absorber layers. Herein, for the first time, we invented two core post-treatment technologies – heterointerface passivation via a dielectric ultrathin SnO_2 layer and manipulation of trace elemental distributions through in-house developed moisture-assisted post-deposition annealing (MAPDA). The latter was upgraded to yield the best efficiency using a follow-up heterojunction air annealing (HJA) at a relatively low temperature. The in-depth mechanisms of MAPDA and the follow-up HJA treatments were investigated for providing a better understanding of this novel technology and ease of the applications to other materials. These post-treatment technologies can be applied to diverse semiconductors in general, with broad interests in surface passivation, modification of elemental distributions, defect engineering, etc.

The author's novel contributions in each chapter are discussed below:

In Chapter 3, an ultrathin SnO_2 layer using a solution method was introduced between the CdS buffer and the CZTS absorber for the heterointerface passivation. This ultrathin SnO_2

layer not only provides a chemical passivation route, but it also modifies the band alignment at the heterojunction. The passivation effect is reflected in the improved minority carrier lifetime. The function of shunt blocking via this layer allows the use of a thinner CdS layer to alleviate the parasitic absorption by the CdS layer.

In Chapter 4, another strategy – manipulation of trace elements by a novel MAPDA technology was developed. This promising technology enables the removal of excessive alkali metal elements from the absorber layer, which, in turn, enhanced the spontaneous diffusion of Cd into the absorber layer during the follow-up CBD process for the CdS deposition. Defect engineering was also achieved by such elemental redistribution, leading to the formation of favorable V_{Cu} shallow acceptors and the transition of the doping source from deep acceptors Zn_{Sn} to shallower acceptors Cu_{Zn} . The redistribution of critical trace elements also contributes to the significant decrease of deep acceptor states at both the CZTS bulk and particularly the CdS/CZTS heterointerface. This elemental redistribution induced defect engineering contributes to escalating device performance.

In Chapter 5, we combined the above MAPDA treatment with another promising HJA treatment to achieve a further leap of conversion efficiency at 9.40 %. SRH recombination at the heterojunction was significantly alleviated by a further modification of elemental distributions. The combined treatments yield a PCE much higher than that of samples only treated with HJA. Additionally, we unveiled the CdS variations likely due to the result of elemental redistributions.

Chapter 6 presented an in-depth investigation of MAPDA and HJA treatments related to the optoelectronic properties of CZTS, CdS and the heterojunction using Kelvin probe force microscopy (KPFM) and conductive-atomic force microscopy (C-AFM). We initially unveiled the detrimental effects of excessive Na and K phases at CZTS surface. Then we demonstrated the dramatic increase of nanoscale V_{OC} of the CdS/CZTS samples with the combined MAPDA and HJA treatments by KPFM-based surface photovoltage (SPV) measurement. SPV measurement under low photon injection revealed remarkable inhibition of SRH recombination for the samples with the combined treatments, which also indicates a potential for indoor applications. Finally, we applied SPV measurement under the support of EQE measurement under biased voltage to reveal the changes of the CdS electrical properties.

Overall, these novel technologies developed in this thesis are promising in various applications. Although the absolute improvement of device performance did not break the efficiency bottleneck, the potential of these technologies may have a far-reaching influence in many fields.

7.2 Future Work

The promising MAPDA technology shows wide potential applications in aspects of extrinsic elemental diffusion, heterojunction and bulk modifications, indoor applications, etc. We will expand the research in the MAPDA treatment for these applications and utilize the implications to develop more novel approaches, finding out the next key technologies to boost the efficiency of kesterite solar cells and paving the pathway of the green and constituent-abundant kesterite semiconductors into commercialization.

7.2.1 Investigation of the Correlation among CdS Compositional, Structural and Optoelectrical Properties due to MAPDA and HJA

In Chapter 4, a noticeable concentration of Cu diffusion into the CdS layer was observed in the MAPDA-devices, which was regarded as a result of elemental interdiffusion within CdS. In Chapters 5 and 6, we observed some variations of the CdS layer in phase, crystallinity, interplanar distance as well as its doping level. We speculate that post-annealing induced changes in structural and optoelectrical properties of CdS might be interrelated. Understanding their correlations is of importance to promote the device performance of all solar cells using CdS as a buffer layer.

7.2.2 Upgrading of the MAPDA Technology by Adding a Cd Ion Soaking Process Before the CdS Deposition

At the end of Chapter 6, a reduced CdS doping level was found in the MAPDA-devices. As discussed, lower n-type doping is detrimental to the V_{oc} improvement. To maximize the device performance due to the elemental redistributions in the CZTS layer, preventing Cu diffusion into CdS may be important to avoid the CdS doping level decrease. This can be at least partially achieved by limiting Cd out-diffusion from the CdS layer. Cd ion soaking¹ could be an effective way to occupy Cu vacancies remained at the CZTS layer after MAPDA and thus restricting the Cd loss from the CdS layer, which is possibly a promising method for further improving the device performance under the MAPDA treatment.

7.2.3 An Efficient Li Doping Strategy by MAPDA and LiCl Post-deposition Treatment

Due to the close ionic radius of Li (0.73 Å) and Cu (0.74 Å), a high possibility of Li incorporation would be predicted. However, only traces of Li (Li/Cu molar ratio in the order of 10^{-4}) were observed in the CZTSSe films². Furthermore, based on our recent report³,

shallow Li_{Zn} acceptor states (shallower than the common shallow dopants Cu_{Zn}) can be created using the LiCl treatment after the CZTS growth. However, the concentration of Li diffusion is very limited (0.0062 at %) as well. The barrier of Li incorporation is believed to be the presence of massive Na⁴, which can be removed by our MAPDA treatment. Therefore, much higher concentrations of preferable Li_{Zn} and Li_{Cu} antisites can be expected.

7.2.4 Promoting V_{OC} by Passivating Acceptor-like Interface Defects via MAPDA plus ZnCl_2 or $\text{Zn}(\text{CH}_3\text{COO})_2$ Post-treatment

Recently, we determined that the V_{OC} of CZTS is severely limited by the high density of acceptor-like interface defects, supported by experiments and numerical simulations⁵. Therefore, a method of acceptor-like defect passivation at the CZTS surface is essential for promoting the V_{OC} of CZTS solar cells. The point defect – Zn_{Cu} , as a shallow donor state, is benign in CZTS^{6,7} which could be a cure for passivating these V_{OC} -limiting defects. Acceptor-like defects with relatively low formation energies (V_{Cu} , Cu_{Zn} and Zn_{Sn}) are prone to form benign neutral clusters ($[\text{Zn}_{\text{Cu}} + V_{\text{Cu}}]$, $[\text{Zn}_{\text{Cu}} + \text{Cu}_{\text{Zn}}]$ and $[2\text{Zn}_{\text{Cu}} + \text{Zn}_{\text{Sn}}]$) with Zn_{Cu} donors in lower formation energies⁷. To achieve this goal, researchers would normally consider two routes: either increasing the Zn concentration or alloying Zn through a post-treatment. However, increasing Zn ratio in the CZTS metal/compound precursors would also result in the compensation of p-type doping of the entire CZTS layer. Therefore, this route is not adoptable. Post-treatment could be an effective way to form Zn-rich compositions at the CZTS surface and thus compensating those acceptor-like defects. The creation of Cu vacancies due to Na loss by MAPDA could make the formation of Zn_{Cu} donors easier, pushing the junction deeper into the CZTS region.

7.3 Reference

- 1 Sun, K. *et al.* Minority lifetime and efficiency improvement for CZTS solar cells via Cd ion soaking and post treatment. *Journal of Alloys and Compounds* **750**, 328-332 (2018).
- 2 Yang, Y., Huang, L. & Pan, D. New insight of Li-doped Cu₂ZnSn (S, Se) 4 thin films: Li-induced Na diffusion from soda lime glass by a cation-exchange reaction. *ACS Applied Materials & Interfaces* **9**, 23878-23883 (2017).
- 3 He, M. *et al.* High Efficiency Cu₂ZnSn (S, Se) 4 Solar Cells with Shallow LiZn Acceptor Defects Enabled by Solution-Based Li Post-Deposition Treatment. *Advanced Energy Materials* **11**, 2003783 (2021).
- 4 Romanyuk, Y. E. *et al.* Doping and alloying of kesterites. *Journal of Physics: Energy* **1**, 044004 (2019).
- 5 Li, J. *et al.* Interface recombination of Cu₂ZnSnS₄ solar cells leveraged by high carrier density and interface defects. *Solar RRL* (2021).
- 6 Chen, S., Yang, J.-H., Gong, X.-G., Walsh, A. & Wei, S.-H. Intrinsic point defects and complexes in the quaternary kesterite semiconductor Cu₂ZnSnS₄. *Physical Review B* **81**, 245204 (2010).
- 7 Chen, S., Walsh, A., Gong, X. G. & Wei, S. H. Classification of lattice defects in the kesterite Cu₂ZnSnS₄ and Cu₂ZnSnSe₄ earth-abundant solar cell absorbers. *Advanced Materials* **25**, 1522-1539 (2013).

Appendix A – List of Publications

Journal Publications

1. **H. Sun**, K. Sun, J. Huang, C. Yan, F. Liu, J. Park, A. Pu, J. A. Stride, M. A. Green, and X. Hao, *Efficiency enhancement of kesterite $\text{Cu}_2\text{ZnSnS}_4$ solar cells via solution-processed ultrathin tin oxide intermediate layer at absorber/buffer interface*, ACS Applied Energy Materials, 2017, 1, 154-160.
2. **H. Sun**, J. Huang, C. Yan, K. Sun, J. S. Yun, J. Li, T. L. Young, A. F. O'Neill, M. P. Nielsen, X. Cui, A. Wang, J. Seidel, J. A. Stride, M. A. Green, and X. Hao, *Manipulating the distributions of Na and Cd by moisture-assisted post-deposition annealing for efficient kesterite $\text{Cu}_2\text{ZnSnS}_4$ solar cells*. Ready for submission.
3. **H. Sun**, J. Huang, T. L. Young, J. Cong, J. Li, K. Sun, C. Yan, J. S. Yun, X. Cui, M. P. Nielsen, J. A. Stride, M. A. Green, and X. Hao, *Defect engineering for efficient $\text{Cu}_2\text{ZnSnS}_4$ solar cells via moisture-assisted post-deposition annealing*, Ready for submission.
4. J. Park, Z. Ouyang, C. Yan, K. Sun, **H. Sun**, F. Liu, M. Green, and X. Hao, *Hybrid Ag nanowire-ITO as transparent conductive electrode for pure sulphide kesterite $\text{Cu}_2\text{ZnSnS}_4$ solar cells*, 2017, 121, 20597-20604.
5. J. Huang, C. Yan, K. Sun, F. Liu, **H. Sun**, A. Pu, X. Liu, M. Green, and X. Hao, *Boosting the kesterite $\text{Cu}_2\text{ZnSnS}_4$ solar cells performance by diode laser annealing*, Solar Energy Materials and Solar Cells, 2017, 175, 71-76.
6. J. Park, J. Huang, K. Sun, Z. Ouyang, F. Liu, C. Yan, **H. Sun**, A. Pu, M. Green, and X. Hao, *The effect of thermal evaporated MoO_3 intermediate layer as primary back contact for kesterite $\text{Cu}_2\text{ZnSnS}_4$ solar cells*, Thin Solid Films, 2018, 648, 39-45.

7. K. Sun, C. Yan, J. Huang, K. Sun, **H. Sun**, L. Jiang, X. Deng, J. Stride, X. Hao, and F. Liu, *Minority lifetime and efficiency improvement for CZTS solar cells via Cd ion soaking and post treatment*, Journal of Alloys and Compounds, 2018, 750, 328-332.
8. K. Sun, J. Huang, C. Yan, A. Pu, F. Liu, **H. Sun**, X. Liu, Z. Fang, J. A. Stride, M. Green, and X. Hao, *Self-assembled nanometer-scale ZnS structure at the CZTS/ZnCdS heterointerface for high-efficiency wide band gap $\text{Cu}_2\text{ZnSnS}_4$ solar cells*, Chemistry of Materials, 2018, 30, 4008-4016.
9. J. Park, J. Huang, J. Yun, F. Liu, Z. Ouyang, **H. Sun**, C. Yan, K. Sun, K. Kim, J. Seidel, S. Chen, M. A. Green, and X. Hao, *The role of hydrogen from ALD- Al_2O_3 in kesterite $\text{Cu}_2\text{ZnSnS}_4$ solar cells: grain surface passivation*, Advanced Energy Materials, 2018, 8, 1701940.
10. K. Sun, F. Liu, J. Huang, C. Yan, N. Song, **H. Sun**, C. Xue, Y. Zhang, A. Pu, Y. Shen, J. A. Stride, M. Green, and X. Hao, *Flexible kesterite $\text{Cu}_2\text{ZnSnS}_4$ solar cells with sodium-doped molybdenum back contacts on stainless steel substrates*, Solar Energy Materials and Solar Cells, 2018, 182, 14-20.
11. C. Yan, J. Huang, K. Sun, S. Johnston, Y. Zhang, **H. Sun**, A. Pu, M. He, F. Liu, K. Eder, L. Yang, J. M. Cairney, N. J. Ekins-Daukes, Z. Hameiri, J. A. Stride, S. Chen, M. A. Green, and X. Hao, *$\text{Cu}_2\text{ZnSnS}_4$ solar cells with over 10% power conversion efficiency enabled by heterojunction heat treatment*, Nature Energy, 2018, 3, 764-772.
12. X. Cui, K. Sun, J. Huang, C. Lee, C. Yan, **H. Sun**, Y. Zhang, F. Liu, M. A. Hossain, Y. Zakaria, L. H. Wong, M. Green, B. Hoex, and X. Hao, *Enhanced heterojunction interface quality to achieve 9.3% efficient Cd-free $\text{Cu}_2\text{ZnSnS}_4$ solar cells using ALD ZnSnO buffer layer*, Chemistry of Materials, 2018, 30, 7860-7871.
13. X. Cui, K. Sun, J. Huang, J. S. Yun, C. Lee, C. Yan, **H. Sun**, Y. Zhang, C. Xue, K. Eder, L. Yang, J. M. Cairney, J. Seidel, N. J. Ekins-Daukes, M. Green, B. Hoex, and X. Hao,

Cd-Free Cu₂ZnSnS₄ solar cell with an efficiency greater than 10% enabled by Al₂O₃ passivation layers, Energy & Environmental Science, 2019, 12, 2751-2764.

14. K. Sun, C. Yan, J. Huang, F. Liu, J. Li, **H. Sun**, Y. Zhang, X. Cui, A. Wang, Z. Fang, J. Cong, Y. Lai, M. A. Green, and X. Hao, *Beyond 10% efficiency Cu₂ZnSnS₄ solar cells enabled by modifying the heterojunction interface chemistry*, Journal of Materials Chemistry A, 2019, 7, 27289-27296.
15. G. He, C. Yan, J. Li, X. Yuan, K. Sun, J. Huang, **H. Sun**, M. He, Y. Zhang, J. A. Stride, M. A. Green, and X. Hao, *11.6% Efficient pure sulfide Cu(In,Ga)S₂ solar cell through a Cu-deficient and KCN-free process*, ACS Applied Energy Materials, 2020, 3, 11974-11980.

Conference Publications

1. **H. Sun**, J. Huang, J. S. Yun, K. Sun, C. Yan, F. Liu, J. Park, A. Pu, J. Seidel, J. A. Stride, M. Green and X. Hao, *Solution-processed ultrathin SnO₂ passivation of absorber/buffer heterointerface and grain boundaries for high efficiency kesterite Cu₂ZnSnS₄ solar cells*, 2019 IEEE 46th Photovoltaic Specialists Conference (PVSC). IEEE, 2019, 2503-2506.
2. K. Sun, C. Yan, J. Huang, F. Liu, **H. Sun**, A. Pu, M. Green, and X. Hao, *Boosting the efficiency of kesterite Cu₂ZnSnS₄ solar cells by optimizing the heterojunction interface quality*, 2018 IEEE 7th World Conference on Photovoltaic Energy Conversion (WCPEC) (A Joint Conference of 45th IEEE PVSC, 28th PVSEC & 34th EU PVSEC). IEEE, 2018, 3048-3050.
3. X. Cui, K. Sun, C. Lee, C. Yan, **H. Sun**, Y. Zhang, F. Liu, M. Green, B. Hoex, and X. Hao, *ALD ZnSnO buffer layer for enhancing heterojunction interface quality of CZTS solar cells*, 2018 IEEE 7th World Conference on Photovoltaic Energy Conversion

(WCPEC) (A Joint Conference of 45th IEEE PVSC, 28th PVSEC & 34th EU PVSEC).
IEEE, 2018, 1166-1171.

4. X. Cui, K. Sun, J. Huang, C. Lee, C. Yan, **H. Sun**, Y. Zhang, M. Green, B. Hoex, and X. Hao, *High-efficient Cd-free CZTS solar cells achieved by nanoscale atomic layer deposited aluminium oxide*, 2019 IEEE 46th Photovoltaic Specialists Conference (PVSC).
IEEE, 2019, 2482-2484.